LOW ADHESION DETECTION AND IDENTIFICATION IN A RAILWAY VEHICLE SYSTEM USING TRACTION MOTOR BEHAVIOUR

Yunshi Zhao

October 2013

A thesis submitted to the University of Huddersfield in partial fulfilment of the requirements for the degree of Doctor of Philosophy

The University of Huddersfield

Acknowledgements

I am very grateful to Prof. Simon Iwnicki and Dr. Bo Liang for their support and guidance throughout my PhD research.

I would like to thank everyone else of the Institute of Railway Research for their help.

I would also like to thank Denis Town, Philip Holdsworth, Steve Goldstein, Richard Midlam and all the other technicians from the university of Huddersfield and Manchester Metropolitan University for their excellent work on manufacturing the test rig for this project.

I would also thank Cencen Gong for being the best colleague, friend and flatmate. Her support in both my work and life is very important to me.

Finally I would like to express my deepest gratitude to my parents and grandparents, who have always been supporting and encouraging me.

Abstract

It is important to monitor the wheel-rail friction coefficient in railway vehicles to improve their traction and braking performance as well as to reduce the number of incidents caused by low friction. Model based fault detection and identification (FDI) methods, especially state observers have been commonly used in previous research to monitor the wheel-rail friction. However, the previous methods cannot provide an accurate value of the friction coefficient and few of them have been validated using experiments.

A Kalman filter based estimator is proposed in this research project. The developed estimator uses signals from the traction motor and provides a new and more efficient approach to monitoring the condition of the wheel-rail contact condition.

A 1/5 scaled test rig has been built to evaluate the developed method. This rig comprises 2 axle-hung induction motors driving both the wheelsets of the bogie through 2 pairs of spur gears. 2 DC generators are used to provide traction load to the rollers through timing pulleys. The motors are independently controlled by 2 inverters. Motor parameters such as voltage, current and speed are measured by the inverters. The speed of the wheel and roller and the output of the DC generator are measured by incremental encoders and Hall-effect current clamps. A LabVIEW code has been designed to process all the collected data and send control commands to the inverters. The communication between the PC and the inverters are realized using the Profibus (Process Field Bus) and the OPC (Object Linking and Embedding (OLE) for Process Control) protocol.

3 different estimators were first developed using computer simulations. Kalman filter and its two nonlinear developments: extended Kalman filter (EKF) and unscented Kalman filter (UKF) have been used in these 3 methods. The results show that the UKF based estimator can provide the best performance in this case. The requirement for measuring the roller speed and the traction load are also studied using the UKF. The results show that it is essential to measure the roller speed but the absence of the traction load measurement does not have significant impact on the estimation accuracy.

A re-adhesion control algorithm, which reduces excessive creepage between the wheel and rail, is developed based on the UKF estimator. Accurate monitoring of the friction coefficient helps the traction motor work at its optimum point. As the largest creep force is generated, the braking and accelerating time and distance can be reduced to their minimum values. This controller can also avoid excessive creepage and hence potentially reduce the wear of the wheel and rail.

The UKF based estimator development has been evaluated by experiments conducted on the roller rig. Three different friction conditions were tested: base condition without contamination, water contamination and oil contamination. The traction load was varied to cover a large range of creepage. The importance of measuring the roller speed and the traction load was also studied. The UKF based estimator was shown to provide reliable

estimation in most of the tested conditions. The experiments also confirm that it is not necessary to measure the traction load and give good agreement with the simulation results.

With both the simulation and experiment work, the UKF based estimator has shown its capability of monitoring the wheel-rail friction coefficient.

Table of Contents

List of Figures

List of Tables

List of Symbols

A	System matrices for the induction motor
a, b	The contact ellipse semi-axes
α, β	Scaling parameter for unscented Kalman filter
B, D	Reduction factors for the friction coefficient
C_{11}, C_{22}, C_{23}, C_{33}	Kalker confidents
E	Young's modulus
F_N	Normal force at the wheel-rail (roller) surface
F_γ	Longitudinal creep force at the wheel- rail (roller) surface
H	Measurement matrix for the induction motor at the motor
$I_{\alpha s}$, $I_{\beta s}$, $I_{\alpha r}$, $I_{\beta r}$	Stator and rotor current at α and β phase at the motor
i	Transmission ratio of the gearset
J_{motor}, J_{wheel}, J_{roller},	Inertia of the motor, wheel and roller
K	Kalman filter gain matrix
k_A, k_S	Reduction factors of creep force
κ	Scaling parameter for unscented Kalman filter
L	dimension of a random variable
Ls, Lr, Lm	Stator, rotor and mutual inductance
Xs, Xr, Xm	Stator, rotor and mutual reactance
m, n	Hertz contact parameter
n_p	Number of poles of the motor
P_{max}	maximum contact pressure between the wheel and rail
$\mathbf{P^-}$, **P**	Predicted and corrected error covariance matrix
Q, R	Covariance matrix of system noise and measurement noise
R_s, R_r	Stator and rotor resistances
R_{w1}, R_{w2}, R_{r1}, R_{r2}	Contact radius at the wheel-rail interface, w for wheel, r for rail
R_{wheel}, R_{roller}	Radius of the wheel and roller
S	Sigma points set
T_e	Electric torque of the motor
T_{Load}	Traction load of the motor
$U_{\alpha s}$, $U_{\alpha s}$, $U_{\alpha s}$, $U_{\alpha s}$	Stator and rotor voltage at α and β phase at the motor
V	Equivalent forward speed of the wheel
v	Measurement noise
ν	Poisson's ratio
W	Sigma point weights
w	System noise

ω_e	Electric speed of the motor
ω_{motor}, ω_{wheel}, ω_{roller}	Rotating speed of the motor, wheel and roller
$\boldsymbol{x}$	State variables
$\boldsymbol{z}$	Measurements
$\hat{\boldsymbol{x}}$, $\hat{\boldsymbol{x}}^{-}$	Predicted and corrected state variables
γ	Creepage
μ, μ_0	Traction and friction coefficients
$\psi_{\alpha s}$, $\psi_{\beta s}$, $\psi_{\alpha r}$, $\psi_{\beta r}$	Stator and rotor flux at α and β phase at the motor

1. Introduction

The friction condition at the wheel-rail interface is a crucial factor in the performance of a railway vehicle, as it determines the available force for accelerating and braking. Incidents can be caused by low friction, which occur most frequently during autumn (due to the presence of leaves on the rails) and affect railway networks throughout the world. Incidents caused by low friction conditions include SPADs (signals passed at danger), station overruns and failures to operate track circuits, usually caused by the presence of contamination on the rail head which prevents the wheels from obtaining adequate adhesion during braking[1]

A summary of the low adhesion incidents that happened in autumn 2000-2005 in the UK [1] is plotted in Figure 1-1.

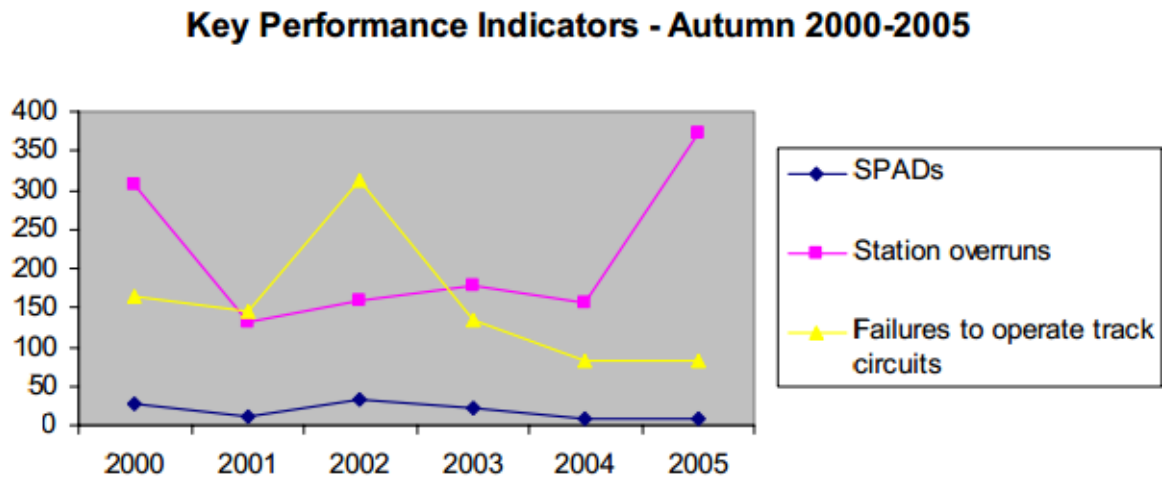

Figure 1-1 Summary of the Low friction incidents

Actions can be taken to avoid these incidents if the friction condition is monitored in real time. With the monitoring of the friction coefficient, intelligent control algorithms can also be developed to achieve a better utilization of the available adhesion at the wheel-rail interface, which can lead to a shorter braking and accelerating time and distance.

Due to the difficulty in measuring the friction coefficient directly, most of the efforts have been made using indirect methods to identify the friction condition based on various measurements. A novel method is proposed in this research to estimate the friction coefficient between the wheel and rail surfaces using the traction motor signals. This method uses fault detection and identification (FDI) technology which monitors the system, detects the fault when it occurs and addresses the type and location of the fault. An analytical redundancy provided by the dynamic relationship between the traction motor and the vehicle-rail system is used in this FDI method, which has rarely been studied in previous research. By using the traction motor behaviour, the developed method can provide a new and more efficient approach to monitoring the condition of the wheel-rail contact condition. Three estimators using Kalman filters and two types of

its nonlinear versions, extended Kalman filter (EKF) and unscented Kalman filter (UKF), have been developed and evaluated using a single wheelset-roller dynamic model. A re-adhesion control algorithm has also been developed to increase the utilization rate of the available adhesion and reduce the acceleration and braking time of the vehicles.

To validate the developed estimators, a 1/5 scaled roller rig has been designed and built. Three different contact conditions (dry, water and oil lubrication) have been tested with varying traction load.

In both the simulation and experiment work, impacts of different combinations of measurements of the estimated system are also discussed to establish the minimum measurements required.

The aims and objectives of this research are listed below:

1.1. Academic Aim

To establish possible novel methods to detect and identify the adhesion status in the railway system using the traction motor as a sensor system.

1.2. Objectives

- To review the existing techniques for vehicle-track system fault detection and identification.
- To study and compare technologies used in vehicle rail system fault detection and identification
- To build a vehicle rail system dynamic model which is suitable for traction motor behaviour based FDI.
- To develop an FDI method to monitor the railway vehicle system using traction motor behaviour.
- To build an roller rig in order to carry out experiments to validate and calibrate the developed FDI method.

2. Literature review

Fault detection and identification technologies are widely used in industry, playing an important role in the fields of condition-based maintenance, predictive maintenance [2], active control and system condition monitoring [3]. Many different methods have been developed and can be classified into three groups: model based, quality based and process history based methods [4-6]. Among these, the model based methods have some desirable characteristics such as good robustness and adaptability as well as the capability of identifying multiple faults [7]. For these reasons the model-based method is widely used in fault detection of many different fields, including in railway engineering.

A two-step algorithm is always used in model based FDI methods, which includes the generation of inconsistencies between the actual and expected behaviour of the monitored system and the selection of a diagnosis decision according to the inconsistencies. Hardware redundancy or analytical redundancy is required in the inconsistency generation. Hardware redundancy requires extra sensors and space which restricts the applications, while analytical redundancy relies on the functional relationship between the inputs and outputs of the monitored system.

To develop an FDI method using the analytical redundancy of the relationship between the traction motor and the vehicle, an accurate dynamic model of the whole system should be built first. Then techniques are used in modelling the vehicle as well as the traction motor and its control method are reviewed below.

Roller-rigs are often used to validate simulation results so existing roller rigs around the world have also been studied.

2.1. State observers

As this research project focuses on developing a model based FDI system, analytical redundancies and residuals are required. For railway vehicles, the dynamic model is also used to provide the analytical redundancy and the residuals can be found in the inconsistencies between the expected and measured parameters.

To generate the residual, three different methods can be used, which are parameter estimation methods, parity equation methods and observer based methods. Observer based methods are commonly adopted in railway system FDI, as faults of railway vehicles are always connected with unmeasured state variables. There are many different types of observer designed to monitor different types of system. For example the Luenberger observer works for the deterministic cases and the Kalman filter works for the stochastic cases. While these two observers are not applicable to nonlinear systems and most dynamic systems in nature are non-linear, Kalman filters can be substituted by extended Kalman filter (EKF) or unscented Kalman filter (UKF), which are developed based on Kalman filters and Particle filters (PF).

The Kalman filter was first proposed in [8] and is developed based on the properties of conditional Gaussian random variables. It minimizes the covariance norm of the estimated state variables and forms a recursive algorithm which the new state estimation is calculated from the previous result. A Kalman filter can offer the best linear solution, when the noises of the system and measurements are white, zero-mean and uncorrelated [9].

To solve the problems of nonlinear systems, a Kalman filter can be linearized at the current estimation using a Taylor series expansion, this forms Extended Kalman filter. An Extended Kalman filter is not an optimal estimator in general cases, as it only approximates the optimality of Bayes' rule by linearization [10]. While the EKF adopts a straightforward way to linearize the estimated system, it also introduces more errors when the system is highly nonlinear. To solve this problem, the unscented Kalman filter was developed which linearizes the system with the unscented transform method (UT). UKF can provide a higher order linearization accuracy but remains the same order of magnitude as the EKF in terms of computing time [11].

2.1.1. Kalman filter

The Kalman filter estimates the observed system based on the knowledge of the input signals, measurements and the physical model of the system, as shown in Figure 2-1.

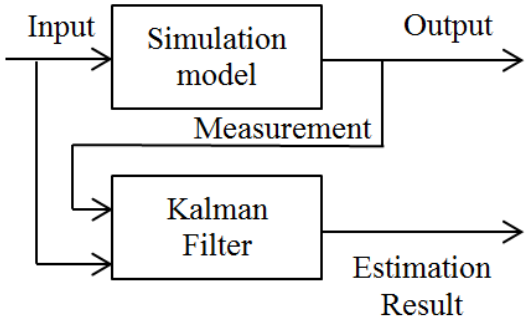

Figure 2-1 Block diagram of Kalman filter

As the measurements are inevitably noisy, it is important to filter the error out. To achieve that, the Kalman filter adopts a "predictor-corrector" algorithm including two sets of equations. Time update equations (predictor), which generate the state variables in the future based on the model of the system and current state variables, as the predictor. The measurement update equations (corrector), which generate the improved estimation result from the difference of the measurements and prediction results the state estimation and the weighting factor called "Kalman gain". The Kalman gain is a factor that minimizes the estimation error covariance.

In the predictor part of this algorithm, where the time is updated, the state of the system and the error covariance matrix are predicted with equation (2-1) and (2-2).

$$\hat{x}_k^- = \mathrm{A}\hat{x}_{k-1} \tag{2-1}$$

$$P_k^- = \mathrm{A}P_{k-1}\mathrm{A}^\mathrm{T} + Q \tag{2-2}$$

Then in the corrector part, where the measurement is updated, the system state estimation is improved with the Kalman filter gain, and the corrected system state and error covariance are used in the prediction of the next time step, as shown in (2-3), (2-4) and (2-5).

$$K_k = P_k^-\mathrm{H}^\mathrm{T}(\mathrm{H}P_k^-\mathrm{H}^\mathrm{T} + R_k)^{-1} \tag{2-3}$$

$$\hat{x}_k = \hat{x}_k^- + K_k(z_k - \mathrm{H}\hat{x}_k^-) \tag{2-4}$$

$$P_k = (I_I - K_k H)P_k^- \tag{2-5}$$

More information about Kalman filter can be found in [8, 12, 13].

2.1.2. Extended Kalman filter

The EKF has the same algorithm as the Kalman filter but linearizes the state and observer matrix at each step of prediction and correction by calculating their Jacobian matrices of partial derivatives so that it can estimate a non-linear system. Hence equations (2-1) to (2-5) are modified as:

$$\hat{x}_k^- = A\hat{x}_{k-1} \tag{2-6}$$

$$P_k = \nabla A P_{k-1} \nabla A^T + Q \tag{2-7}$$

$$K_k = P_k^- \nabla H^T (\nabla H P_k^- \nabla H^T + R_k)^{-1} \tag{2-8}$$

$$\hat{x}_k = \hat{x}_k^- + K_k(z_k - H(\hat{x}_k^-)) \tag{2-9}$$

$$P_k = (I - K_k \nabla H)P_k^- \tag{2-10}$$

where symbol ∇ is the Laplace operator.

2.1.3. Unscented Kalman filter

Although it is straightforward and simple, the EKF has well-known drawbacks. These drawbacks include [14]:

- Instability due to linearization and erroneous parameters
- Costly calculation of Jacobian matrices
- Bias in its estimates,
- Lack of analytical methods for suitable selection of model covariance

The performances of the EKF and UKF to monitor AC motors are compared in [15]. To improve the estimation results, an unscented Kalman filter is then proposed, which

avoids the linearization but utilizes a deterministic sampling approach (the unscented transformation) to calculating the state predictions and covariance. In the unscented transformation (UT), a series of sigma points are chosen based on a square root decomposition of the prior covariance, then these points are propagated through the true nonlinearity of the system, which generates the weighted mean and covariance. The differences between the EKF and UKF are shown in Figure 2-2.

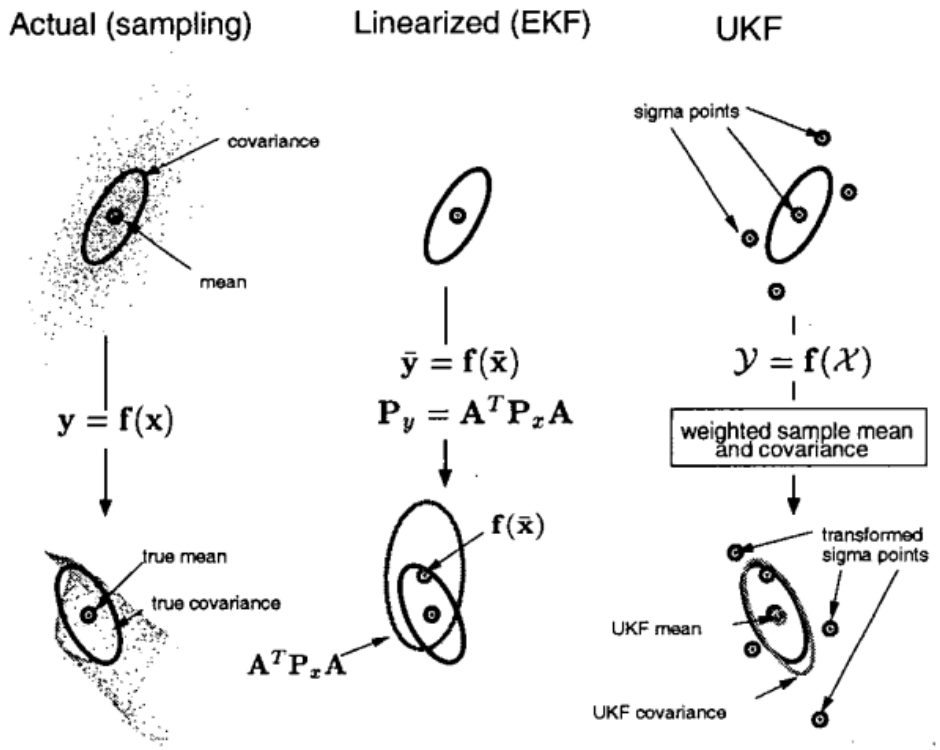

Figure 2-2 Comparison between UKF and EKF [16]

The unscented transformation (UT) is a method for calculating the statistics of a random variable which undergoes a nonlinear transformation. Consider propagating a random variable $\boldsymbol{x}$ (dimension L) through a nonlinear function, $\boldsymbol{y}$ = g($\boldsymbol{x}$). Assume $\boldsymbol{x}$ has mean $\bar{x}$ and covariance P_x and a set of sigma points $\square S$, whose associated weights S =[i=0,1,…, L: $\boldsymbol{x}^{(i)}$, $W^{(i)}$] are taken. The weights $W^{(i)}$ must follow the condition [11]:

$$\sum_{i=0}^{2p} W^{(i)} = 1 \tag{2-11}$$

Given these sigma points, statistics of $\boldsymbol{z}$ can be calculated. First a matrix $\mathcal{X}$ of 2L+1 sigma vectors $\mathcal{X}_i$ is formed according to the following equations [17].

$$\mathrm{X}_0 = \bar{x} \tag{2-12}$$

$$\mathrm{X}_i = \bar{x} + (\sqrt{(L+\lambda)P_x})_i, \; i = 1,....,L \tag{2-13}$$

$$\mathrm{X}_i = \bar{x} - (\sqrt{(L+\lambda)P_x})_i, \; i = L+1,....,2L \tag{2-14}$$

$$\mathrm{W}_0^{(m)} = \lambda / (L+\lambda) \tag{2-15}$$

$$\mathrm{W}_0^{(c)} = \lambda / (L+\lambda) + (1-\alpha^2+\beta) \tag{2-16}$$

$$\mathrm{W}_i^{(m)} = \mathrm{W}_i^{(c)} = 1/[2(L+\lambda)], \; i = 1,...,2L \tag{2-17}$$

where $\lambda=\alpha^2(L+\kappa)-L$ is a scaling parameter. α determines the spread of the sigma points around $\bar{x}$ and is usually set to a small positive value (e.g., 1e-3). κ is a secondary scaling parameter which is usually set to 0, and β is used to incorporate prior knowledge of the distribution of ***x*** (for Gaussian distributions, β=2 is optimal). $(\sqrt{(L+\lambda)P_x})_i$ is the i_{th} row of the matrix square root. These sigma vectors are propagated through the nonlinear function

$$z_i = g(\mathrm{X}_i), \; i = 1,....,2L \tag{2-18}$$

The mean and covariance for ***z*** are approximated using a weighted sample mean and covariance of the posterior sigma points,

$$\bar{z} \approx \sum_{i=0}^{2L} W_i^{(m)} z_i \tag{2-19}$$

$$P_y \approx \sum_{i=0}^{2L} W_i^{(c)} \{z_i - \bar{z}\}\{z_i - \bar{z}\}^T \tag{2-20}$$

Besides the Kalman filter and its other developments, the particle filter (PF) can also offer estimations of non-linear non-Gaussian systems without local linearization or crude approximation and is therefore often used in severely nonlinear systems for which the EKF and UKF cannot offer reliable estimation. Algorithms used in the PF can all be interpreted as the sequential Monte Carlo method which allows the PF to achieve the Bayesian optimal estimation with sufficient knowledge of the studied system [18]. To maintain the estimation accuracy, large sample sizes are required which increases the computational cost of the PF. Due to this disadvantage; the PF has not been implemented before the 1980s despite the fact that it was first proposed in the 1940s.

2.2. Railway vehicle dynamics

In this section, modelling techniques are reviewed to prepare background knowledge in building the dynamic model of the railway vehicle traction model.

For the railway vehicle dynamics, all the forces that guide and support a railway vehicle are generated at the wheel-rail interface. The position of the contact point is critical in calculating the contact force; therefore it is important to study the contact geometry and the way the contact force is generated.

Models used to solve the contact geometry problems can be divided into two groups: rigid body contact models which assume that the wheel and rail are rigid bodies; while the elastic models consider the elastic deformation of the wheel and rail. The rigid body method assumes that the wheel and rail contact at one (or two) isolated point. This method can save up 95% CPU-time compared with a pure elastic model [19] but is less accurate. Traditionally, constraint equations were used to solve the contact problem [20-22] and Newton-Raphson methods were always employed to solve the constraint equations. Another method using a polynomial 2D-tensorproduct splines based approximation was discussed in [19]. The contact problems were further extended into 3D cases and were discussed in [23]. More computer efficient methods were discussed in [24, 25]. Vehicle-rail dynamic coupling models were also developed [26], which consider the interaction of the force and deformation between the vehicle and the rail. Elastic models which consider the influence of the deformation of the wheel and rail were also developed and shown in [27, 28].

The contact force between the wheel and rail surfaces can be split into normal and tangential components. Different models describing the wheel-rail force are reviewed as follows.

2.2.1. Normal force model

The normal force between the wheel and rail surfaces is most commonly calculated using the classical Hertzian model. The Hertzian model assumes that the contact patch size is small comparing to the curvature of the wheel and rail and the curvatures are constant at the contact patch. The wheel and rail are also assumed to deform elastically and can be represented in the semi-infinite spaces. As the result of the Hertzian model, the contact patch is elliptical and the contact pressure is distributed semi-ellipsoidal.

In the Hertzian model, the longitudinal and transversal semi-axis lengths (a and b) of the contact ellipse are calculated as[29]:

$$a = m[\frac{3F_N(1-\upsilon^2)}{(\frac{1}{R_{w1}}+\frac{1}{R_{w2}}+\frac{1}{R_{r1}}+\frac{1}{R_{r2}})E}]^{1/3} \quad (2\text{-}21)$$

$$b = n[\frac{3F_N(1-\upsilon^2)}{(\frac{1}{R_{w1}}+\frac{1}{R_{w2}}+\frac{1}{R_{r1}}+\frac{1}{R_{r2}})E}]^{1/3} \quad (2\text{-}22)$$

R_{w1} is the rolling radius of the wheel, R_{w2} is the radius of the wheel profile at the contact point, R_{r1} is the rolling radius of the rail (infinite in most cases) and R_{r2} is the radius of the rail profile at the contact point. m and n are non-dimensional coefficients that can be found in [30]. E is the elastic modulus of the material. υ is the poison's ratio of the material. F_N is the normal force between the wheel and rail.

As the contact pressure is distributed elliptically, the maximum contact pressure $p_{max}=1.5F_N/(\pi ab)$ and the contact pressure within the contact patch can be calculated using equation (2-23).

$$P(x,y) = \frac{2P_{\max}\bullet(1-(\frac{x}{a})^2-(\frac{y}{b})^2)}{\pi ab} \quad (2\text{-}23)$$

where x and y are the position along the longitudinal and transversal axis of the contact patch.

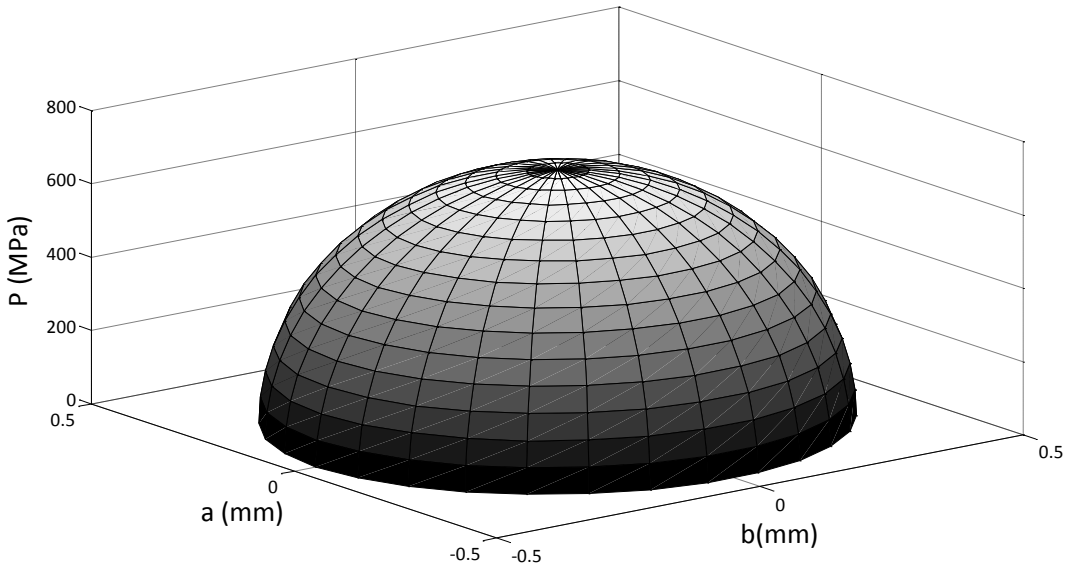

Figure 2-3 Contact pressure distribution

Considering the case of a 1/5 scaled steel wheel and roller in contact, the curvatures at the contact point are given as: R_{w1}=0.1m, R_{w2}=infinite, R_{r1}=0.2m and R_{r2}=0.60m. With a normal force F_N between the wheel and roller of 285N the size of the contact patch and the pressure distribution are shown in Figure 2-3.

For cases that the wheel and rail are in contact at more than 1 point, the Hertzian model is not valid and other methods have been reviewed in [31].

2.2.2. Tangential force model

In the case of Hertzian contact, the creep force (tangential force) is a function of the creepage. The creepage between the wheel and rail can be divided into 3 components, longitudinal creepage, lateral creepage and spin creepage, which are defined as:

$$\gamma_x = \frac{v_x' - v_x}{v} \tag{2-24}$$

$$\gamma_y = \frac{v_y' - v_y}{v} \tag{2-25}$$

$$\omega_z = \frac{\Omega_z' - \Omega_z}{v} \tag{2-26}$$

where v_x, v_y and Ω_z are the actual longitudinal, lateral and spin velocities of the wheel; v'_x, v'_y and Ω'_z are the pure rolling velocities of the wheel and v is the forward velocity of the wheelset.

One commonly used model calculating the creep force is based on Kalker's linear assumption, which assumes the creep force and the creepage have a linear relationship when the creepage is very small. However, when the creepage is large, the creep force - creepage relationship becomes highly nonlinear and the creep force saturates at its limit, which is determined by the normal force and the friction coefficient at the wheel-rail interface.

The following equations show the creep force and creepage relationship using the Kalker's linear assumption and saturated by the equations developed by Johnson and Vermeulen.

$$F_x = -f_{11}\gamma_x \tag{2-27}$$

$$F_y = -f_{22}\gamma_y - f_{23}\omega_z \tag{2-28}$$

$$M_z = f_{23}\gamma_y - f_{33}\omega_z \tag{2-29}$$

$$F_x' = \begin{cases} \dfrac{\mu F_N F_x}{\sqrt{F_x^2 + F_y^2}}\left(\dfrac{\sqrt{F_x^2 + F_y^2}}{\mu F_N} - \dfrac{1}{3}\left(\dfrac{\sqrt{F_x^2 + F_y^2}}{\mu F_N}\right)^2 + \dfrac{1}{27}\left(\dfrac{\sqrt{F_x^2 + F_y^2}}{\mu F_N}\right)^3\right) & \sqrt{F_x^2 + F_y^2} \le 3\mu F_N \\ \dfrac{\mu F_N F_x}{\sqrt{F_x^2 + F_y^2}} & \sqrt{F_x^2 + F_y^2} > 3\mu F_N \end{cases} \tag{2-30}$$

$$F_y' = \begin{cases} \dfrac{\mu F_N F_y}{\sqrt{F_x^2 + F_y^2}}\left(\dfrac{\sqrt{F_x^2 + F_y^2}}{\mu F_N} - \dfrac{1}{3}\left(\dfrac{\sqrt{F_x^2 + F_y^2}}{\mu F_N}\right)^2 + \dfrac{1}{27}\left(\dfrac{\sqrt{F_x^2 + F_y^2}}{\mu F_N}\right)^3\right) & \sqrt{F_x^2 + F_y^2} \le 3\mu F_N \\ \dfrac{\mu F_N F_y}{\sqrt{F_x^2 + F_y^2}} & \sqrt{F_x^2 + F_y^2} > 3\mu F_N \end{cases} \tag{2-31}$$

The linear creep coefficients are defined as:

$$
\begin{aligned}
f_{11} &= \mathrm{E}(a,b)C_{11} \\
f_{22} &= \mathrm{E}(a,b)C_{22} \\
f_{23} &= \mathrm{E}(a,b)^{1.5}C_{23} \\
f_{33} &= \mathrm{E}(a,b)^{2}C_{33}
\end{aligned}
\tag{2-32}
$$

where a and b are the lengths of the semi-axis of the contact patch calculated by the Hertz method and the values of the Kalker coefficients C_{11}, C_{22} and C_{23} can be found from the table in [30], μ is the friction coefficient and F_N is the normal force between the wheel and rail.

Another model was developed by Polach to improve the accuracy especially when the creepage is large [32, 33]. In the Polach's model, the creep force F_γ is calculated by:

$$
F_\gamma = \frac{2\mathrm{F_N}\mu}{\pi}\left(\frac{\mathrm{k_A}\varepsilon_\gamma}{1+(\mathrm{k_A}\varepsilon_\gamma)^2} + \arctan(\mathrm{k_s}\varepsilon_\gamma)\right) \tag{2-33}
$$

where

$$
\varepsilon_\gamma = \frac{2\pi \mathrm{abC_{11}}}{4\mathrm{F_N}\mu}\gamma \tag{2-34}
$$

k_A and k_S are the reduction factors regarding to the different conditions between the wheel and rail surface. k_A is related to the area of adhesion, k_S is related to the area of slip and $k_S \le k_A \le 1$.

The contact shear stiffness coefficient C can be derived from Kalker's coefficients and creepage components by equation (2-35) and (2-36).

$$
C = \sqrt{\left(\frac{C_{11}\gamma_x}{\gamma}\right)^2 + \left(\frac{C_{22}\gamma_y}{\gamma}\right)^2} \tag{2-35}
$$

$$
\gamma = \sqrt{\gamma_x^2 + \gamma_y^2} \tag{2-36}
$$

It is also necessary to consider that the traction coefficient can bemodelled using the friction coefficient decreasing with an increasing slip velocity at the wheel-rail interface.. The relationship is expressed by the following equations [33]

$$
\mu = \mu_0((1-\mathrm{D})e^{-\mathrm{B}\gamma V} + \mathrm{D}) \tag{2-37}
$$

The creep curves with different friction coefficients are plotted in Figure 2-4 and the optimum values of creepage (γ_{opt}) which achieve maximum creep forces are also marked out.

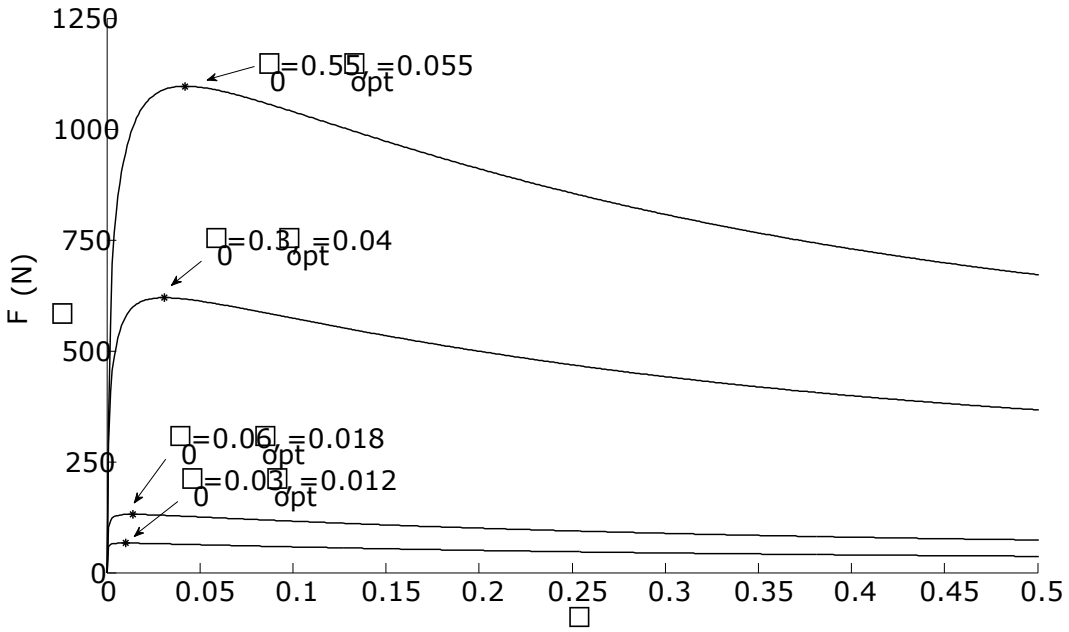

Figure 2-4 Creepage-creep force curves with different friction coefficients

In this simulation case, the normal force is 2kN and the forward speed is 10m/s. The values of B, D, k_A and k_S under different friction coefficients are listed in Table 2-1.

Table 2-1 Parameters of Polach model under different friction coefficients [34]

Parameter	Dry	Wet	Low	Very Low
k_A	1.00	1.00	1.00	1.00
k_S	0.40	0.40	0.40	0.40
μ_0	0.55	0.30	0.06	0.03
B	0.40	0.40	0.40	0.40
D	0.60	0.20	0.20	0.10

Other computer codes such as CONTACT (developed from Kalker's exact theory) and FASTSIM (developed from Kalker's simplified theory) have also been employed in cases where the contact condition and tangential forces are critical [35-37].

Many commercial simulation packages such as VI-Rail, Nucars, GENSYS, Simpack and Vampire have been developed based on the theories mentioned above. A benchmark exercise was made in [38], comparing the results of CONTACT, FASTSIM and these commercial simulation packages.

The case of a vehicle running on rollers rather than rail was also studied, terms of the normal force and creep force are discussed and modified in [39, 40].

2.3. Vehicle traction and its control method

The arrangement of railway vehicle traction systems is critical in applying model based FDI methods. There are primarily three different drive arrangements for railway

vehicles: axle-mounted, hollow shaft hugging and joint axle traction motor and their modelling methods are also discussed in [41].

Induction motors (IMs) are most commonly used as traction motors for railway vehicles as they have the advantages of simple construction, high reliability, ruggedness and low cost. To drive the IMs, power converters are required to transfer the supplied power (DC or high voltage AC) to a variable-frequency three-phase AC power. Different drive circuits are discussed in [42, 43] and some applications in Europe and Japan are presented in [44, 45].

Many control strategies have been developed to control the IMs and enable high performance under varying speed. The control strategies for the IMs can be classified as: scalar control, vector control or field oriented control (FOC) and direct torque control (DTC).

2.3.1. Scalar control

Scalar control is a control technique that concerns the magnitude of the control variables only and disregards the coupling effect of the induction motor. It is developed using the equivalent circuit of the IM (Figure 2-5) which is only valid in steady state. Therefore scalar control cannot offer highly accurate control but it is easy to implement and low-cost and therefore employed widely in industry. Generally, there are two kinds of scalar control techniques, which are volts/Hz control and scalar torque control [7].

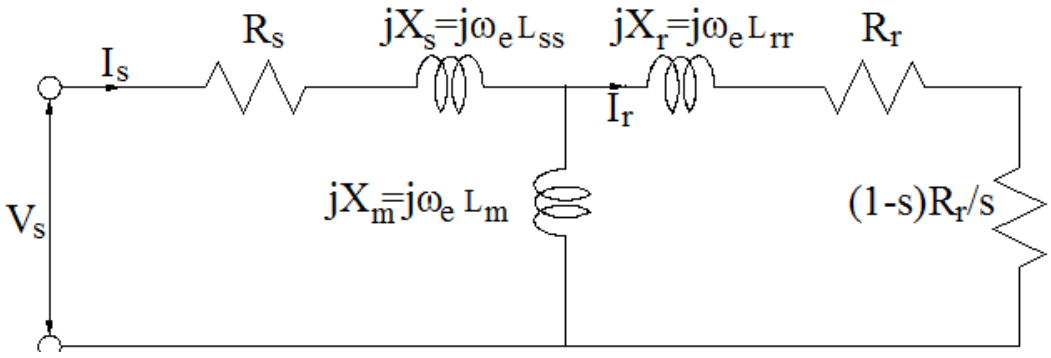

Figure 2-5 Equivalent circuit of the AC motor

In the equivalent circuit, the motor speed (ω_{motor}) and the electric power supply frequency (ω_e) has a proportional relationship when the slip ratio s ($s=1- n_p\ \omega_{motor}/\omega_e$) is assumed to be 0. Thus the motor speed can be controlled by altering the frequency of its power supply. To maintain the load capacity of the motor, the stator flux ($\psi_s=V_s/\omega_e$) is required to be constant, thus the ratio between the magnitude and frequency of the stator voltage should also remain constant. Therefore, the Volts/Hz control is developed by controlling the magnitude and frequency of the stator voltage.

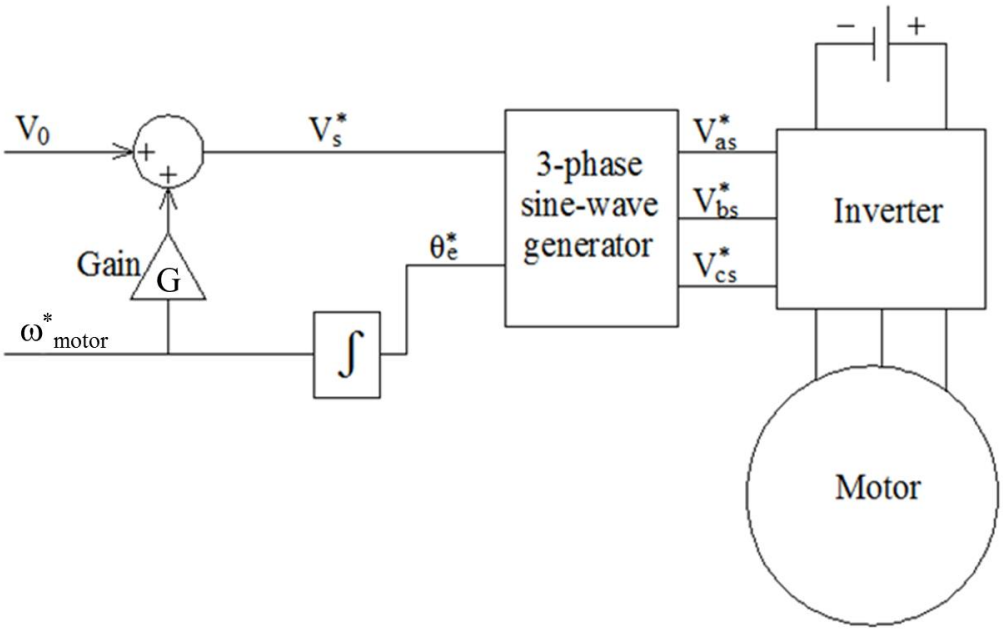

Figure 2-6 Open loop volts/Hz control

Figure 2-6 shows a typical scheme of an open-loop volts/Hz control system. The stator voltage command (V_s^*) is generated by the speed command (ω_e^*) command directly. V_0 is added to keep the flux and corresponding full torque available down to zero speed. V_0 is negligible at high frequency, so that the Volts/Hz ratio can still be treated as constant. The voltage commands for each phase (V_{as}^*, V_{bs}^* and V_{cs}^*) are generated by equation (2-38). AC power is supplied to the motor by the inverter according to the phase voltage commands.

$$\begin{cases} V_{as}^* = \sqrt{2}V_s^* \sin\theta_e \\ V_{bs}^* = \sqrt{2}V_s^* \sin(\theta_e - 120^\circ) \\ V_{cs}^* = \sqrt{2}V_s^* \sin(\theta_e + 120^\circ) \end{cases} \quad (2\text{-}38)$$

The Volts/Hz method has the disadvantage of potentially unstable stator flux and being vulnerable to changing machine parameters and incorrect volts/Hz ratio. To achieve better dynamic performance, scalar torque control, which regulates the motor by giving flux and torque command directly was developed. Figure 2-7 shows a typical scheme of this method, the flux and torque of the motor are estimated using the equivalent circuit and the rotor speed is measured by an encoder. The flux loop, the torque loop and the speed loop are used together to improve the accuracy of this method and eliminate the problems of the Volts/Hz method. However, as the stator flux is related to the torque this coupling effect will lead to a slower torque response and more difficulty in achieving high accuracy.

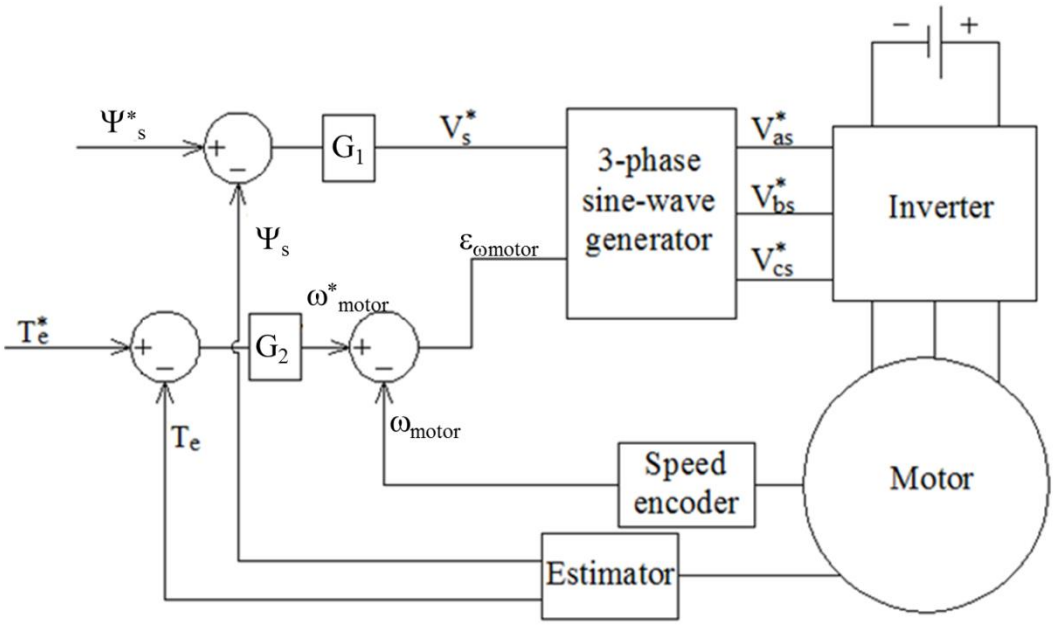

Figure 2-7 Scalar torque control

2.3.2. Vector control

Due to the complex mechanism of the IM, it is difficult to control the motor precisely as the torque has both flux and speed components in its original ABC frame, which is used in scalar control. Vector control was first proposed in [46, 47]. In vector control, the motor is modelled in a dynamic d-q coordinate system, which rotates synchronously with the rotor flux vector, as shown in Figure 2-8.

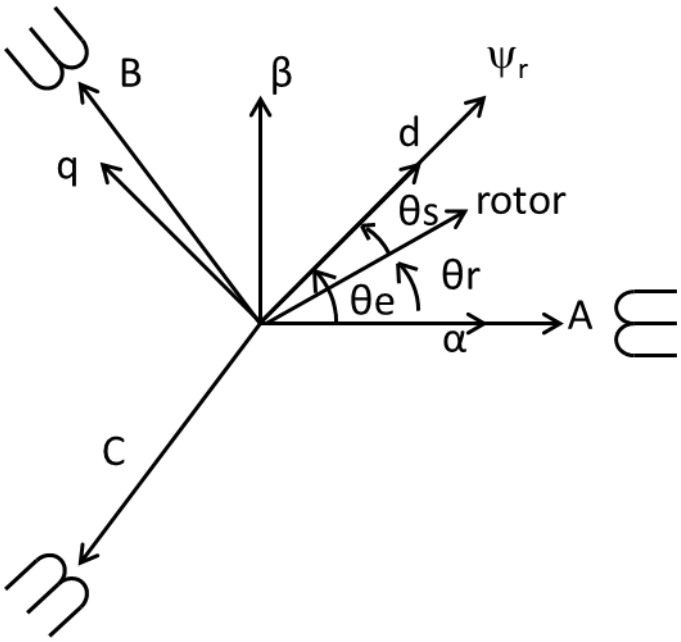

Figure 2-8 d-q frame of the motor

In the d-q frame, the dynamic equations of the IM are:

$$T_e = \frac{3}{2}(\frac{n_p}{2})\frac{1}{L_r} I_q \psi_d \quad (2\text{-}39)$$

$$\psi_r = \psi_d = L_m I_d \quad (2\text{-}40)$$

It can be seen from these equations that T_e and ψ_d can be controlled separately by I_q and I_d. Therefore, in the d-q frame, the current and flux of the motor are decoupled into the speed and flux components independently, which enables the IM to be controlled like a separately excited DC motor. The vector control method is based on the orientation of the rotor flux, thus it is also referred as field oriented control (FOC). The orientation of the rotor flux can be determined by direct calculation or through estimation of the slip frequency.

Direct field orientation control (DFOC) can be achieved by measuring the stator voltage, current and speed signals. Two different models are used, which are the voltage – current model and the current – speed model. These two models are always used together as the voltage – current model is not accurate during low speed and the current – speed model is not accurate during high speed.

For the indirect field orientation control (IFOC) method, the flux orientation (θ_e) is comprised of the slip angle (θ_s) and rotor angle (θ_r), as shown in Figure 2-8. The rotor angle can be measured using the encoder and the slip angle needs to be estimated based on the dynamic relationship of the motor. The DFOC estimates the flux position in the stator coordinate and the IFOC estimates it using the slip and rotor speed. While the DFOC requires rotor flux position sensors, which increase the total cost and also reduce the reliably of the controller, the IFOC has become more popular.

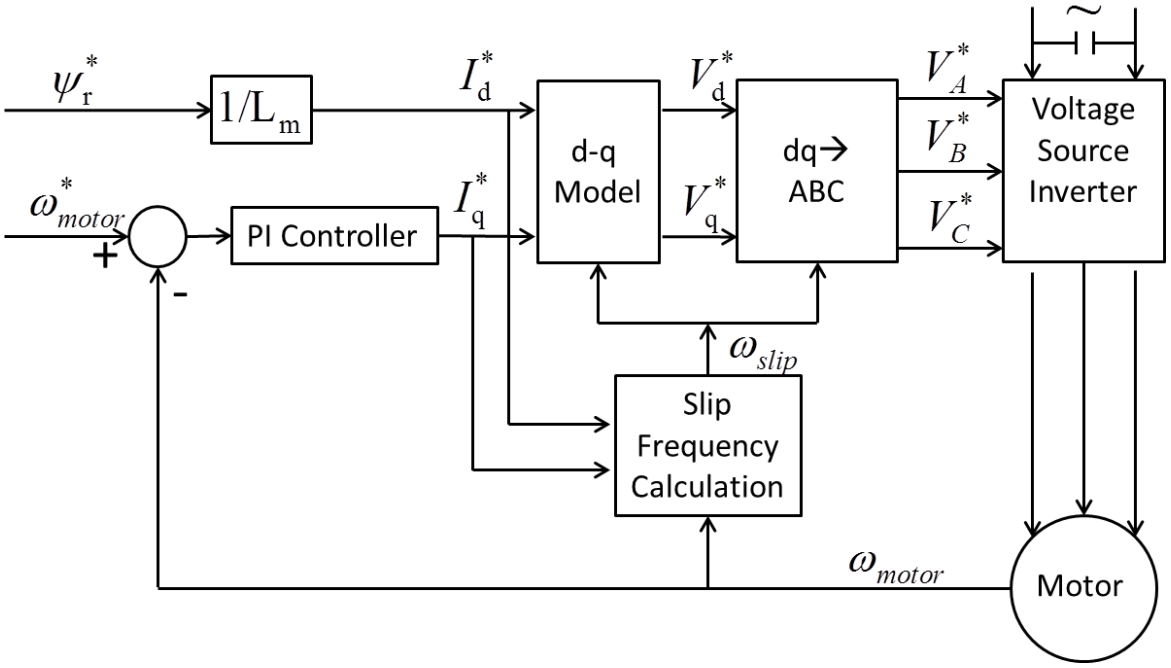

Figure 2-9 Indirect field oriented control scheme

Figure 2-9 shows a typical IFOC scheme, in which the rotor flux and motor speed commands are given to control the motor. A PI (proportional - integral) controller is often used to provide a better dynamic performance. The I_d and I_q commands are generated based on equation (2-39) and (2-40). The slip frequency can be calculated using the current commands and the rotor flux can be oriented.

$$\omega_{slip} = \frac{R_r I_q^*}{L_r I_d^*} \tag{2-41}$$

$$\omega_e = \omega_{motor} + \frac{R_r I_q^*}{L_r I_d^*} \tag{2-42}$$

For a voltage source inverter, the current commands need to be converted into voltage commands using equation (2-43) and (2-44).

$$U_d^* = R_s^* I_d^* \tag{2-43}$$

$$U_q^* = R_s^* I_q^* + \omega_{motor} L_s I_q^* \tag{2-44}$$

Park's transformation [48] then converts the commands from the dq frame to the ABC frame as:

$$\begin{bmatrix} I_d \\ I_q \end{bmatrix} = \begin{bmatrix} \cos(\theta_e) & \cos(\theta_e - 2/3\pi) & \cos(\theta_e + 2/3\pi) \\ -\sin(\theta_e) & -\sin(\theta_e - 2/3\pi) & -\sin(\theta_e + 2/3\pi) \end{bmatrix} \begin{bmatrix} I_a \\ I_b \\ I_c \end{bmatrix} \quad (2\text{-}45)$$

2.3.3. Direct torque control

Direct control (DTC) was first developed in [49, 50] which replaced the decoupling technique used in the FOC by a "bang-bang" controller. A conventional DTC scheme is shown in Figure 2-10.

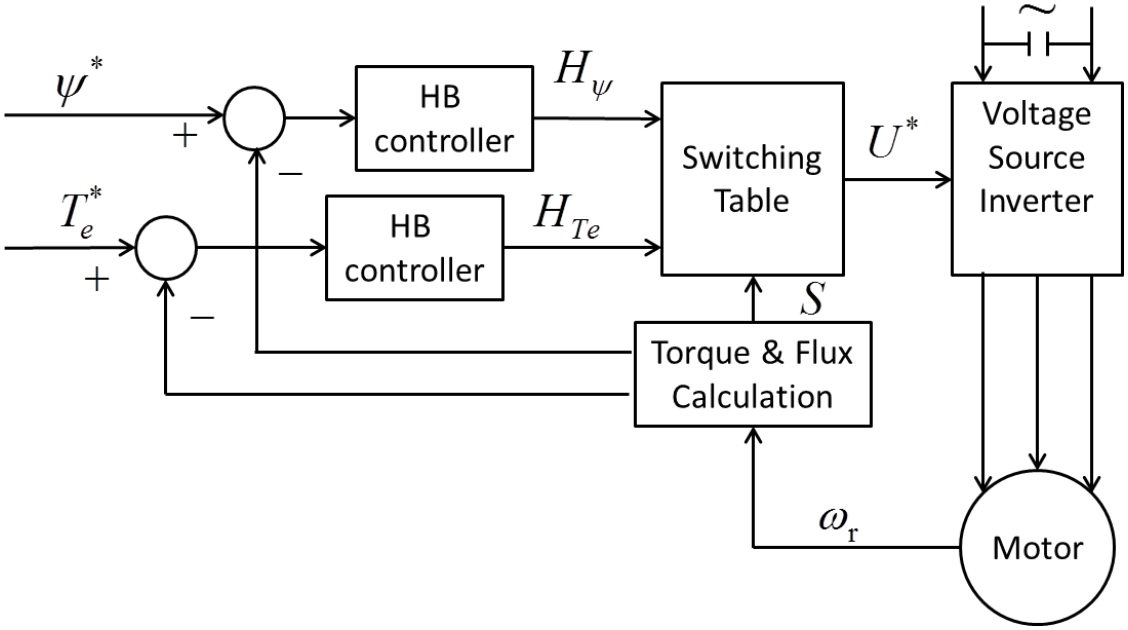

Figure 2-10 Conventional direct torque control scheme

In this method, the electric torque and flux of the motor is estimated by equation (2-39) and (2-40). Based on the flux orientation, the space is divided into 6 sectors, shown in Figure 2-11.

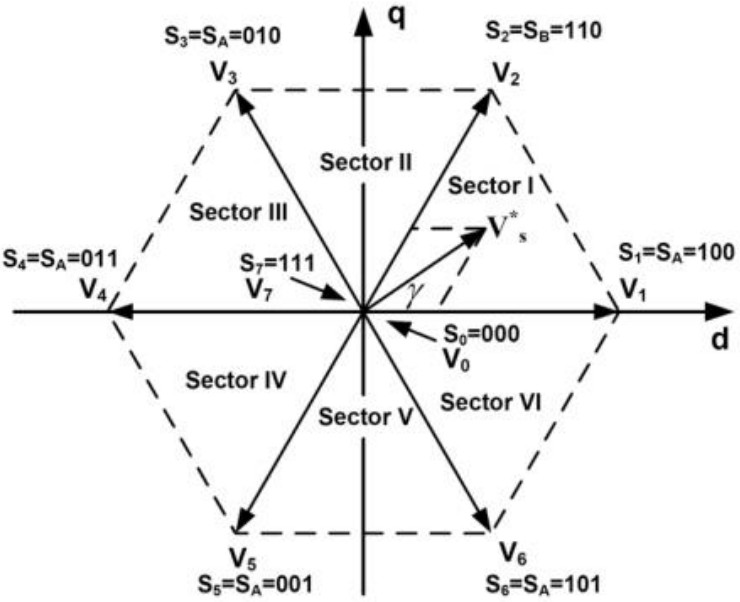

Figure 2-11 Voltage vectors

The estimated flux and torque are compared with their reference values and then fed in two hysteresis band (HB) controllers (Figure 2-12). Then a switching table is used to choose the appropriate voltage command from the HB controller signals and the flux. In this way, the stator flux is controlled between the high and low limit of the HB controller.

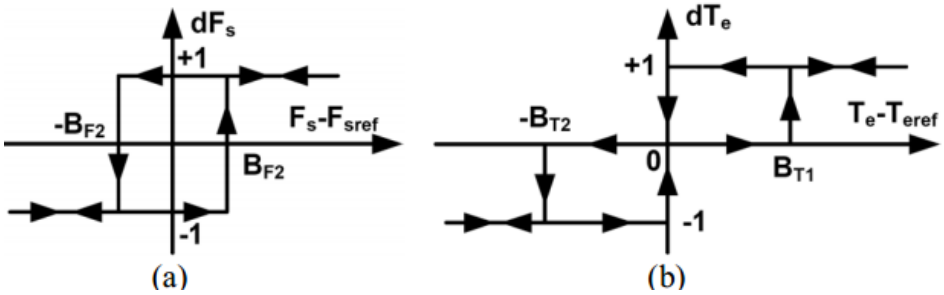

Figure 2-12 Hysteresis band controller (a) Stator flux (b) Torque

Table 2-2 Switching Table

H_ψ	H_{Te}	S1	S2	S3	S4	S5	S6
1	1	V2	V3	V4	V5	V6	V1
	0	V7	V0	V7	V0	V7	V0
	-1	V6	V1	V2	V3	V4	V5
-1	1	V3	V4	V5	V6	V1	V2
	0	V7	V0	V7	V0	V7	V0
	-1	V5	V6	V1	V2	V3	V4

Comparative study of the FOC and DTC methods is shown in [51], proving that DTC is less parameter dependent thus more robust and easier to be implemented. The

disadvantages of the DTC are that torque and flux ripples are always generated during low speed.

2.4. Applications of FDI techniques in railway vehicle systems

Model based FDI methods have been widely used in the chemical industry, automobiles, actuators and suspension systems, which are reviewed in [52]. Applications in the railway industry are summarized in [3], which showed that little research has been done in this field. Proposed methods of using FDI methods in the estimation of the wheel-rail profile and creep force (friction coefficient) will be discussed in detail in the following sections, as these are the focuses of the research. There are also methods monitoring suspension parameters of the vehicle, as shown in [53-55].

2.4.1. Estimation of the wheel-rail creep force

Methods used in estimating the wheel-rail creep force can be classified into two categories: lateral model based and torsional model based.

The feasibility of using a Kalman filter in estimating low-adhesion conditions using vehicle lateral dynamic responses was explored in [34]. Two different Kalman filters were used in this research, the first one focused on estimating the creep coefficient directly but the result was not satisfactory; then another more complex Kalman filter was built aiming at estimating the creep force and detecting the change of creep coefficient by further analysis of the vehicle lateral responses. However, the proposed methods cannot give an accurate enough estimation either of the creep coefficients or the creep forces, thus the methods are only suitable when the change in the friction coefficient is large enough.

An improved method to estimate wheel-rail creep forces was proposed in [56], where a more complex dynamic model was used to build the Kalman filter. In this method the effects of friction coefficient and track irregularities on the estimation results were analysed. The results showed that the estimation was only accurate when the friction coefficient was high and the track irregularity amplitude was low.

A multi-filter method offering a more accurate estimation of the friction coefficient between the wheel and rail profile was shown in. Multiple models of different friction coefficient of a single wheelset system were built to formulate the Kalman filters. This method judges the friction coefficient by comparing the root mean square of the estimating errors of these Kalman filters, but the accuracy was still not satisfactory and had the problem of having residuals too close to each other. Accuracy can be improved by increasing the number of filters but will result in an increase in computing time and still cannot avoid the problem of choosing from residuals of similar values.

Besides using the lateral model of the vehicle, there has also been research focused on the torsional/longitudinal dynamics of the vehicle.

Two algorithms were proposed in [59] to estimate the friction coefficient at the wheel-rail interface, but the estimation error was found to be large when sudden changes occurred. The EKF method was used in both of the algorithms as the longitudinal model was nonlinear.

A combination of the Luenberger observer and integrator was developed to estimate creep force and identify the skidding (sliding) phenomenon between the wheel and roller and was validated through experiments on a scaled roller-rig [60]. In the research, the sliding phenomenon was identified based on the sudden and significant change of the estimated friction force. The skidding phenomenon was then more thoroughly studied with the implementation of the 2nd order Luenberger observer [61]. The interaction between the wheel-roller slip and the torsional oscillations of the driving system was studied using spectrum analysis, showing that the creep force was influenced by low frequency harmonics. These two pieces of research focused only on the skidding phenomena and did not analyse the creepage or friction coefficient.

2.4.2. Estimation of wheel-rail profiles

Preliminary work estimating the nonlinear conicity of the wheel profile using observer based methods was studied in [62, 63]. Results obtained from Kalman filter and Least Mean Squares approaches were compared and analysed. The estimation results were in good agreement with the actual values thus proving the potential for developing more practical methods in the estimation of the wheel conicity. Similarly, another method of estimating the wheel-rail conicity was shown in [64] using a Kalman filter.

To estimate the vertical profile of the rail, an approach using inertial methods was proposed [65]. A vertical model of the vehicle was built and the vertical acceleration of the wheel axle was measured.

Though the results proved that the standard deviation and magnitude scale were similar to the real case, there were still some differences in the magnitude and shape of the rail profile.

2.4.3. Estimation of the motor traction system

Few FDI methods have been developed considering the traction motor as part of the vehicle dynamic system. Therefore it is important to study model based FDI methods for induction motors. Condition monitoring methods for the motor traction system are mostly focused on speed sensorless control of motors using EKF [66-68].

An approach estimating the speed and electric torque of the induction motor of a torsional system was proposed in [69]. The torsional model includes an induction motor and a constant load. A Kalman filter was used to estimate the electric torque of the motor. The simulation and experimental results of this method showed good agreement

with their real values. A control system was then developed based on the estimation of the system.

A method identifying the parameters of a turbine-generator was developed in [70]. This method is based on a torsional model of the driving system. The electric torque and mechanical torque of the motor was measured and the rotating speed of the components in the turbine-generator system was estimated using a Kalman filter. The mass and inertia of the components were also identified using trajectory sensitivities and least squares method.

2.4.4. FDI based re-adhesion control

In railway vehicle traction systems, it is necessary to reduce the occurrences of the excessive creepage between the wheel-rail (roller) surfaces to avoid wheel slip/slide and a decrease in traction effort, plus possible worse riding comfort, increase in wheel wear and noise. Large creep mostly occurs when the applied tractive effort exceeds the maximum available adhesion, during acceleration or deceleration. This phenomenon occurs more commonly when the wheel-rail (roller) surfaces are wet or contaminated with oil or leaves, as the friction coefficient may drop to very low levels.

To avoid this issue, re-adhesion control strategy has been studied and many different algorithms have been proposed [71-79]. In these algorithms, the vector control method is most commonly adopted, while the major differences lie in the way of detecting creepage and generating the torque command.

Yasuoka et al [71] presented a method in which slip is detected by comparing the speed difference between the wheel and the vehicle body (estimated by averaging the speed of all its axles).Then a torque compensation signal is generated using the estimated slip. Kim et al [72] suggested a model based re-adhesion control which treats the creep force as the mechanical load of the traction motor and the creepage force is estimated by a Kalman filter. Matsumoto [73] and Kawamura [74] investigated a single-inverter for a multiple-induction-motor drive system, which uses the estimated adhesion force to adjust the torque command and suppress the slip. The advantages for these applications are that they can regulate the traction system to work around the peak of the creepage – creep force curve, but require knowledge of the friction coefficient and the vehicle speed, which are both hard to be measured accurately. Kadomaki et al [75] and Shimizu [76] evaluated anti-slip re-adhesion control based on speed-sensorless vector control and disturbance observer technique with a similar principle with the previously discussed work. However, it is questionable about the reliability of the sensorless control as its fundamental assumption is that the traction motor flux is constant which is only valid in certain cases. Spiryagin et al [77, 78] included the complex relationship between the creepage and creep force in the observers in his proposed method, to improve the results of previous research. The friction coefficient is assumed to be measurable from

wheel – rail noise and the vehicle speed is measurable by GPS. Then the re-adhesion controller is proposed using the normal load, friction coefficient, vehicle and wheel speed to estimate the actual creep force, hence generating the control commands which achieve its optimum performance. Mei [79] used wheelset torsion vibration analysis to detect slip between wheel and rail which has an advantage of eliminating effort in the estimation of creepage and creep force using state observers.

2.5. Roller rig design

Both full size and scaled roller rigs were used in developing bogies for the Shinkansen in Japan in the 1950s and since then the roller rig applications have been more popular. Compared to field tests, full size roller rigs have the advantage that the experiments are not affected by the weather condition and it is much easier to study individual problems or to produce particular conditions. Some examples such as the DB (Deutsche Bahn) roller rig in Munich are listed in [39].

Despite its advantages, a full size roller rig requires high manufacturing, operating and maintenance cost and its parameters are difficult to change. The development of scaled roller rigs was motivated by these disadvantages. To transfer the experimental results from the scaled model to full scale, similarity laws need to be addressed. There are several approaches to scaling. Dimensionless groups can be established by applying dimensional analysis and scale factors can be derived from them [80-82]. Inspectional analysis has also been used to maintain similarities by studying the equations of motion of the system.

Some applications around the world are reviewed. The first one is the test rig of the institute for Robotics and System Dynamics of DLR [83-85] (German Aerospace Centre, German: Deutsches Zentrum für Luft- und Raumfahrt e.V.). This roller rig is 1/5 scale so the lateral distance between the rollers is 287mm (=1435/5). The rollers are driven by a DC – controlled disc motor through a tooth belt. In the plan view of the roller rig (Figure 2-13), it can be seen that the roller axle is built with a large diameter tube which provides high torsional stiffness and large moment of inertia in order to simulate the ideal track and eliminate the disturbance of the rotating velocity of the rollers. The distance between the roller axles can vary from 400mm to 560mm, corresponding to different bogie models. The maximum speed is between 900rpm and 1100rpm, corresponding to different rolling resistance of the bogie models.

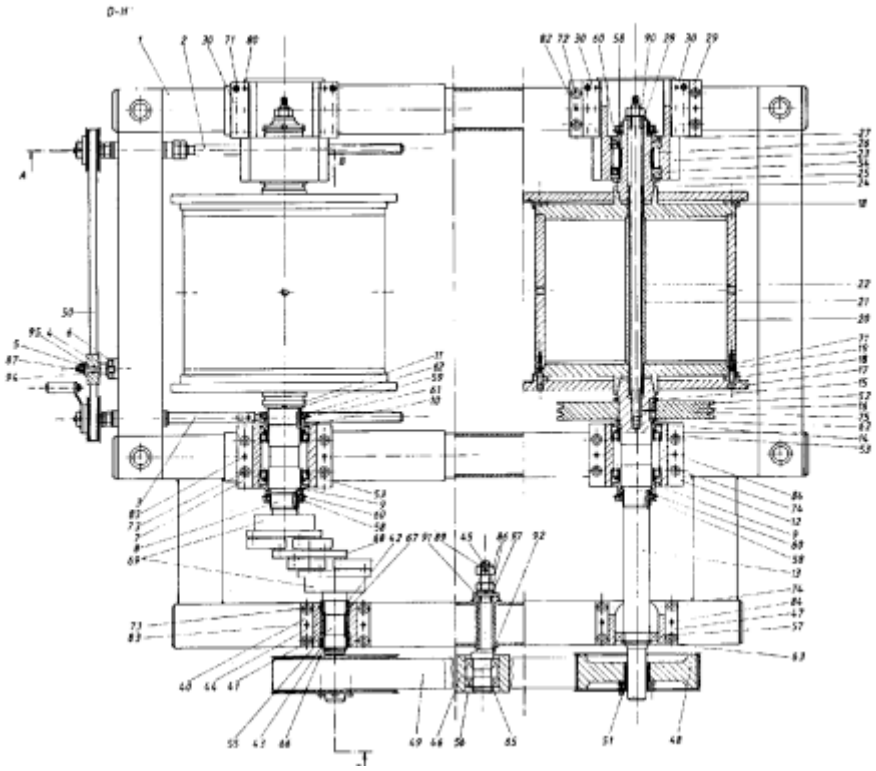

Figure 2-13 Plan view of the DLR roller rig [85]

Another roller rig (Figure 2-14) was designed by MERLIN GERIN to test linear motors for the BERTIN AEROTRAIN transport vehicle in the 1970s and is located in the 'Institut National de Recherche sur les Transports et leur Securite' (INRETS). It is equipped with a 13m diameter, 40 ton roller which is driven by a linear two megawatt asynchronous motor. The maximum speed is 250km/h. Despite the huge size, the flywheel is designed to support 1/4 scale bogies, rather than the full size ones.

Figure 2-14 The INRETS roller rig [86]

The Rail Technology Unit at Manchester Metropolitan University (now moved to Huddersfield University and changed its name to the Institute of Railway Research) has also built a 1/5 scale roller rig for suspension design (Figure 2-15) [87]. It has two pairs of rollers which are interconnected by a belt and driven by a single phase AC motor. The

scale speed is up to 250mph. Servo-hydraulic actuators at the end of the roller axles can move the rollers laterally and create a yaw angle to simulate track irregularities and curving. The wheelbase and gauge between the rollers can be changed easily for different research projects.

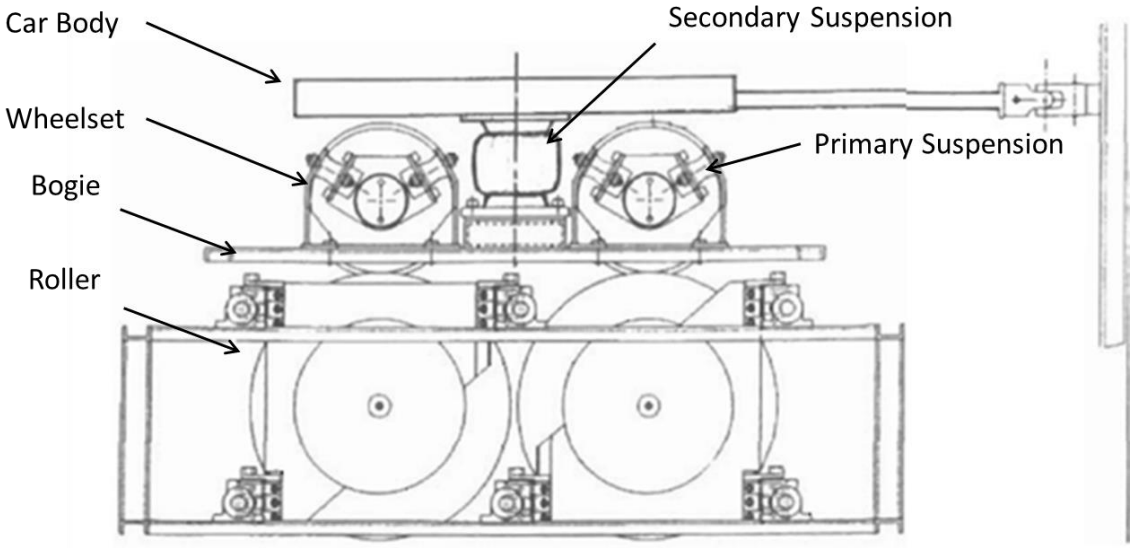

Figure 2-15 Side view of the MMU roller rig [87]

Table 2-3 Comparing of the scaling strategies of the DLR, INRETS and MMU roller rig[39]

SCALING:	MMU	DLR	INRETS	Comments
		geometry		
length	5	5	4	vehicle geometry
cross section	25	25	16	
volume	125	125	64	
		material		
density	1	0,5	1	weight
mass	125	62,5	64	weight
inertia	3125	1562,5	1024	inertial forces
elasticity	G, E, cij	approximat.	G, E, cij	Hookes law
		parameters		
time	1	$\sqrt{5}$	4	
frequency	1	$1/\sqrt{5}$	1/4	
velocity	5	$\sqrt{5}$	1	dynamic range
acceleration	5	1	4	dynamic forces
stress	25	5	1	contact pressure
strain	5	5	1	elastic behaviour
stiffness	125	12,5	4	suspension
		forces		
inertial forces	625	62,5	16	
grav. forces (weight)	reduced 1/5, soft springs	62,5	multipl. ×4 (air jack)	contact normal load
spring forces	modified	62,5	scaled	spring scaling
dry frict. forces	modified	62,5	scaled	contact forces, damping
viscous damping forces	modified	62,5	no	anti-yaw dampers (if any) structure damping

These three applications are scaled using different strategies. The DLR roller rig is designed to investigate the nonlinear lateral phenomenon so that it is scaled to keep the similarity in the lateral dynamic equation. The INRETS roller rig aims at representing the wheel rail contact patch so the scale factor for the stress is unity. The MMU roller rig

focuses on the frequency analysis of the vehicle; therefore the scaling factor for time is set as 1. Details of scaling factors for these three roller rigs are compared in Table 2-3.

2.6. Summary of the literature review

State observers to monitor dynamic systems are firstly reviewed. Different models for the railway vehicle and its traction system are studied as the monitored system must be modelled accurately using the model based FDI method.

Related previous research projects and applications using state observers to estimate railway vehicle and traction motors have also been reviewed. Previous research activities in estimation of wheel-rail friction require many measurements and cannot offer accurate estimation most of the time. Another problem is that most of the proposed methods are developed based on computer simulations, and only few of them have been validated against experiments. Some successful traction motor estimators have been proposed , which could offer precise estimation of the motor behaviour with simple load conditions. Nevertheless, these previous efforts do still show potential for using a state observer to estimate the wheel-rail friction coefficient using the signals of the traction motor. Re-adhesion control methods are then studied. None of the previous research projects have included a precise knowledge of the friction coefficient at the wheel-rail interface. Therefore, given accurate friction estimation, the performance of the re-adhesion estimator could be improved significantly.

A test rig is required in this project to validate the developed method. Therefore, in the last part of the literature review, previously designed test rigs around the world are reviewed to guide the test rig design.

3. Roller rig design

Although a roller rig existed at Manchester Metropolitan University it was decided to build a new one for this project. In the existing roller rig (Section 2.5), the rollers are driven by a single phase AC motor and the wheelsets are driven by the rollers through the creep force at the wheel-roller interface. This driving arrangement cannot simulate the traction behaviour of the railway vehicles so in order to use traction motor signals to detect and identify faults for the vehicle, the roller rig designed for this project uses two induction motors to drive the wheelsets directly. This arrangement brings in a closer dynamic relationship between the bogie and its driving system. Furthermore, a bogie with the wheelsets driven by traction motors instead of rollers is also closer to real vehicles, which makes it easier to transfer the research developments to practical applications.

3.1. Introduction

The roller rig is 1/5 scale to keep the dimensions and forces suitable for construction and laboratory installation. It is desirable to have the scaled roller rig and full size vehicle showing the same frequency components, which makes the analysis convenient. Therefore the scale strategy is the same as the pervious design, which keeps the time factor at unity, as is discussed in Section 2.5. Steel is used to construct the roller rig, so the material properties are similar to those of full size vehicles.

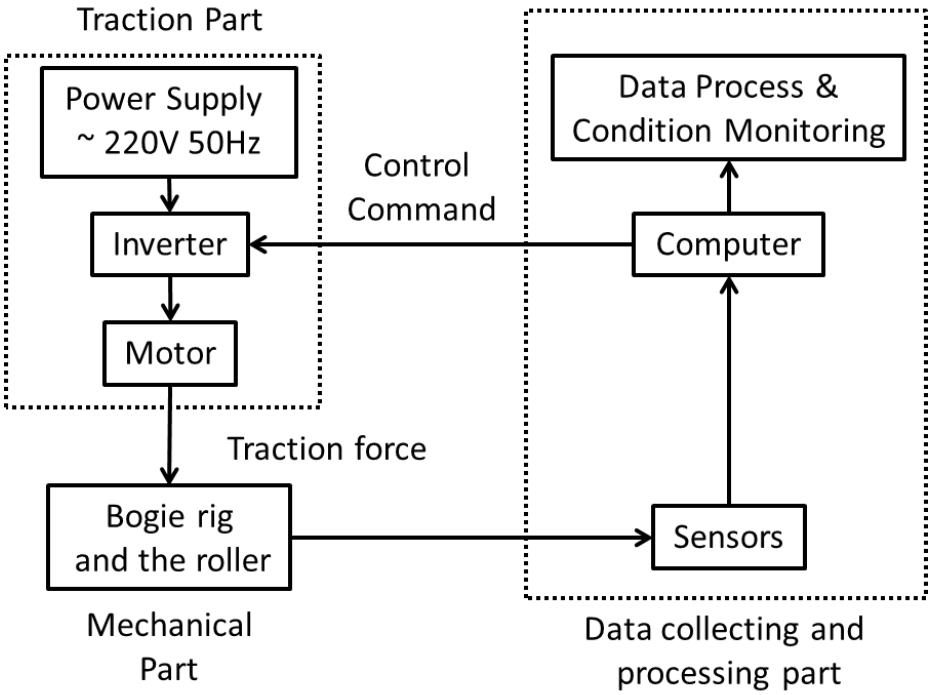

Figure 3-1 Overall lay out of the roller rig system

The whole roller rig system is comprised of three major parts, which are the mechanical part, the traction part and the data collecting and processing part. An overall system structure is shown in Figure 3-1. In the mechanical part, a bogie-wheelset rig is mounted on rollers representing the vehicle-rail scenario. The rotating speed of the wheelset and the rollers are measured by rotary encoders and together with the motor signals (stator voltage, current and speed) are fed into the computer using a data acquisition card. The measured data are processed to generate control commands for the inverter, which controls the motor to drive the wheelset. In this way, the mechanical and electrical components are connected in a closed loop.

3.2. Mechanical structure of the roller rig

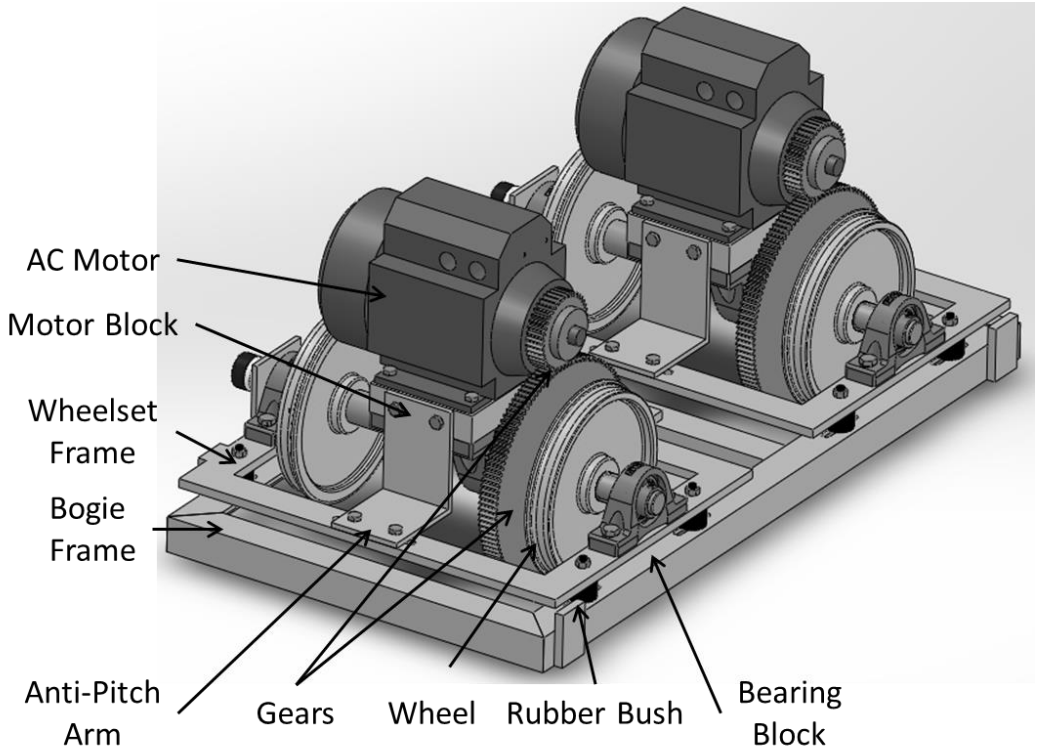

Figure 3-2 Bogie assembly

The rig consists of a bogie frame and two wheelsets, as shown in Figure 3-2. Each wheelset is connected to a rectangular wheelset frame with two self-aligning ball bearing blocks on the end of each wheel axle. The wheelset frames are connected to the bogie frame with 4 rubber bushes. The rubber bushes represent the primary suspension of the vehicle, providing stiffness and damping longitudinally, laterally and vertically. The bogie frame is made of angle section steel and the wheelset frame is made of flat section steel, providing a stable structure for the rig. The bogie is supported on two roller axles. Each roller axle is rigidly connected to the roller frame with two self-aligning ball bearing blocks at each end. The wheel profile is a 1/5 scaled UK P8 worn profile. The roller profile is a 1/5 scaled BS 113a worn profile with no cant. The diameter of the wheel at the contact point is 200mm and the rolling diameter of the roller is 400mm. This large roller diameter was chosen to reduce the influence of the de-crowning effect described in [40]. The mass and inertia properties for the parts of the roller rig are listed in Table 3-1. As a summary, the total mass of the bogie is 116.1 kg and the normal force between each wheel and roller is 284.45 N. The rotating inertias of the wheel and roller axles are 0.05 kgm^2 and 0.35 kgm^2, respectively.

Table 3-1 Mass and Rotating Inertia of the Roller Rig Components

ITEM NO.	ITEM NAME	QUANTITY	Mass (kg)	Inertia ($kgmm^2$)

1	WHEEL AXLE	2	2.62	335.86
2	WHEEL	4	3.38	19549.43
3	BOGIE FRAME	2	10.59	N/A
4	SPACER 1	4	0.06	11.43
5	SPACER 2	2	0.04	8.16
6	MOTOR BASE	2	4.98	N/A
7	WHEELSET FRAME	2	4.67	N/A
8	ANTI-PITCH ARM	2	0.77	N/A
9	ENCODER HOLDER 1	2	0.26	N/A
10	ENCODER SHAFT	4	0.04	0
11	GEAR 1	2	6.94	50352.86
12	GEAR 2	2	0.88	678.80
13	AC MOTOR	2	15.00	N/A
14	PLUMMER BLOCK 1	4	0.72	N/A
15	PLUMMER BLOCK 2	4	1.45	N/A
16	ROLLER AXLE	2	3.89	679.19
17	ROLLER	4	8.56	172598.36
18	SPACER 3	2	0.08	23.43
19	PULLEY 1	4	0.5	1101.09
20	PULLEY 2	4	0.02	2.78
21	PULLEY SHAFT 1	2	0.06	1.77
22	PULLEY SHAFT 2	2	0.14	3.70

The longitudinal movement of the rig need to be restrained to prevent it from rolling off the rollers and maintaining the other degrees of freedom in the meantime. To achieve this, the bogie is connected to the roller frame through a special linkage, as shown in Figure 3-3. One end of the link is bolted in the centre of the bogie frame and the other end is bolted to the roller frame. This link uses 2 spherical joints along the longitudinal axis and the vertical axis to enable the required movements of the bogie.

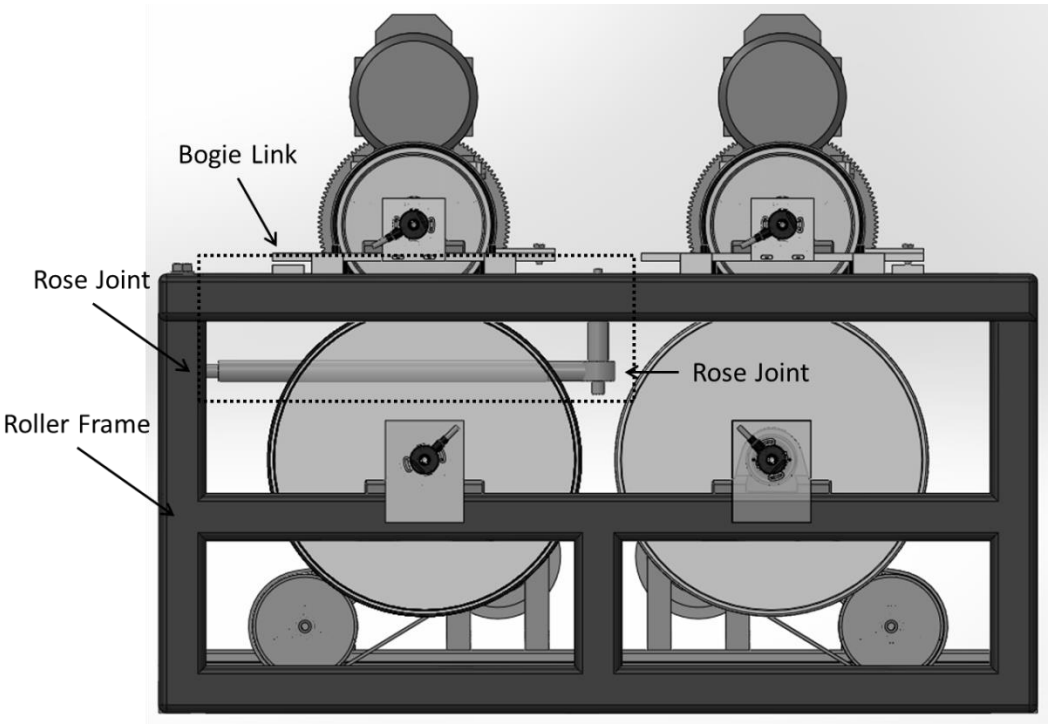

Figure 3-3 Side view of the roller rig

Two permanent magnetic DC motors, which are used as generators, are connected to the roller axles to provide traction load to the AC motors. Two sets of timing belt pulleys are used to increase to the speed at the DC motor (generator). For each pair of the pulleys, the bigger one has 84 teeth and the small one has 20 teeth, thus the effective transmission ratio is $(84/20)^2=17.64$. The belt width is 10mm, the pitch is 5mm and the length is 800mm.

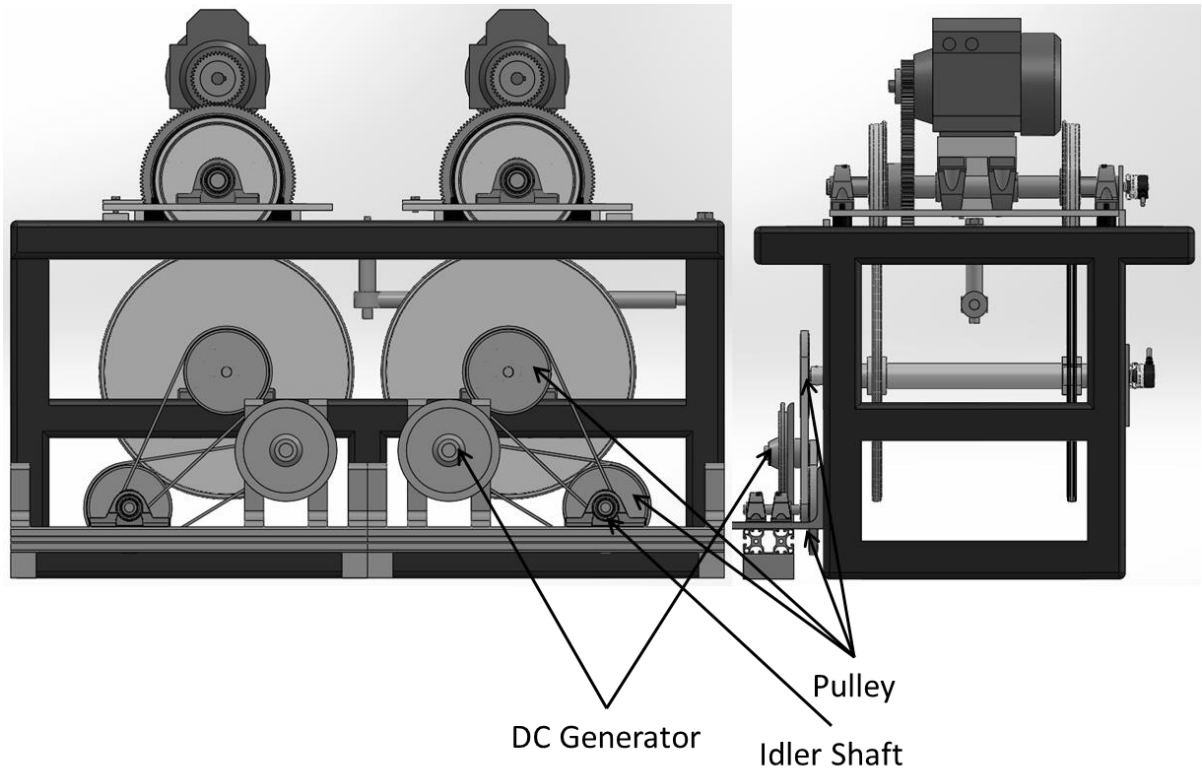

Figure 3-4 Transmission to the DC Generator

The transmitted torque and speed ratios between all the shafts from the AC motor to the DC generator are summarized in Table 3-2.

Table 3-2 Summary of the roller rig transmission

	Speed	Torque	Transmission Ratio
AC Motor	ω_{motor}	T_{motor}	3:1
Wheel	$1/3\omega_{motor}$	$3T_{motor}$	2:1
Roller	$1/6\ \omega_{motor}$	$6T_{motor}$	1:17.64
DC Generator	$2.94\ \omega_{motor}$	$0.34T_{motor}$	

3.3. Induction motors and the inverter drives

Two 750W 3 phase AC motors are selected to drive the wheelsets. The rated motor parameters are shown in Figure 3-5.

Figure 3-5 Motor label

'Y' connection is used in the motors. The rated torque of the motor is calculated as follow:

$$T_{rated} = 9550 P_{rated} / n_{rated} = 4.78 Nm \qquad (3\text{-}1)$$

Each motor is powered by a SIEMENS SIMOVERT MASTERDRIVE inverter. The output voltage of the inverter is rated as 380-480V at 50/60Hz and the rated power is 2.2kW. The inverter employs a Vector control (VC) function, which enables the following control methods:

- Vector control with speed encoder.
- Vector control without speed encoder.
- Volts/Herts control.

For this application the vector control with speed encoder is chosen as discussed in Section 2.3.2. The block diagram of this control scheme includes five different parts, which are setpoint channel, speed controller, torque/current limit, current controller and gating unit, as shown in Figure 3-6. The detailed function blocks of the control scheme are listed in Appendix C

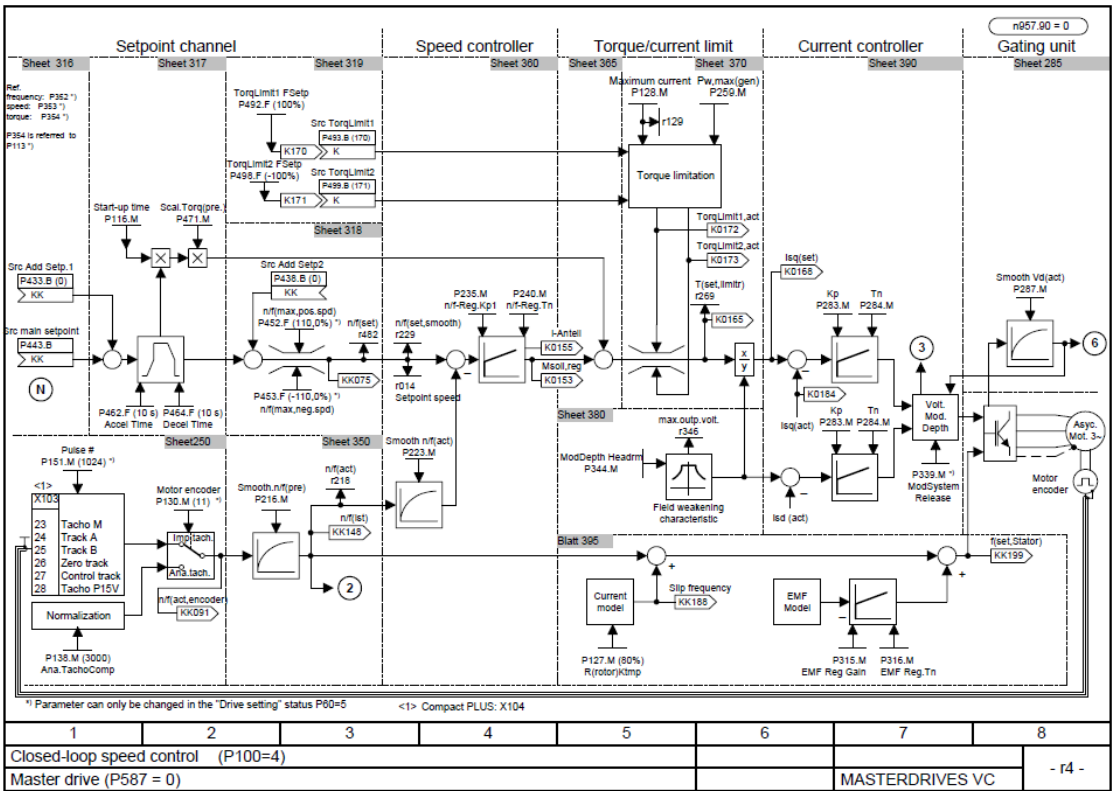

Figure 3-6 Block diagram of the control strategy [89]

The inverter can be controlled via different methods, such as PMU (basic control panel, Figure 3-7 (left)), OP1S (advance control panel, Figure 3-7 (right)), computer and PLC (programmable logic controller). The PMU is a basic control unit which is connected to inverter by a parallel bus cable. It can only change control commands by the raise, lower and reversing keys thus making it very difficult to operate the inverter freely. OP1S is a more advanced control panel which communicates with a single inverter via the RS-485 serial interface using the USS protocol (Universal Serial Interface Protocol). OP1S can also operate a series of inverters (up to 32) via the industrial bus. The inverter can also be controlled by computers via the RS-232 serial interface and USS protocol for individual control or PROFIBUS (Process field bus) for bus control. PLCs are also popular in the industry, especially for controlling a series of inverters automatically. Profibus is also used in the communication between the PLC and inverters.

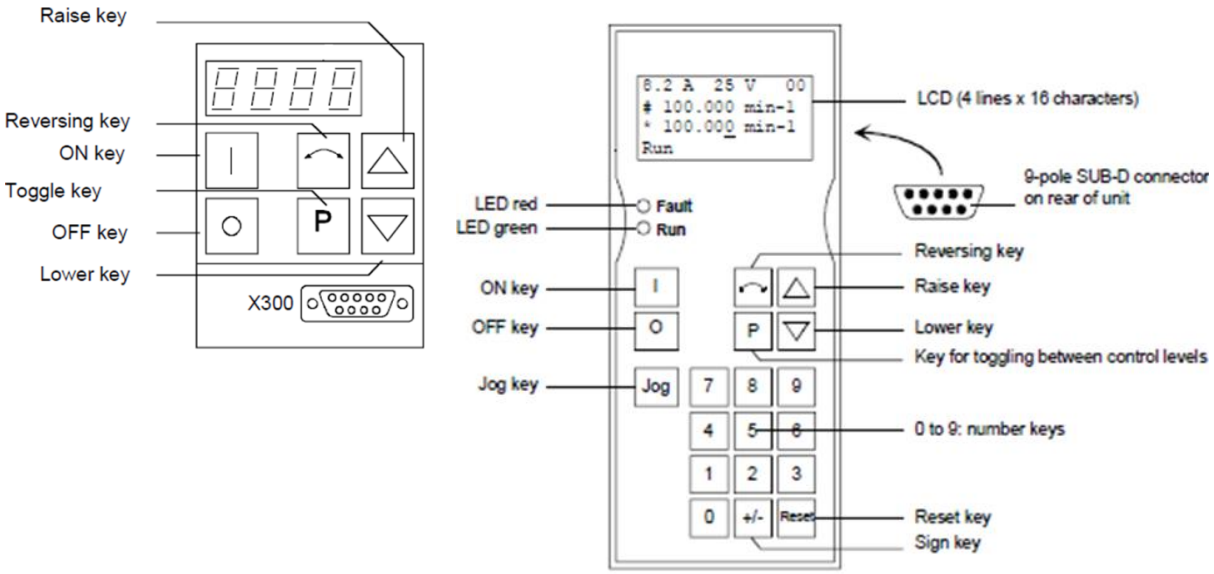

Figure 3-7 PMU (left) and OP1S (right) control panel [89]

For this roller rig application, automatic control based on different measurements is required and it is also important to keep the system simple. Therefore a computer is used to control the inverters via PROFIBUS.

PROFIBUS is a standard for field bus communication in automation technology and was first promoted in 1989 by BMBF (German department of education and research) and then used widely in the industry including Siemens. In 1993 a much faster protocol called PROFIBUS DP (Decentralized Peripherals) was introduced for communication between the PROFIBUS masters and their slaves. For the roller rig drive system, the PROFIBUS master is the PC and the slaves are the inverters and the transmission speed is 12Mb/s. The data is always exchanged cyclically on the bus between the DP master and slaves by the telegram. Each telegram starts and ends with the PROFIBUS protocol frame and the useful data are stored in the PPO (Process Data Object) in the middle. The PPO consists of two parts, parameter (PKW) and process data (PZD), as shown in Figure 3-8. [89]

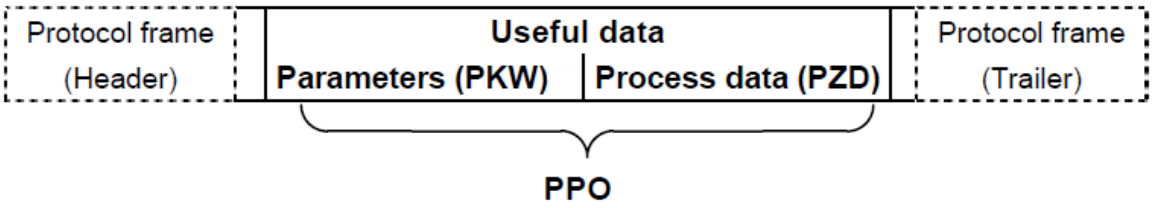

Figure 3-8 PROFIBUS telegram structure[89]

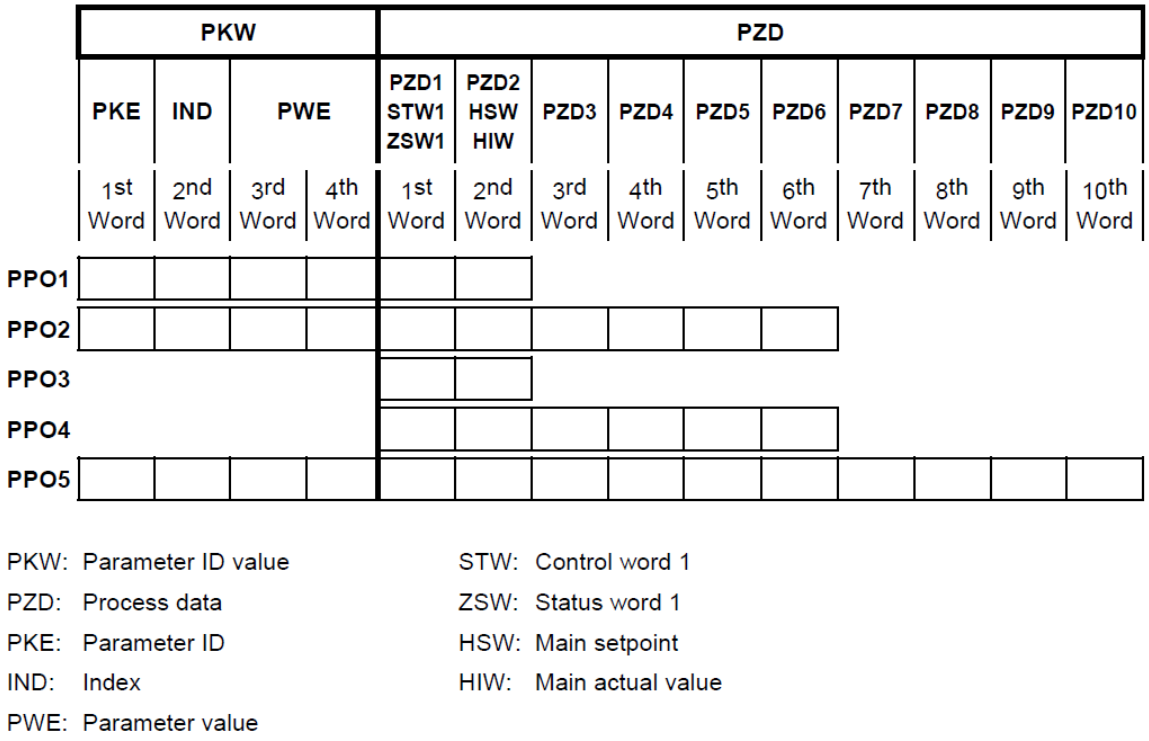

Figure 3-9 structure of the telegram

There are two types of telegrams, the 'call telegram' which is sent from the DP master to the DP slaves and the 'reply telegram' which is sent from the DP slaves to the DP master. In the 'call telegram', the control words and command value are include in the PZD part and other parameters to be written in the inverter comprise the PKW part. In the 'reply telegram', the status information and actual values of different parameters are sent back to the DP master in the PZD part; while some other parameter values are sent back in the PKW part. The inverter used for this roller rig provides 5 different PPO types, with different lengths of the PKW and the PZD parts, as shown in Figure 3-9. PPO5 with 10 PZD words are selected in this application. The first PZD word is the control/status word with 16 binary digits (4 digit in hexadecimal form), which is corresponding to 16 switches or inverter statuses. Details of the control/status word can be found in [89].

Object Linking and Embedding (OLE) for Process Control (OPC) specifies the standard in process control which allows different control devices and software to communicate between each other. OPC was first developed in 1996 and has become a set of standards after 2006. For the roller rig application, one of the standards, OPC DA (data access), is

used to provide a bridge between the inverter telegram and the data-processing softwares. OPC DA uses server-client scheme, in which the server provides the data and the client processes the data, as shown in Figure 3-10. Two different interfaces, automation interface and custom interface are available in this standard. The custom interface is a COM (Component Object Model) interface. The COM interface enables interprocess communication and dynamic object creation in programming languages such as Microsoft Visual C/C++. For other languages such as Microsoft Visual Basic and Delphi, access from the automation interface is defined by the OPC automation wrapper. Therefore, using the control commands and feedback parameters in the inverter telegrams can be automatically processed with other software.

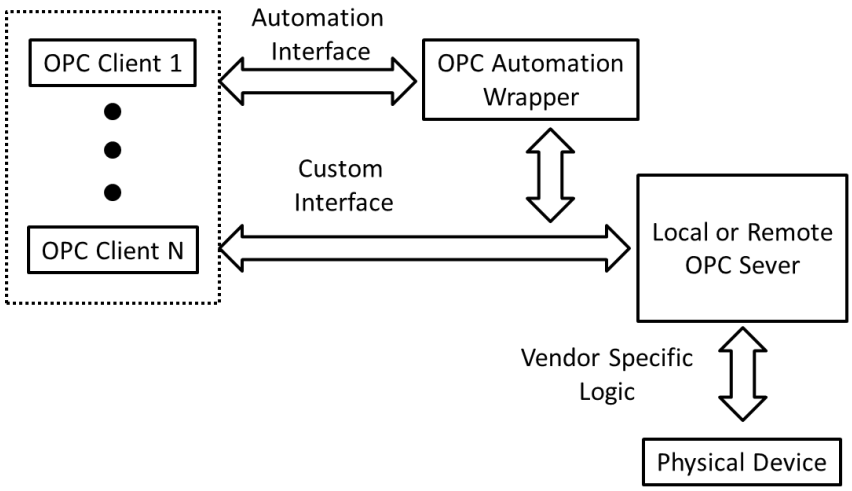

Figure 3-10 Typical OPC DA scheme

3.4. Sensors and data acquisition devices

Besides the data measured within the inverter drive (motor current, voltage and speed), the output current of the DC generator, the rotating speed of the wheel axle and roller axle are also required.

Incremental rotary encoders are used to measure the rotating speed of the wheel and roller axle and are mounted as shown in Figure 3-11. The encoder provides 1024 pulses per revolution, which makes the minimum resolution about 0.006 rad ($2\pi/1024$). As the encoder is required to be connected to a stationary part, a steel plate which is bolted on the wheelset frame is designed as the encoder holder. The thickness of the encoder holder is selected as 6mm to prevent relative movement against the wheelset frame, which leads to a long distance between the encoder holder to the end of the wheel axle and roller axle. Therefore, the hollow shaft version of the encoder is chosen here to overcome this disadvantage. An 8mm diameter encoder shaft is used to pass the rotation of the axle to the encoder. To eliminate the relative rotation between the

encoder shaft and the axles, the encoder shaft has a transient fit on the encoder side and tightened with grub screws. An interference fit is provided on the end of the axle.

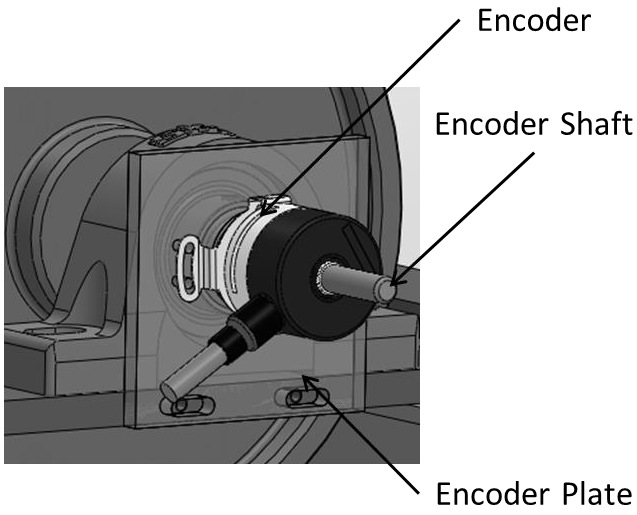

Figure 3-11 Encoder mounting

It is not very convenient to measure the driving torque of the DC generator directly, as the torque sensor requires a relatively large space and is expensive. Therefore, the output current of the DC generator is measured to calculate the torque indirectly. There are normally two ways to measure the current, one is connect a shunt resistor in the circuit and measure the voltage and then calculate the current indirectly. The other way is using electromagnetic based sensors, such as the Hall-effect sensor. For this roller rig, as the output voltage of the DC generator can be higher than 5V, which exceeds the maximum input of the data acquisition card. It is not an option to increase the load resistance to reduce the voltage as the resistance directly influences the load torque. Therefore, a hall-effect clamp is used to measure the output current of the DC generator. The measuring range of the current clamp is from 30mA to 30A for direct current. The accuracy is 1% of reading ±2mA at 25 °C. The output sensitivity is 100mV/A.

A data acquisition card is used to convert the analogue voltage signals from the sensors to digital signals and send them into the computer. Laboratory Virtual Instrumentation Engineering Workbench (LabVIEW) is used to analyse the collected sensor measurements and send control command to the inverter drives.

The data acquisition card is a National Instrument PCI-6010 data acquisition card provides 16 analogue input channels, 2 digital analogue input channels, two 32 bits, 100MHz digital counters and 10 digital input/output channels.

Normally the digital counters are used to count the pulses of the encoder output signals. However, in this application, the counters signals are highly interfered by the high frequency noise from the motor drives thus cannot offer reliable readings, which are most possibly led by the screening defects of the AC motors and the inverters. To solve

this problem, the encoder outputs are fed into the analogue input ports instead and a LabVIEW function is programmed to decode the encoder output, hence count the pulses and calculated the rotating speed instead of using the counters in the data acquisition card.

The encoder has 6 output channels, which are A, B, Z and $\overline{A}$, $\overline{B}$, $\overline{Z}$. An example of the signals of channels A and B are shown in Figure 3-12. Signals from channel A and channel B have a 90 degree phase shift. When the encoder turns forward, channel A leads channel B; otherwise channel B leads channel A.

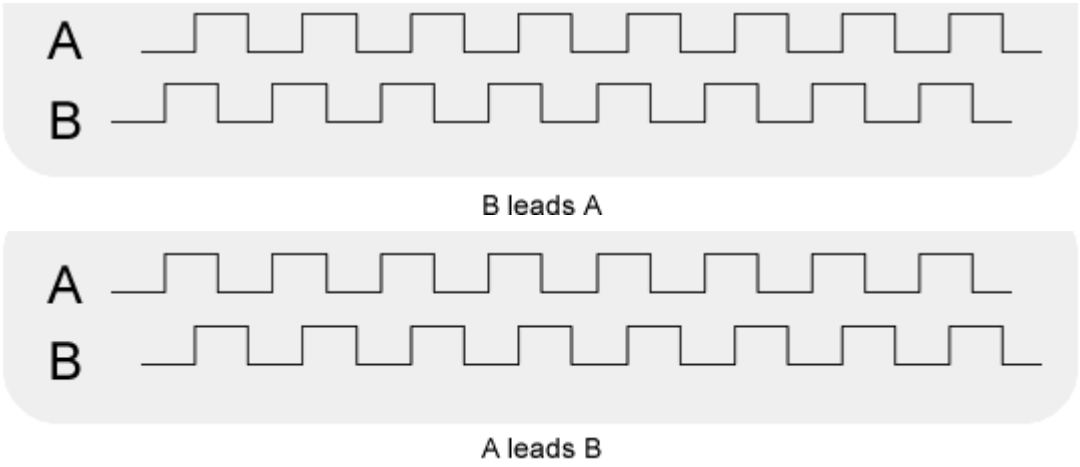

Figure 3-12 Example of the encoder output

The decoding algorithm uses the signals from channel A and channel B to determine the angular position of the encoder. The flow chart of the algorithm is shown in Figure 3-13. The A and B channels are scanned every cycle to determine the rotating direction of the encoder (DIR=Reverse or Forward) and updates the counts.

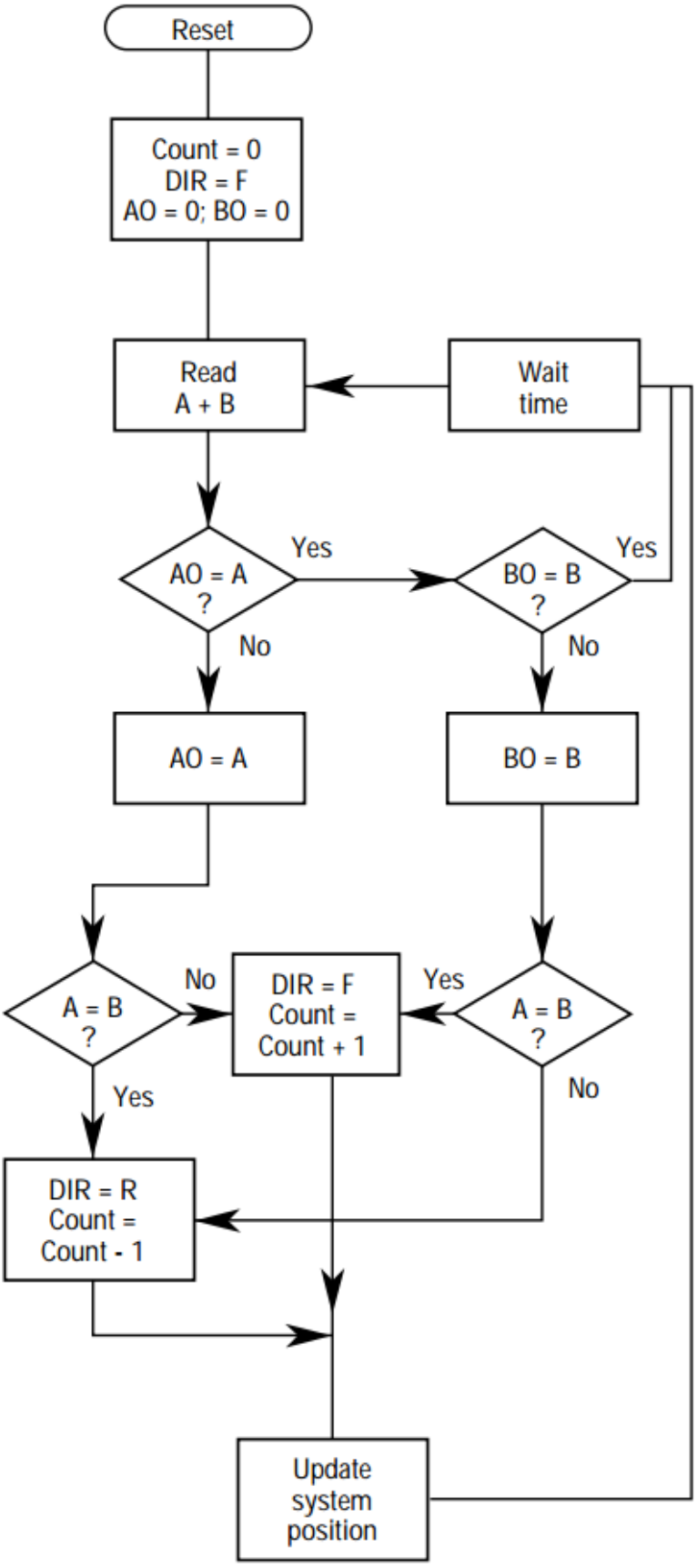

Figure 3-13 Decoding algorithm

The position θ and speed ω of the encoder can then be worked out according to the counts with the following equations:

$$\theta = \frac{2\pi Count}{1024} \tag{3-2}$$

$$\omega = \frac{d\theta}{dt} \tag{3-3}$$

The stator current, voltage components in the α–β frame and the motor speed signals are written in the inverter telegraph, as introduced in Section 3.3. The LabVIEW code has two parts: the data acquisition part which read the data from the inverter and the rotary encoders; the motor control parts which writes the control commands into the inverter.

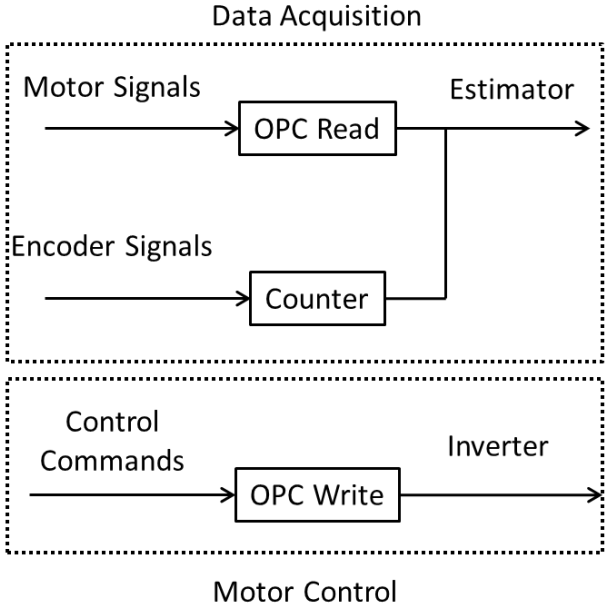

Figure 3-14 Layout of the LabVIEW code

3.5. AC motor parameters identification

Parameters such as stator and rotor resistances, stator, rotor and mutual inductances of the AC motors which are used on the roller rig are measured to provide knowledge required by this research project. Conventional methods such as no-load test and blocked-rotor test are used. In these conventional methods, the 3 phases of the motor are assumed to be balanced; hence only 1 phase is considered.

The single phase equivalent circuit of an induction motor is shown in Figure 2-5. The stator resistance (R_r) can be directly measured using a multimeter, and the blocked-rotor test and no-load test are used to identify the rotor resistance (R_s), stator, rotor and mutual inductances (L_{rr}, L_{ss} and L_m).

In the blocked-rotor test, the slip is unity, which results in $(1-s)R_r/s=0$. As the current in the rotor branch is much larger than that in the excitation branch, the excitation branch can be ignored and the equivalent circuit for the blocked rotor test is shown in Figure 3-15.

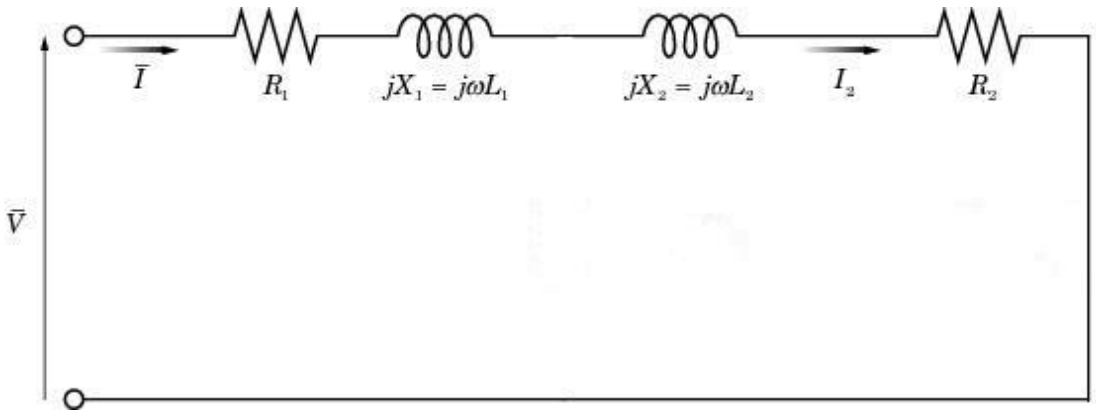

Figure 3-15 Equivalent circuit for the blocked-rotor test of the AC motor

The two watt-meter method is used to measure the voltage (V), current (I) and power (P) between the phase AB and phase AC. For each phase, the equations to identify the rotor resistance and the total reactance X are:

$$R_r = \frac{P}{I^2} - R_s \tag{3-4}$$

$$X = \omega(L_{ss} + L_{rr}) = \sqrt{(\frac{V}{I})^2 - (\frac{P}{I^2})^2} \tag{3-5}$$

The stator and rotor reactance are divided based on the empirical equations as summarized in Table 3-3. Both motors are both of Class D so the stator and rotor reactance are split equally.

Table 3-3 Blocked rotor reactance distribution [90]

Motor Type	L_{ss}	L_{rr}
Wound Rotor	50%	50%
Class A	40%	60%
Class B	40%	60%
Class C	30%	70%
Class D	50%	50%

The readings from the two watt-meter of both of the motors are In the no-load test, as the motor runs without load and the slip is very low; therefore the resistance in the rotor branch is very high. The rotor branch of the equivalent circuit can be neglected, which leads to the equivalent circuit for the no-load test as shown in Figure 3-16.

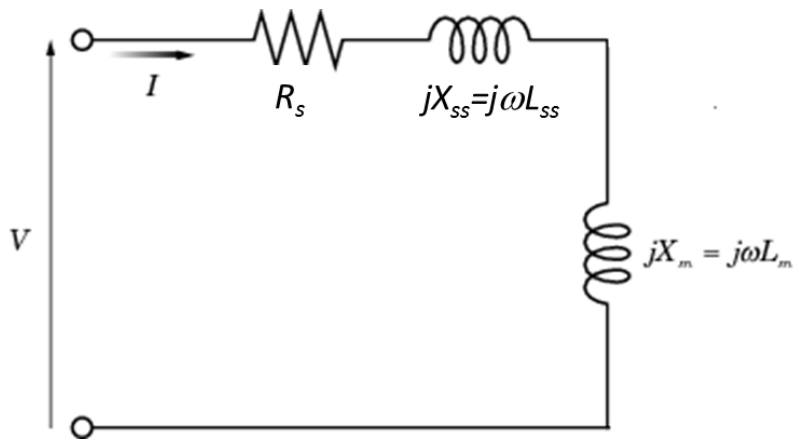

Figure 3-16 Equivalent circuit for the no-load test of the AC motor

The mutual reactance is calculated as:

$$X_m = \omega_e L_m = \frac{\sqrt{V^2 I^2 - P^2}}{I^2} - \omega_e L_{ss} \tag{3-6}$$

The readings for both motors are listed in Appendix D.

The parameters of both motors can be determined as:

Table 3-4 Motor parameters

	$R_1(\Omega)$	$R_2(\Omega)$	L_1(H)	L_2(H)	L_m(H)
Motor A	12.00	8.62	0.165	0.165	1.744
Motor B	12.00	9.24	0.169	0.169	1.852

3.6. Traction Load Calculation

As discussed previously, two DC motors are used as DC generators to provide traction load to the roller rig. An external resistor is connected to the output of the DC generator to vary the torque induced in the DC generator.

The equivalent circuit of the DC generator is shown in Figure 3-17, where the R_a is the armature resistance and the R_L is the load resistance. E_a is the back emf (electromotive force) generated in the armature. ω_{dc} is the rotating speed of the DC generator.

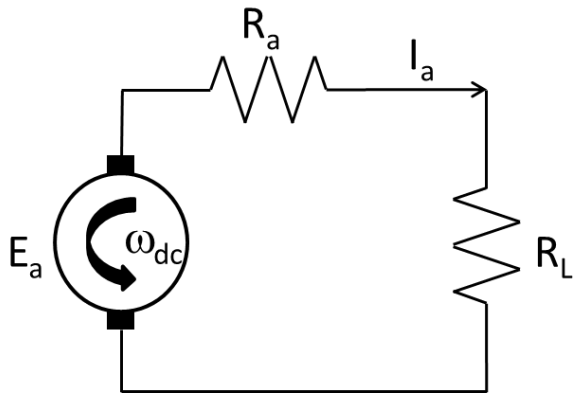

Figure 3-17 Equivalent circuit of the Permanent Magnet DC Generator

The following equations are used to model the DC generator:

$$E_a = k_\phi \omega_{dc} \tag{3-7}$$

$$I_a = \frac{E_a}{R_a + R_L} \tag{3-8}$$

$$T_{dc} = k_\phi I_a = k_\phi \frac{E_a}{R_a + R_L} = \frac{k_\phi^2}{R_a + R_L} \omega_{dc} \tag{3-9}$$

where k_ϕ is the magnetic constant of the DC generator.

For this DC generator, k_ϕ=0.096 and R_a=0.66Ω, thus the generated torque is:

$$T_{dc} = \frac{k_\phi^2}{R_a + R_L} \omega_{dc} = \frac{92.16 \times 10^{-4}}{0.66 + R_L} \omega_{dc} \tag{3-10}$$

According to Table 3-2, $\omega_{dc}=2.94\omega_{motor}$; then

$$T_{dc} = \frac{270.95 \times 10^{-4}}{0.66 + R_L} \omega_{motor} \tag{3-11}$$

The load torque applied on the roller axle is:

$$T_{Load} = 17.64 T_{dc} = \frac{47.8 \times 10^{-2}}{0.66 + R_L} \omega_{motor} \tag{3-12}$$

where $17.64=(84/20)^2$ is the transmission ration through the tooth belt pulleys from the roller to the DC generator.

The corresponding longitudinal creep force is:

$$F_{\gamma} = \frac{T_{Load}}{R_{roller}} = \frac{2.39}{0.66 + R_L}\omega_{motor} \quad (3\text{-}13)$$

3.7. Conclusion

In this chapter, the designed roller rig and its traction system is discussed. The roller rig is 1/5 scaled, with a unity time factor. The wheel diameter is 200mm and the roller diameter is 400mm. The wheel profile is scaled UK P8 and the roller profile is scaled BS 113a. To introduce a more direct and practical link between the traction motor and the bogie, two AC induction motors are mounted on the two wheelsets. Pairs of spur gears are used to transmit the movements from the traction motors to the wheelsets. Two DC generators are connected to the roller axles with timing belts to provide traction loads.

The traction motors are controlled by two inverters independently. Profibus (Process Field Bus) is used to connect the inverter to the computer and the control commands are given using the OPC (Object Linking and Embedding (OLE) for Process Control) protocol.

The stator voltage, current and speed signals are measured within the inverter; the rotating speed of the wheels and rollers are measured using incremental encoders. The output current signals of the DC generators are measured using hall-effect current clamps.

A program has been written using LabVIEW to collect the measured data from the inverter and the sensors. Control commands are also sent to the inverter using this code. With these features of the roller rig, experiment can be used to study the driving behaviour of railway vehicles and carry out to validate the proposed friction estimation methods.

4. Torsional model based estimator design

In this chapter, estimators are designed to monitor the wheel-roller friction coefficient based on the dynamic model of the roller rig. In the dynamic model only considers a single wheelset traction system which includes a traction motor, a wheelset and a pair of rollers. The rotational movements about the axles of the motor, wheelset and rollers are the only degrees of freedom considered in the dynamic model, so the interaction between the two wheelsets can be ignored. Then three estimation methods were investigated for estimating the creepage, creep force and friction coefficient at the wheel-roller interface. The first one uses a Kalman filter to estimate the electric torque of the traction motor and then estimates the creepage and creep force based on the estimated electric torque. It further couples with a root mean square algorithm to estimate friction coefficients at the wheel-roller interface. To improve the estimation accuracy of the first method, the extended Kalman filter is then used in the second method. When load is applied to the estimated system, the extended Kalman filter is found not able to offer accurate and stable performance therefore unscented Kalman filter is used in the third method.

4.1. Layout of the roller rig model

The layout of one wheelset of the roller rig is shown in Figure 4-1,.

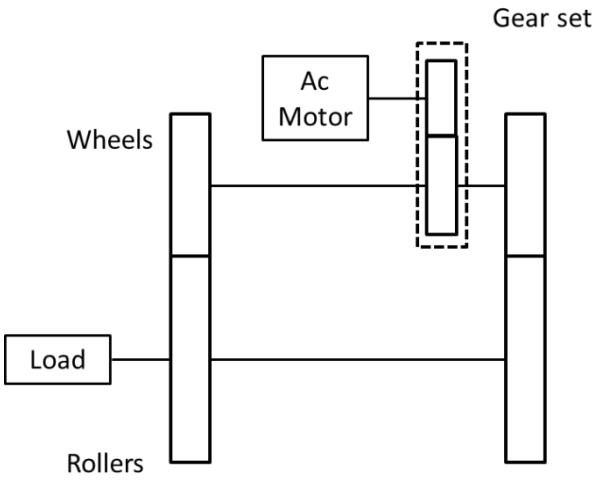

Figure 4-1 The layout of the simulated system

4.2. Dynamic model of the system

Equation (4-1) to (4-3) are the equations of motions of the system represented in Figure 4-1:

$$\frac{d}{dt}\omega_{motor} = \frac{T_e - 2iR_{wheel}F_\gamma}{J_{eqv}} \tag{4-1}$$

$$\omega_{wheel} = \frac{\omega_{motor}}{i} \tag{4-2}$$

$$\frac{d}{dt}\omega_{roller} = \frac{2R_{roller}F_\gamma}{J_{roller}} \tag{4-3}$$

where $J_{eqv} = J_{motor} + \frac{J_{wheel}}{i^2}$

T_e is calculated using the traction motor model in a stationary α - β frame with the following equation.

$$T_e = \frac{n_p L_m}{L_r}(I_{\beta s}\psi_{\alpha r} - I_{\alpha s}\psi_{\beta r}) \tag{4-4}$$

Dynamic equations of the stator current and rotor flux components are list in Equation (4-5) to (4-8). The motor is controlled by an indirect flux oriented scheme [91], which is commonly used in railway traction and other applications as discussed previously.

$$\frac{d}{dt}I_{\alpha s} = -(\frac{R_s}{\sigma L_s} + \frac{1-\sigma}{\sigma t_r})I_{\alpha s} + \frac{L_m}{\sigma L_s L_r t_r}\psi_{\alpha r} + \frac{L_m}{\sigma L_s L_r}\omega_r\psi_{\beta r} + \frac{1}{\sigma L_s}U_{\alpha s} \tag{4-5}$$

$$\frac{d}{dt}I_{\beta s} = -(\frac{R_s}{\sigma L_s} + \frac{1-\sigma}{\sigma t_r})I_{\beta s} - \frac{L_m}{\sigma L_s L_r}\omega_r\psi_{\alpha r} + \frac{L_m}{\sigma L_s L_r t_r}\psi_{\beta r} + \frac{1}{\sigma L_s}U_{\beta s} \tag{4-6}$$

$$\frac{d}{dt}\psi_{\alpha r} = \frac{L_m}{t_r}I_{\alpha s} - \frac{1}{t_r}\psi_{\alpha r} - \omega_r\psi_{\beta r} \tag{4-7}$$

$$\frac{d}{dt}\psi_{\beta r} = \frac{L_m}{t_r}I_{\beta s} + \omega_r\psi_{\alpha r} - \frac{1}{t_r}\psi_{\beta r} \tag{4-8}$$

where $\sigma = 1 - \frac{L_m^2}{L_s L_r}$ and $t_r = \frac{L_r}{R_r}$

As the lateral dynamics of the system is not considered in this research, the creepage and creep force terms contain the longitudinal components only. The creepage is calculated by the following equation:

$$\gamma = 2\frac{R_{roller}\omega_{roller} - R_{wheel}\omega_{wheel}}{R_{roller}\omega_{roller} + R_{wheel}\omega_{wheel}} \tag{4-9}$$

The creep force is acquired using Kalker's linear assumption and modified by the Vermeulen-Johnson equations [9]:

$$F_x = -f_{11}\gamma_x \tag{4-10}$$

$$F_\gamma = \begin{cases} \mu F_N \left(\frac{F_x}{\mu F_N} - \frac{1}{3}\left(\frac{F_x}{\mu F_N}\right)^2 + \frac{1}{27}\left(\frac{F_x}{\mu F_N}\right)^3\right) & F_x \le 3\mu F_N \\ \mu F_N & F_x > 3\mu F_N \end{cases} \quad (4\text{-}11)$$

The linear creep coefficient is defined as:

$$f_{11} = \mathrm{E}(a,b) C_{11} \quad (4\text{-}12)$$

where a and b are calculated by the Hertz method and C_{11}, C_{22} and C_{23} are calculated from approximate formulae given by Kalker [10].

4.3. Kalman filter based estimation

The Kalman filter based estimation model is a preliminary research to investigate the feasibility of estimation wheel-rail friction indirectly from traction motor signals. The system is set up as follow:

- Monitored system: AC motor
- System input: Stator voltage of the motor
- Measurement: Stator current of the motor
- Estimated variables: Stator flux of the motor

A simulation case is carried out based on the dynamic model from Section 4.2. Then the input and measurements are used in the Kalman filter to estimate the stator flux of the motor. The creepage and creep force values are further calculated using the dynamic equation of the roller rig. Finally, the friction coefficient is identified through curve fitting.

4.3.1. Simulation case and results

The parameters of the AC motor are given as:

The parameters of the system are given as: L_m=0.361H, L_s=0.362H, L_r=0.362H, R_s=3.2Ω, R_r=2.2Ω, R_{wheel}=0.1m, R_{roller}=0.2m, i=3, J_{wheel}=0.895Nm^2, J_{roller}=0.895Nm^2.

The induction motor is controlled by the Volts/Hz method and the details of this method can be found in Section 2.3.1. The frequency and voltage commands are given as:

$$f = \begin{cases} 4\mathrm{f}_0 t & t \le 0.25\mathrm{s} \\ \mathrm{f}_0 & t > 0.25\mathrm{s} \end{cases} \quad (4\text{-}13)$$

$$V_m = 30 + 5f \quad (4\text{-}14)$$

where f_0=50Hz.

It is assumed that the wheel and roller are held apart in the beginning and then get into contact at 1s, thus there is no creep force between the wheel and roller before 1s.

Simulation results of the rotating speed of the motor, wheel and roller are shown in Figure 4-2. The motor speed decreases slightly at 1s, when the wheel and roller start to interact with each other. The speed then increases slightly at about 2.6s, when the wheel and roller begin to rotate at a same speed. The change in the motor speed shows the change of load applied on it due to the effect of the creep force.

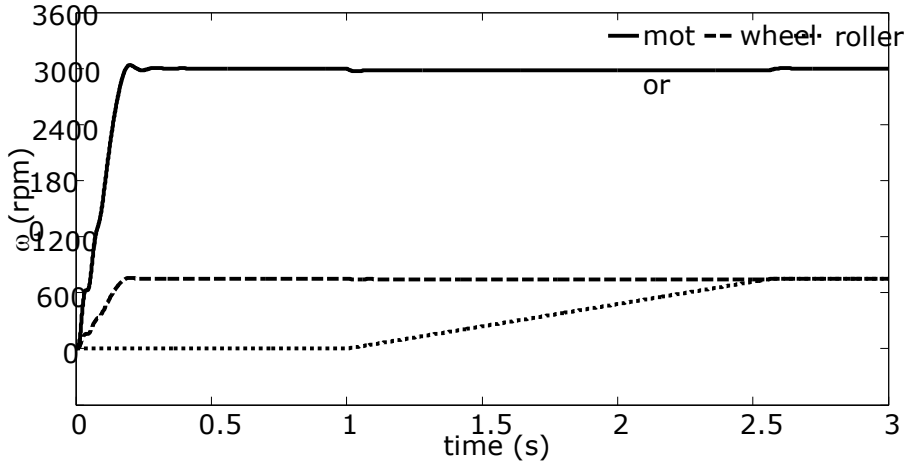

Figure 4-2 Speed results of the motor, wheel and roller

4.3.2. Estimation results

To estimate the wheel-roller friction coefficient, the wheel-roller creep force and creepage are required. A recursive Kalman filter is designed to estimate the creep force and creepage between the wheel and roller, using the recorded stator voltage, current and motor speed of the simulation model. Stator current signals $I_{\alpha s}$, $I_{\beta s}$ and rotor flux signals $\psi_{\alpha r}$, $\psi_{\beta r}$ are the state variables.

The system equation is worked out according to the model described above and is shown in (4-15),

$$x_{k+1} = Ax_k + Bu_k + w_k \tag{4-15}$$

where $x_k = \begin{bmatrix} I_{\alpha s} & I_{\beta s} & \psi_{\alpha r} & \psi_{\beta r} \end{bmatrix}^{\mathrm{T}}$

$u_k = \begin{bmatrix} U_{\alpha s} & U_{\beta s} \end{bmatrix}^{\mathrm{T}}$

$$\mathrm{A} = \begin{bmatrix} 1-\left(\frac{\mathrm{R_s}}{\sigma \mathrm{L_s}}+\frac{1-\sigma}{\sigma \mathrm{t_r}}\right)\mathrm{t_s} & 0 & \frac{\mathrm{L_m}}{\sigma \mathrm{L_s L_r t_r}}\mathrm{t_s} & \frac{\mathrm{L_m}}{\sigma \mathrm{L_s L_r}}\omega_r \mathrm{t_s} \\ 0 & 1-\left(\frac{\mathrm{R_s}}{\sigma \mathrm{L_s}}+\frac{1-\sigma}{\sigma t_r}\right)\mathrm{t_s} & -\frac{\mathrm{L_m}}{\sigma \mathrm{L_s L_r}}\omega_r \mathrm{t_s} & \frac{\mathrm{L_m}}{\sigma \mathrm{L_s L_r t_r}}\mathrm{t_s} \\ \frac{\mathrm{L_m}}{\mathrm{t_r}}\mathrm{t_s} & 0 & 1-\frac{1}{\mathrm{t_r}}\mathrm{t_s} & -\omega_r \mathrm{t_s} \\ 0 & \frac{\mathrm{L_m}}{\mathrm{t_r}}\mathrm{t_s} & \omega_r \mathrm{t_s} & 1-\frac{1}{\mathrm{t_r}}\mathrm{t_s} \end{bmatrix}$$

$$\mathrm{B} = \begin{bmatrix} \frac{1}{\sigma \mathrm{L_s}} & 0 \\ 0 & \frac{1}{\sigma \mathrm{L_s}} \\ 0 & 0 \\ 0 & 0 \end{bmatrix}$$

where t_s = 0.1ms is the timestep, $\sigma=1-\frac{L_m^2}{L_s L_r}$ and $t_r=\frac{L_r}{R_r}$

The measurement matrix is shown in (4-16),

$$z_k = Hx_k + v_k \tag{4-16}$$

where $z_k = \begin{bmatrix} I_{\alpha s} & I_{\beta s} \end{bmatrix}^T$

$H = \begin{bmatrix} 1 & 0 & 0 & 0 \\ 0 & 1 & 0 & 0 \end{bmatrix}$

The covariance matrices for system and measurement noise Q and R are:

- **Q**=diag[1e-6,1e-6,1e-6,1e-6]
- **R**=diag[1e-4,1e-4]

By adopting the "predictor-corrector" algorithm of the Kalman filter, the rotor flux signals $\psi_{\alpha r}$, $\psi_{\beta r}$ are estimated. The electric torque, mechanical torque of the motor and the wheel-roller creep force and creepage are further estimated by equations (4-1) to (4-8) and hence the F_γ- γ relationship can be estimated.

A comparison of the estimated results and simulated results of the electric torque is shown in Figure 4-3. The estimation error is most significant when the motor is in its dynamic state, which is a nonlinear process. After the motor reaches its steady state, the estimation error reduces to a very small value proving the Kalman filter is working properly.

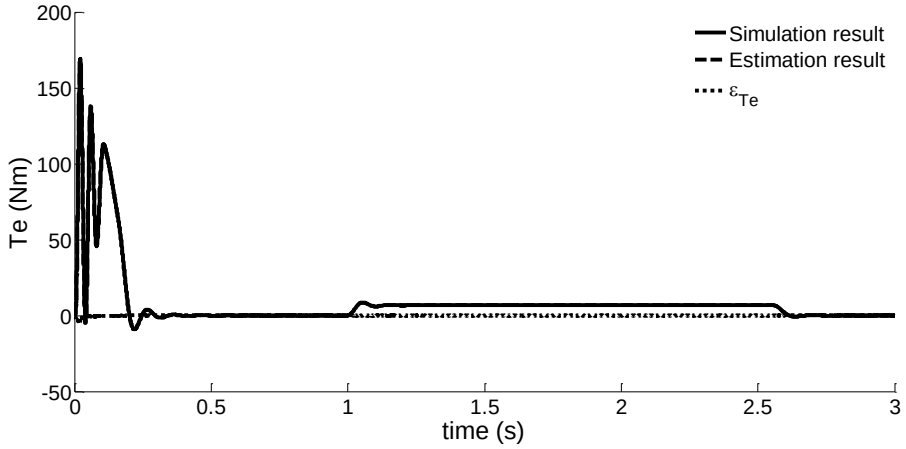

Figure 4-3 Result of the electric torque

From the estimated electric torque the estimated creep force-creepage curve is plotted and compared to the curve based on the simulation results, as shown in Figure 4-4.

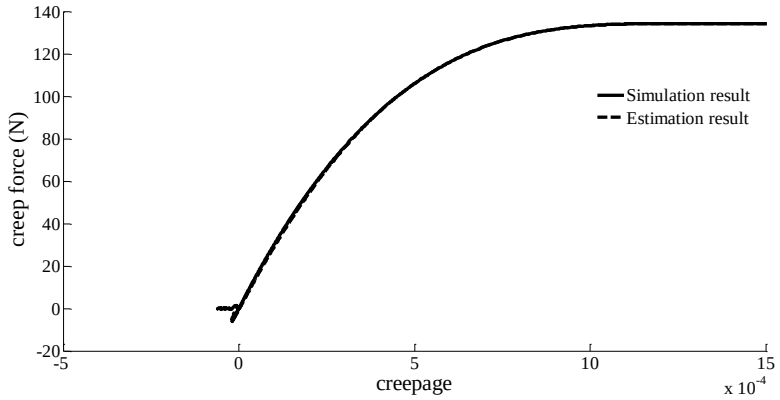

Figure 4-4 Creepage-creep force relationship

It can be seen that the estimation error for the electric torque is very small demonstrating that the estimated creep force and creepage are very accurate. The creepage-creep force result is then compared to series of simulation results to calculate the residual between them. In the last step, the friction coefficient is identified by curve fitting. It is shown that the best fit happens when the friction coefficient is 0.27,, which is the same as that in the simulation model.

As the studied system is non-linear, parameters such as the creep force, creepage and friction coefficient cannot be estimated directly from the Kalman filter but have to be calculated from the estimation result of the electric torque. This accumulates the estimation error of the electric torque and eventually affects the accuracy of the estimation of the friction coefficient.

4.4. Extended Kalman filter based estimation

The extended Kalman filter based estimation model is set up as follow:

- Monitored system: wheelset-roller system with an AC traction motor
- System input: stator voltage of the motor
- Measurement: stator current and speed of the motor
- Estimated variables: creepage, creep force, speed of the roller, traction and friction coefficient

Due to the limitation that the Kalman filter can only estimate linear systems, the potential of using the extended Kalman filter (EKF) to estimate parameters for a more complex railway vehicle traction system is studied. Polach's model is used to calculate the creep force as it can offer a more accurate result with large creepage. The friction coefficient is treated as a variable in this case. These models have been discussed in Section 2.2 and the equations used to calculate the creep force are as follow:

$$F_\gamma = \frac{2F_N\mu}{\pi}\left(\frac{k_A\varepsilon}{1+(k_A\varepsilon)^2} + \arctan(k_s\varepsilon)\right) \tag{4-17}$$

$$\varepsilon = \frac{G\pi abC_{11}}{4F_N\mu}\gamma \tag{4-18}$$

$$\mu = \mu_0((1-D)e^{-B\gamma(0.5(R_{roller}\omega_{roller}+R_{wheel}\omega_{wheel}))} + D) \tag{4-19}$$

4.4.1. Simulation case and results

The induction motor in this simulation case is controlled by the indirect field oriented method and the details of this method can be found in Section 2.3.2. The flux demand ψ_r^* is given as 5Wb and the speed demand ω_r^* changes by the following pattern:

$$\omega_{motor}^*(\text{rad/s}) = \begin{cases} 2\pi f & t < 0.5\text{s} \\ 3\pi f & 0.5\text{s} \le t < 1.5\text{s} \\ 2\pi f & 1.5\text{s} \le t < 2.5\text{s} \\ 3\pi f & 2.5\text{s} \le t < 3.5\text{s} \\ 2\pi f & 3.5\text{s} \le t < 4.5\text{s} \\ 3\pi f & 4.5\text{s} \le t < 7\text{s} \\ 2\pi f & 7\text{s} \le t \le 7.5\text{s} \end{cases} \tag{4-20}$$

While the friction coefficients are set according to the following equation to simulate 3 different contact conditions between the wheel and roller, which are dry, wet and low. Details of these conditions are listed in Table 2-1. However, to help the system stabilize faster, a lower friction value was applied in the first 0.5s of the simulation.

$$\mu_0 = \begin{cases} 0.4 & t \le 0.5\text{s} \\ 0.55(\text{dry}) & 0.5\text{s} < t \le 2\text{s} \\ 0.3(\text{wet}) & 2\text{s} < t \le 4\text{s} \\ 0.06(\text{low}) & 4\text{s} < t \le 7.5\text{s} \end{cases} \tag{4-21}$$

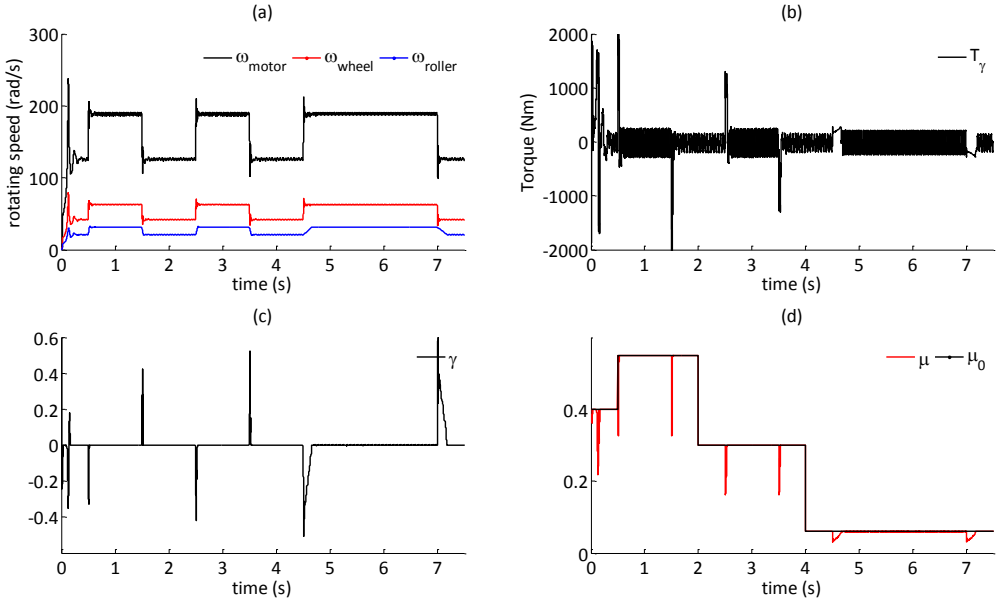

Figure 4-5 Simulation results for EKF

The speed, creep force torque, creepage and traction coefficient results are plotted in Figure 4-5 (a) to (d). In plot (a), the speed difference between the wheel and roller becomes greater when the friction coefficient drops. This speed difference (creepage) is also shown in plot (c), showing that both the magnitude and duration of the creepage increase under lower friction. This is because the maximum value of the mechanical torque of the motor (T_γ) is lower when the friction coefficient decreases, as presented in plot (b). Plot (d) shows that when creepage occurs, the traction coefficient decreases to a much lower value, which results in the more obvious slip between the wheel and roller. The results of this simulation model will be used to provide knowledge for the proposed estimation and then validate against the generated estimation results.

4.4.2. Estimation results

The state equation and measurement equation are given as:

$$\mathrm{x}_{k+1} = \mathbf{A}\mathrm{x}_k + \mathrm{w}_k \tag{4-22}$$

$$\mathrm{z}_k = \mathbf{H}\mathrm{x}_k + \mathrm{v}_k \tag{4-23}$$

where:

$$\mathrm{x} = \left[I_{\alpha s}, I_{\beta s}, \psi_{\alpha r}, \psi_{\beta r}, \omega_{motor}, U_{\alpha s}, U_{\beta s}, \gamma, F_\gamma, \omega_{roller}, \mu, \mu_0 \right]^T \tag{4-24}$$

$$\mathrm{z} = \left[I_{\alpha s}, I_{\beta s}, \omega_{motor}, U_{\alpha s}, U_{\beta s} \right]^T \tag{4-25}$$

State matrix **A** and Measurement matrix **H** are determined by system dynamic equations as listed in Section 4.2. The value of matrices **Q** and **R** can have a very large influence on the EKF performance. In this simulation, both of these matrices are assumed to be

diagonal to reduce computing time and both matrices can be obtained by considering the stochastic properties of the corresponding noise [92]. Due to the uncertainty of the system and measurement noise, **Q** and **R** are usually determined by a trial-and-error process.

For this simulation, covariance matrices **Q** and **R** are set as:

- **Q**=diag[1e-6,1e-6,1e-6,1e-6,1e-6,1e-6,1e-6,1e-2,1e-2,1e-2,1e-2,1e-2]
- **R**=diag[1e-6,1e-6,1e-6,1e-6,1e-6]

State variables $\psi_{\alpha r}$, $\psi_{\beta r}$, hence T_e are estimated from the EKF using Equation (4-4). The estimation result and error of the electric torque are shown in Figure 4-6. It can be seen that the error is generally small except when the speed command suddenly changes and this difference only lasts for a few time steps. All the following figures start at 0.5s as the system was not stable before then.

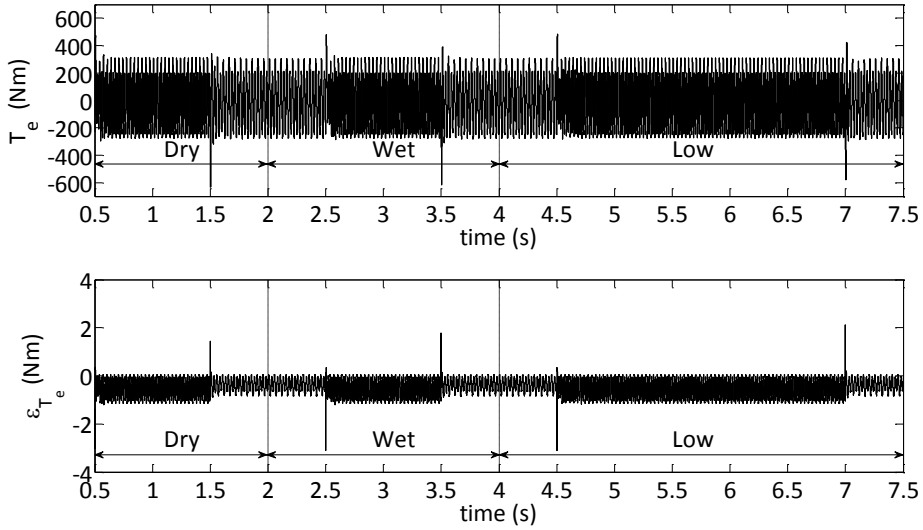

Figure 4-6 Estimation and error of the electric torque

The estimation results of γ and F_γ are shown in Figure 4-7 and Figure 4-8 only have remarkable error during the transition of the speed command.

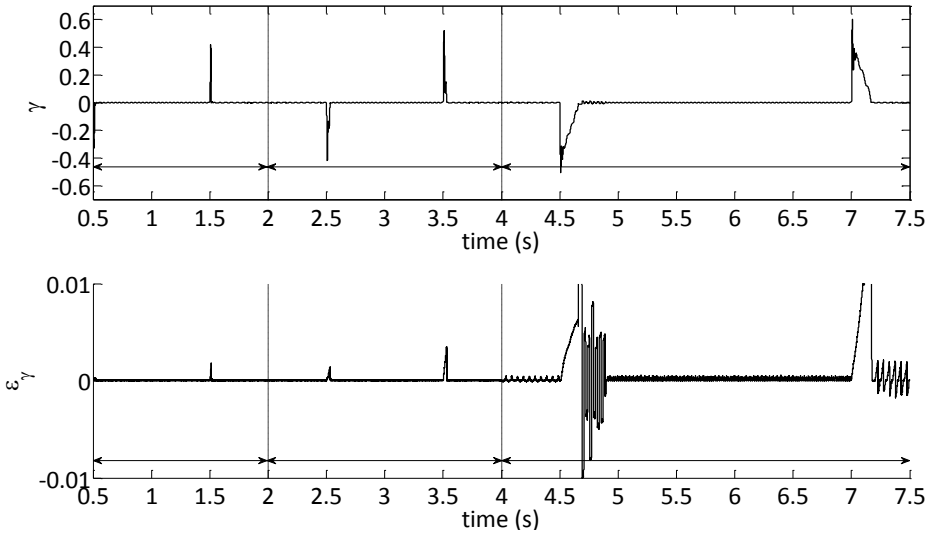

Figure 4-7 Estimation and error of the creepage

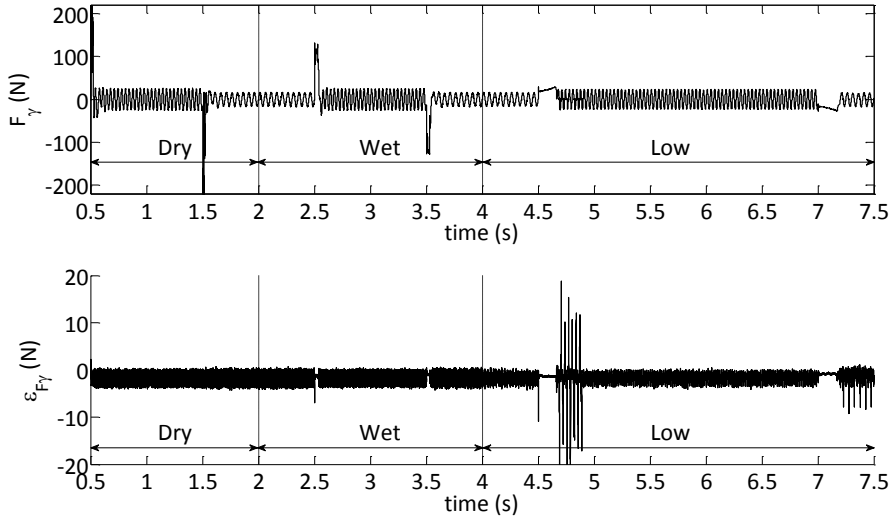

Figure 4-8 Estimation and error of the creep force

In Figure 4-9, the estimated friction coefficient does not respond to the change of the actual value immediately until a large creepage occurs. This is due to the fact that the value of the creep force, hence the roller speed and the creepage are not affected by the traction coefficient unless the creepage is large enough so that the friction coefficient can have a significant enough influence on the creep force. To solve this problem, it is necessary to apply a load on the roller to create the creepage. However, the estimation results in this case turn to be very time consuming and unstable, which may be caused by the high non-linearity of the system. To solve these problems, the performance of the unscented Kalman filter is then evaluated in the next section.

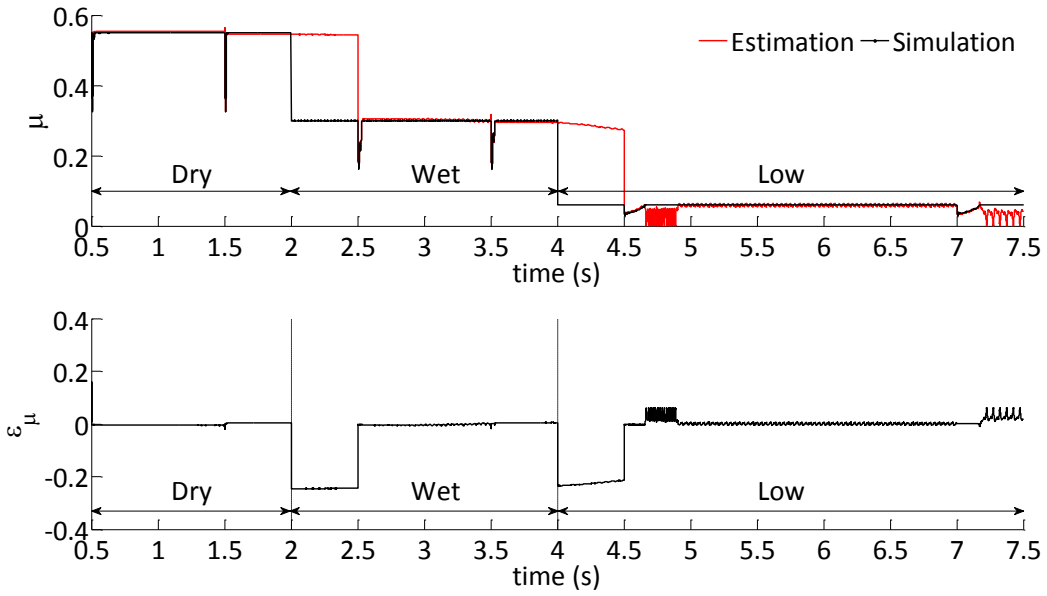

Figure 4-9 Actual result and estimation of the traction coefficient

4.5. Unscented Kalman filter based estimation

The unscented Kalman filter based estimation model is set up as follow:

- Monitored system: wheelset-roller system with an AC traction motor
- System input: stator voltage of the motor
- Measurement: 3 cases, see following discussion
- Estimated variables: 3 cases, see following discussion

4.5.1. Simulation case and results

A similar simulation case to the one in Section 4.4 is used for this simulation. The only difference is that there is an external load T_{Load} applied on the roller axle. The load applied to the roller axle simulates the wheelset running up a slope with 7% gradient before 3.7s and a slope with 2% gradient after 3.7s. Compared with the results shown in Figure 4-5, Figure 4-10(a) shows that the roller speed increases much more slowly due to the external load. The effect of the traction load can be seen more clearly in the creepage result, as plotted in Figure 4-10 (c). These simulation results are used in the unscented Kalman filter (UKF) developed in the following sections.

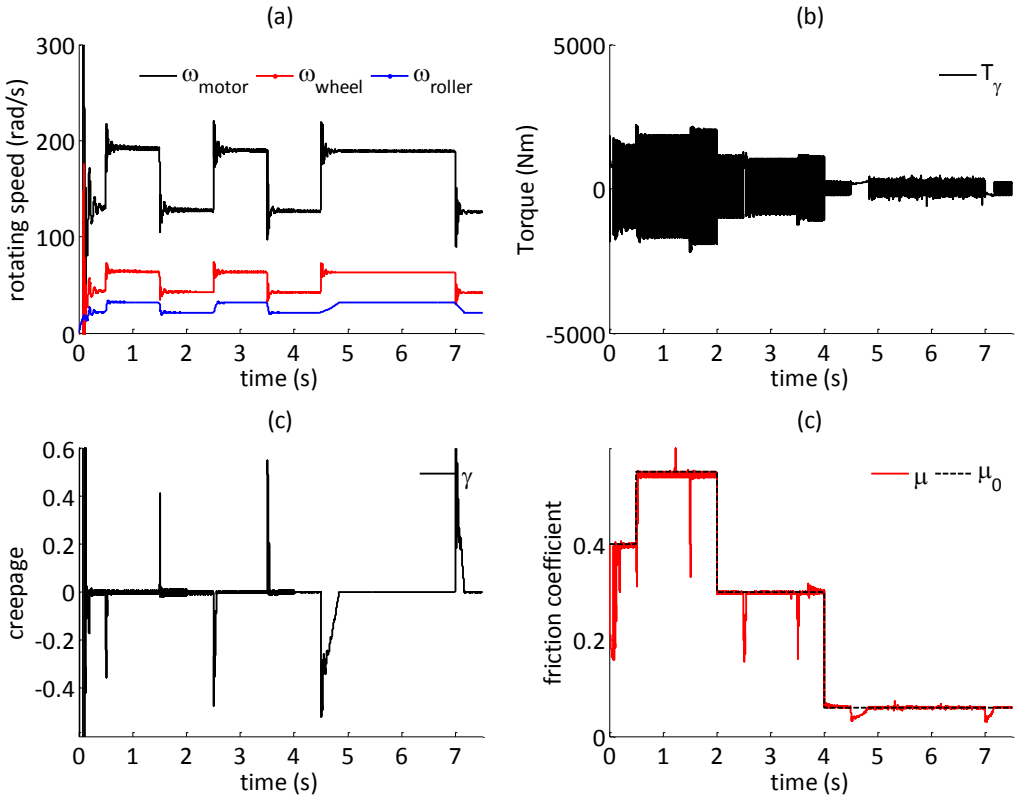

Figure 4-10 Simulation results for UKF

4.5.2. Estimation results

The state variables are:

$$x = \left[I_{\alpha s}, I_{\beta s}, \psi_{\alpha r}, \psi_{\beta r}, \omega_{motor}, U_{\alpha s}, U_{\beta s}, \gamma, F_{\gamma}, \omega_{roller}, \mu, \mu_0, T_{Load} \right]^T \quad (4\text{-}26)$$

To study the necessity of the knowledge of ω_{roller} and T_{Load}, three different sets of measurements are used, which are:

$$z^{(1)} = \left[I_{\alpha s}, I_{\beta s}, \omega_{motor}, U_{\alpha s}, U_{\beta s}, \omega_{roller}, T_{Load} \right]^T \quad (4\text{-}27)$$

$$z^{(2)} = \left[I_{\alpha s}, I_{\beta s}, \omega_{motor}, U_{\alpha s}, U_{\beta s}, \omega_{roller} \right]^T \quad (4\text{-}28)$$

$$z^{(3)} = \left[I_{\alpha s}, I_{\beta s}, \omega_{motor}, U_{\alpha s}, U_{\beta s}, T_{Load} \right]^T \quad (4\text{-}29)$$

State matrix **A** and Measurement matrix **H** are determined by system dynamic equations as listed in Section 4.2. As the dynamic equations are nonlinear an extended Kalman filter is chosen to provide estimations of the state variable.

For this simulation, **Q** and **R** are set as:

- **Q**=diag[1e-6,1e-6,1e-6,1e-6,1e-6,1e-6,1e-6,1e-2,1e-2,1e-2,1e-2,1e-2,1e-6]
- $\mathbf{R}^{(1)}$=diag[1e-6,1e-6,1e-6,1e-6,1e-6,1e-6,1e-6]

- $\mathbf{R}^{(2)}= \mathbf{R}^{(3)}$=diag[1e-6,1e-6,1e-6,1e-6,1e-6,1e-6]

State variables $\psi_{\alpha r}$, $\psi_{\beta r}$, and hence T_e are estimated from the UKF using Equation (4-4). The estimation result and error of the electric torque are as follow. The estimation results and errors of T_e for case 1-3 are shown in Figure 4-11.

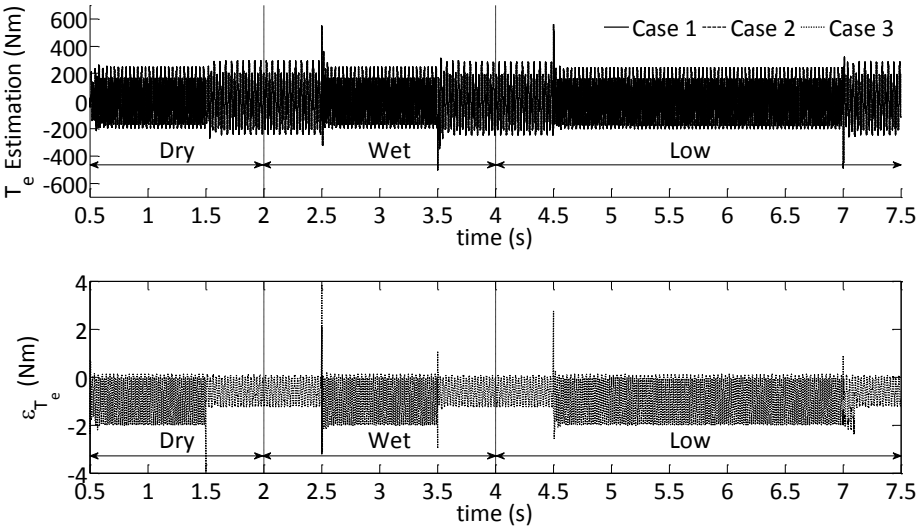

Figure 4-11 Estimation results and errors for the electric torque

In all of the 3 cases, the error is generally small despite when the speed command suddenly changes and will only last a few time steps and there is no significant difference between these cases.

The estimation results and errors of γ are shown in Figure 4-12. As in case 1 and case 2, both the wheel and roller speed are measured, the errors are very small. In case 3, before 4.5s, the error is about the same as that of case 1 and case 2; but the error becomes more significant after 4.5s.

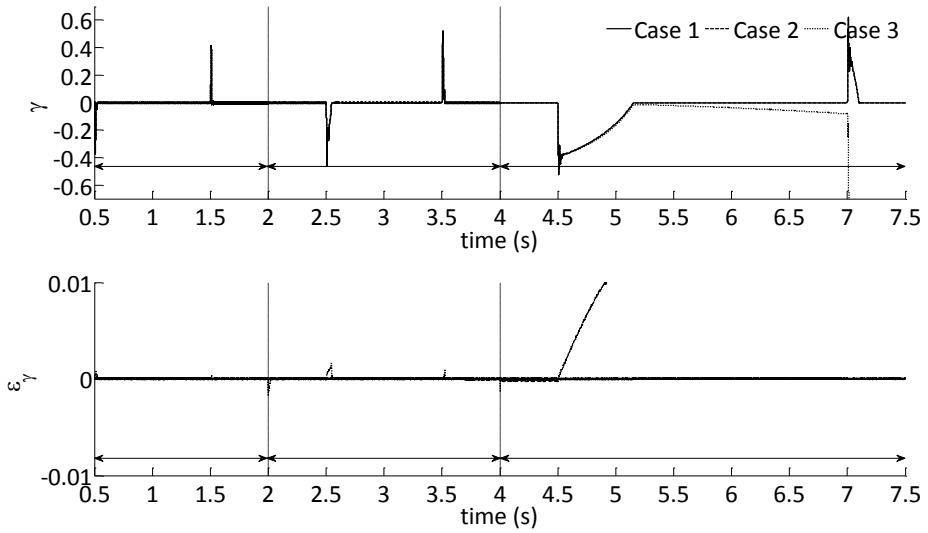

Figure 4-12 Estimation results and errors for the creepage

The same pattern can also be found in Figure 4-13, the estimation error for F_γ in case 3 rises to a much higher value between about 3.7s to 4.5s and after 5.2s while the errors for the other 2 cases still remain low.

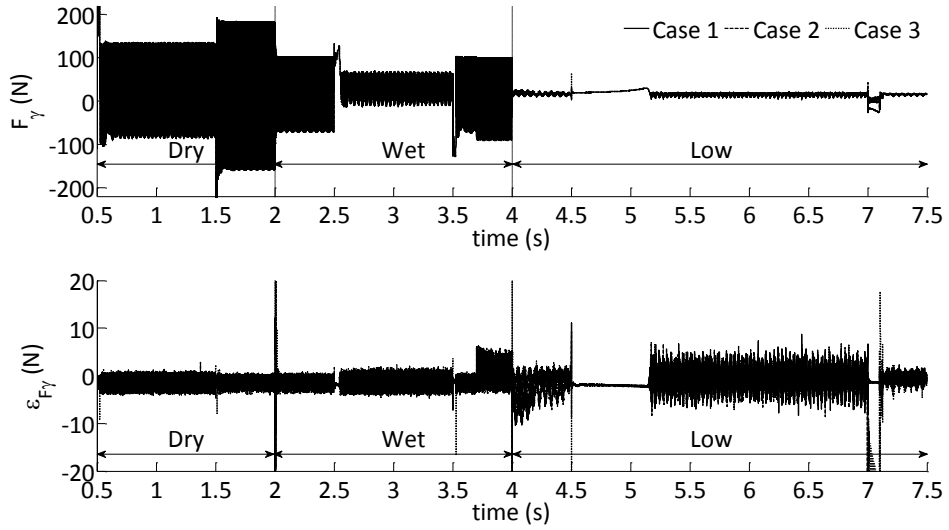

Figure 4-13 Estimation results and errors for the creep force

Figure 4-14 shows the estimation results for μ. For all of the 3 cases, the estimation results are accurate and respond in 0.02s (because the load is large enough) when μ drops from 0.55 to 0.3. However, when μ drops from 0.3 to 0.06, the estimation results have large lags: about 0.2s for case 1, 0.5s for case 2 and case 3 will not respond to the change until a large change of creepage occurs (i.e., change of speed command).

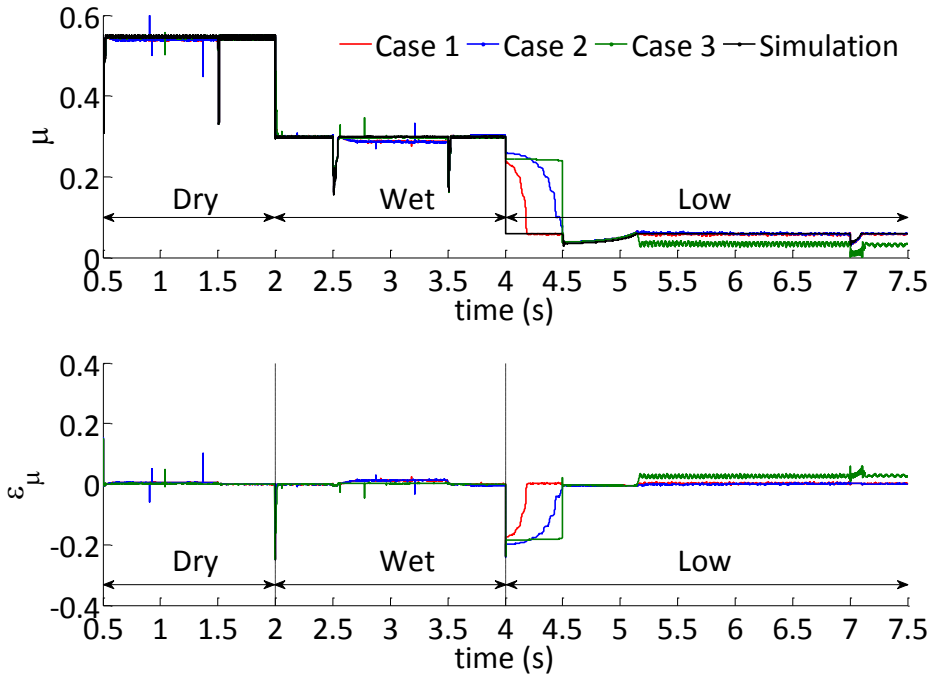

Figure 4-14 Estimation results and errors for the traction coefficient

These three combinations of measurements have shown that it is necessary to measure the roller speed for accurate estimation of the friction coefficient, while the impact of measuring traction load is not as obvious.

4.6. Re-adhesion control design

Large creepage will occur at the wheel-rail interface during the acceleration and braking of the vehicle, especially under low adhesion. The excessive creepage can lead to wear and fatigue at the wheel and rail profile. The traction coefficient also decreases under large creepage, which reduces the available creep force between the wheel and rail, and results in a longer accelerating and braking time.

A re-adhesion control scheme was designed based on the basic IFOC control strategy and the UKF friction estimator developed in Section 4.5. By applying this control scheme, the wheel-roller creepage can be maintained around the optimum point where the maximum creep force can be achieved. This controller can therefore utilize the maximum available adhesion and reduce the acceleration and braking time (distance) to their minimum value.

4.6.1. Controller design

The block diagram of the proposed control scheme is presented in Figure 4-15. It is a typical IFOC diagram with an additional re-adhesion controller which is included in the

dashed lines. The control commands are motor speed and rotor flux; and motor actual speed, current and voltage are the feedback signals.

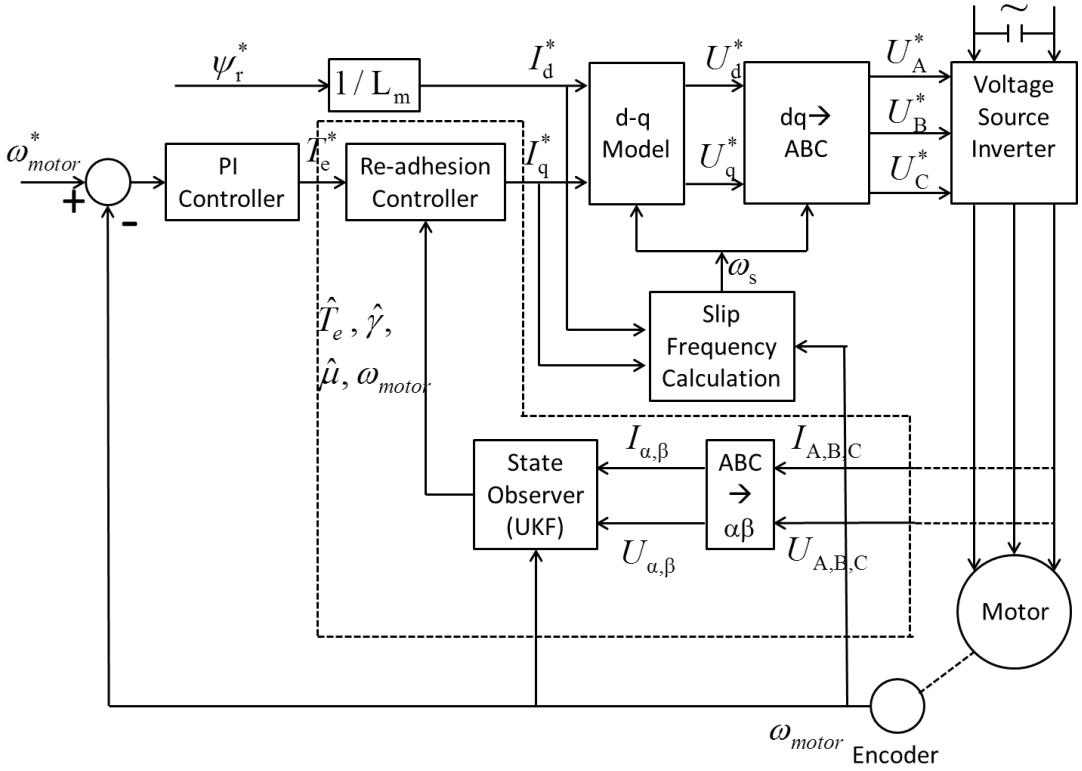

Figure 4-15. Block diagram for the control scheme of the traction motor

The aim of applying this re-adhesion controller is to keep the system working at the peak of the creepage – creep force curve as shown in Figure 2-4. To achieve this, first the stator voltage and current signals of the motor are transformed to the α – β frame from the ABC frame, providing the information required by the unscented Kalman filter block. Together with the voltage and current signals, motor speed is also fed into the UKF which estimates the creepage, creep force and traction coefficients. Finally the re-adhesion algorithm is applied thus compensate the electric torque command according to estimation results.

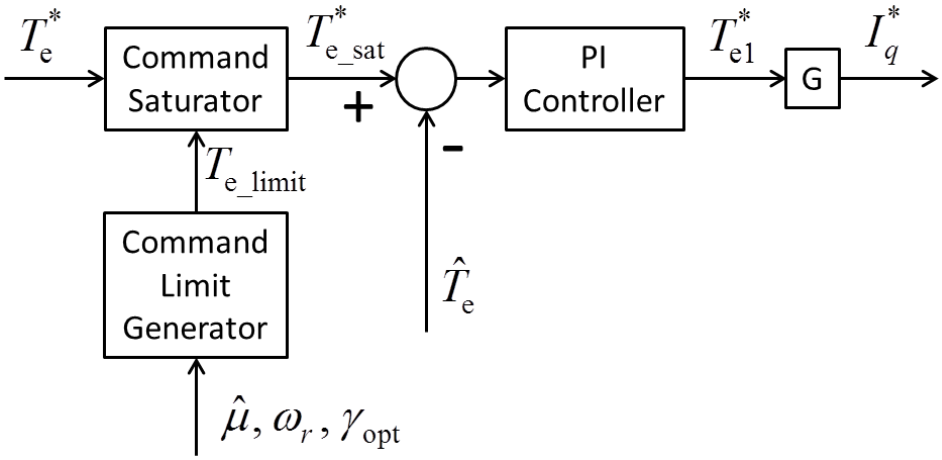

Figure 4-16 Re-adhesion controller structure

The re-adhesion algorithm is shown in Figure 4-16. In this algorithm, first the upper and lower limits of electric torque command are calculated according to the motor speed, the estimated traction coefficient and the optimized creepage (as discussed in) with equation (4-30) and (4-31). The optimal creepage (γ_{opt}) values for different friction coefficients are interpolated from Figure 2-4.

$$T_{e\_limit} = \frac{R_{wheel}}{i} F_{opt} + J_{eqv}\dot{\omega}_r \tag{4-30}$$

$$F_{opt} = \frac{2F_N\hat{\mu}}{\pi}\left(\frac{k_A \frac{G\pi abC_{11}}{4F_N\hat{\mu}}\gamma_{opt}}{1+(k_A \frac{G\pi abC_{11}}{4F_N\hat{\mu}}\gamma_{opt})^2} + \arctan(k_s \frac{G\pi abC_{11}}{4F_N\hat{\mu}}\gamma_{opt})\right) \tag{4-31}$$

To maintain the simplicity of the controller, the optimized creepage values for friction coefficients other than those listed in Table 2-1 are determined using linear interpolation. As the main purpose of the controller is to avoid excessive creepage between the wheel and roller, it is not necessary to keep the wheel-roller creepage at its exact optimal value.

The command saturator block works as a bandwidth controller, which regulates the value of T_e^* within its limitations (T_{e_limit}). Then the error between the regulated electric torque command and the estimated electric torque are fed into a PI regulator, to gain a smooth and stable performance.

4.6.2. Controller performance evaluation

Another simulation was carried out under the same conditions which are listed in Section 4.5 with the re-adhesion controller. The simulation results with and without the re-adhesion controller were then compared.

Figure 4-17 shows the wheel speed signals with and without the re-adhesion controller. When the re-adhesion controller was applied, the wheel speed changes were much slower and smoother. When the lower the friction coefficient decreases, the influence of

the controller on the wheel speed becomes more significant, as the available adhesion between the wheel and roller is reduced.

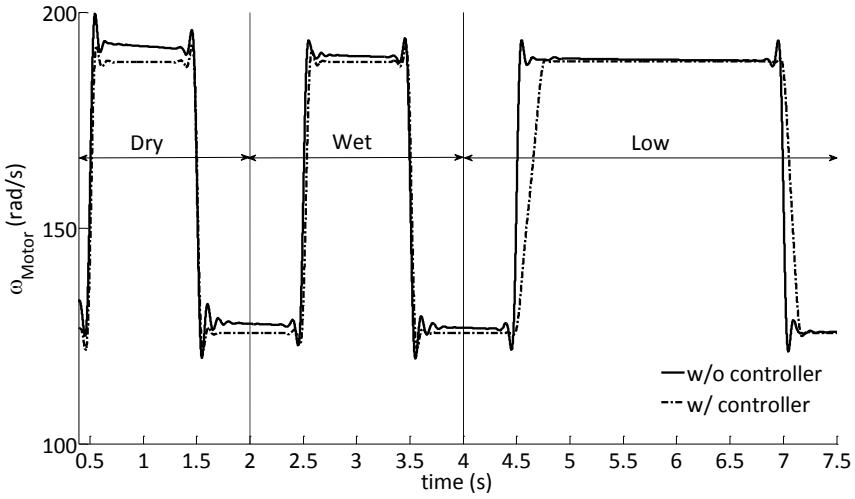

Figure 4-17 Wheel speed performance with and without controller

Though the wheel speed increases more slowly when the controller is applied, the roller speed increase faster as the controller regulates the creepage to its optimise value which can generate the maximum creep force, as shown in Figure 4-18.

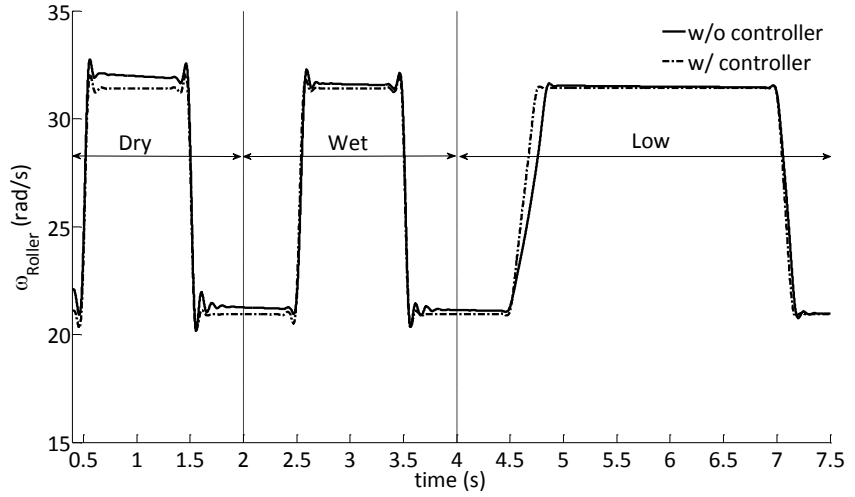

Figure 4-18 Roller speed performance with and without controller

The effect of the controller is very obvious in Figure 4-19, where the creepage value changes remarkably when the controller is applied. For the normal IFOC method, the creepage could reach up to 40%, while the optimised value is no larger than 5.5%. The excessive creepage would lead to a large drop in the traction coefficient, therefore reducing the available creep force.

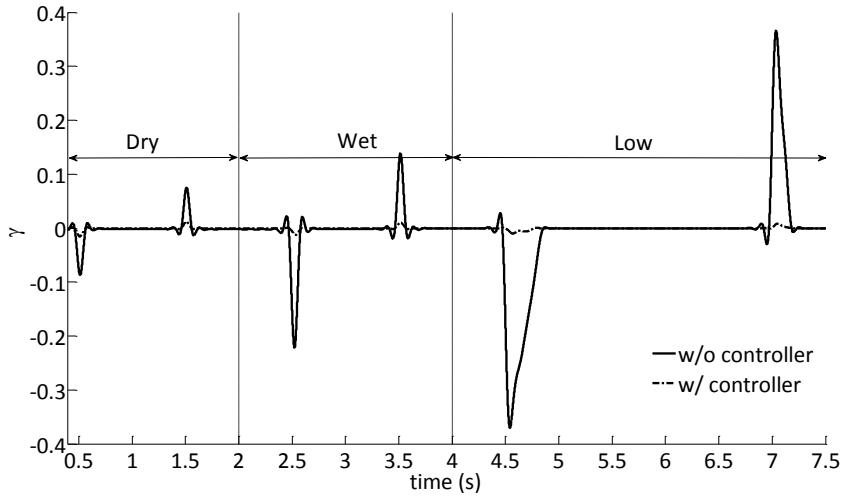

Figure 4-19 Creepage performance with and without controller

The utilization rate of the available creep force can also increase with the use of controller, which explains why the roller speed increases faster when the controller is used, as presented in Figure 4-20. It is very obvious that when the friction low, the creep force signal has a shorter duration but higher amplitude with the re-adhesion controller.

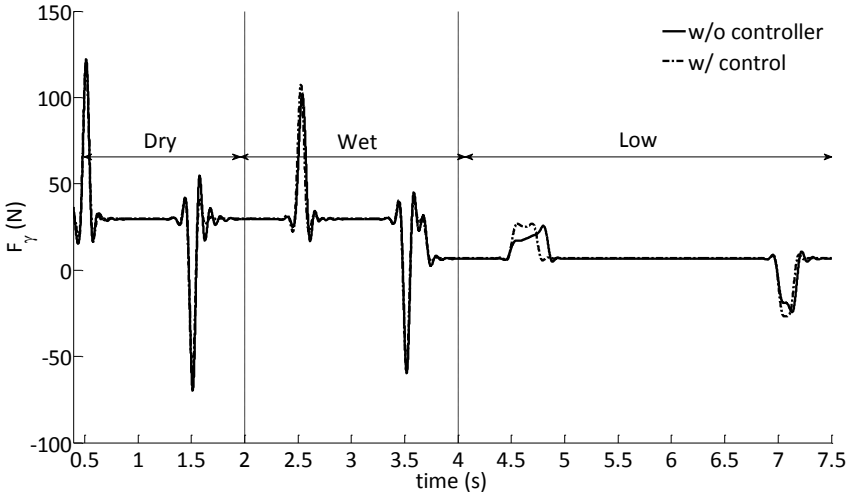

Figure 4-20 Creep force performance with and without controller

Figure 4-21 shows how much the creep force decreases with large creepage without the re-adhesion controller, while the creep force stays at a much larger value when the controller is engaged.

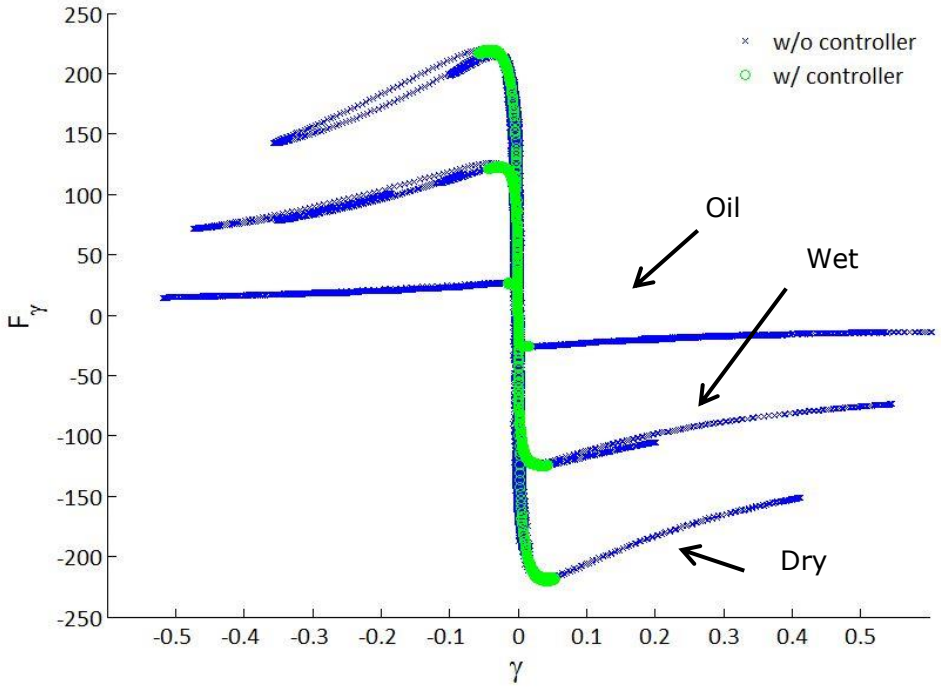

Figure 4-21 Creepage – creep force with and without controller

4.7. Conclusion

In this chapter, three different methods were used to estimate the wheel – roller friction coefficient. First a simple wheel – roller traction model was built and the Kalman filter was applied. As the Kalman filter cannot estimate nonlinear systems, only the AC motor electric torque was directly estimated. Creepage and creep force were further calculated using the dynamic equations of the modelled system. The estimated creepage and creep force curve were then compared to the standard values, and the friction coefficient was identified using the root mean square values. The estimation error was accumulated in this method due to its algorithm, thus the creepage and creep force estimation can be inaccurate given a more complex system model and measurements with significant noise. Therefore, the extended Kalman filter (EKF) is applied to provide direct estimations of a more complex and accurate dynamic model. As shown previously, the estimations given by the EKF method are very close to the measurements. However, when the traction load is included in the estimated system, the EKF method struggles to perform as well. To solve this problem, more simulations have been carried out using the unscented Kalman filter (UKF). The importance of measuring the traction load and the roller speed is also studied by altering the measurement matrix. According to the simulation result, the UKF method can provide accurate estimation of the wheel-rail friction coefficient without the traction load measurement but it is necessary to measure the roller speed.

An anti-slip control algorithm was then developed based on the UKF estimator. Excessive creepage during traction and braking can be significantly reduced with this algorithm. The available adhesion can also be better utilized thus the accelerating and braking time can also be reduced.

All these results have shown that the Kalman filter based estimators can offer reliable estimations of the wheel – roller friction coefficient with the measurement of the traction motor parameters and can also contribute to further applications such as advance control strategies for railway vehicles.

5. Experimental validations of the estimator

As previously discussed in Chapter 4, an unscented Kalman filter can provide the best estimation performance among the studied methods. To test whether the UKF method works as well in practice, some experiments have been carried out using the designed roller rig. In Chapter 4, the importance of measuring the roller speed and the traction load was discussed, and three different observers are used in the experiments to validate this conclusion as well.

5.1. Introduction

In the experiments, the two motors are given the same speed command as shown in equation (5-1). The motor speed command ω_{motor}^{*} changes every 5 seconds from 20 rad/s to 30 rad/s in order to create more creepage. This speed profile is different from that used in Chapter 4 (4-21), as it is not very practical to change the motor speed that frequently(every second).

$$\omega_{motor}^{*}(\text{rad/s}) = \begin{cases} 20\pi & t < 5\text{s} \\ 30\pi & 5\text{s} \le t < 10\text{s} \\ 20\pi & 10\text{s} \le t < 15\text{s} \\ 30\pi & 15\text{s} \le t < 20\text{s} \\ 20\pi & 20\text{s} \le t < 25\text{s} \\ 30\pi & 25\text{s} \le t < 30\text{s} \\ 20\pi & 30s \le t \end{cases} \tag{5-1}$$

Three different unscented Kalman filters are designed to estimate the roller rig system and the state and measurement variables are:

$$\mathrm{x} = \left[I_{\alpha s}, I_{\beta s}, \psi_{\alpha r}, \psi_{\beta r}, \omega_{motor}, U_{\alpha s}, U_{\beta s}, \gamma, F_{\gamma}, \omega_{roller}, \mu, \mu_0, T_{Load} \right]^T \tag{5-2}$$

The only difference between these estimators is the estimation variable matrix. In the first estimator, both the roller speed and the traction load are measured, while the traction load is not included in estimator 2 and the roller speed is not included in estimator 3.

$$\mathrm{z}^{(1)} = \left[I_{\alpha s}, I_{\beta s}, \omega_{motor}, U_{\alpha s}, U_{\beta s}, \omega_{roller}, T_{Load} \right]^T \tag{5-3}$$

$$\mathrm{z}^{(2)} = \left[I_{\alpha s}, I_{\beta s}, \omega_{motor}, U_{\alpha s}, U_{\beta s}, \omega_{roller} \right]^T \tag{5-4}$$

$$\mathrm{z}^{(3)} = \left[I_{\alpha s}, I_{\beta s}, \omega_{motor}, U_{\alpha s}, U_{\beta s}, T_{Load} \right]^T \tag{5-5}$$

Noise convariances matrices **Q** and **R** are set as:

Q=diag[1e-6,1e-6,1e-6,1e-6,1e-6,1e-6,1e-6,1e-2,1e-2,1e-2,1e-2,1e-2,1e-6]

$\mathbf{R}^{(1)}$=diag[1e-6,1e-6,1e-6,1e-6,1e-6,1e-6,1e-6]

$\mathbf{R}^{(2)}= \mathbf{R}^{(3)}$=diag[1e-6,1e-6,1e-6,1e-6,1e-6,1e-6]

First the base condition with no contaminants between the wheel and roller surfaces was tested and the estimations of the creep force, creepage and friction coefficient are shown in Figure 2-4. In case 0, the DC generator is not connected, and the external resistance of the generator decreases from case 1 to case 4, as listed in Table 5-1. As the maximum available creep force decreases significantly when lubrications are added, lower traction load (higher resistance values) are applied for low adhesion cases. In this way, larger ranges of creepage and be tested and more complete creepage-creep force curves can be plotted from the results.

Table 5-1 Load resistance values of the DC generator

	Base	Water	Oil
Case 0	Infinite	Infinite	Infinite
Case 1	3Ω	4.5Ω	7Ω
Case 2	1.5Ω	3Ω	4.5Ω
Case 3	1Ω	1.5Ω	3Ω
Case 4	0Ω	1Ω	1.5Ω

5.2. Estimator 1

The first estimator obtains both the roller speed and the traction load signals. The estimation results are plotted in Figure 5-1.

The difference in the traction load can be found in the plot (a), the output current of the DC generator increases accordingly with the resistance. For each load case, I_{dc} follows the changes of the roller speed as indicated in equation (3-9). The creepage and creep force estimations in plot (b) and (c) show that the creepage and creep force also increases while the traction load is larger.

The friction coefficient estimation in plot (d) shows that the result for case 0 is very low and cannot be true when the wheel and roller surfaces are dry. This estimation error is most possibly caused by the fact that the traction load is negligible in case 0, as shown in plot (a), thus the effect of friction coefficient on the creep force is not significant. Therefore the estimator is not reliable when there is no traction load.

For case 1 to 3, the estimated friction coefficient is about 0.28 but the variation is quite significant and has a similar frequency with the estimated creepage and creep force. When the traction load increases to case 4, the oscillation becomes much less, possibly due to the much larger creepage.

The results therefore prove that the estimator is able to provide acceptable performance with adequate traction load and the estimation error reduces as the traction load increases.

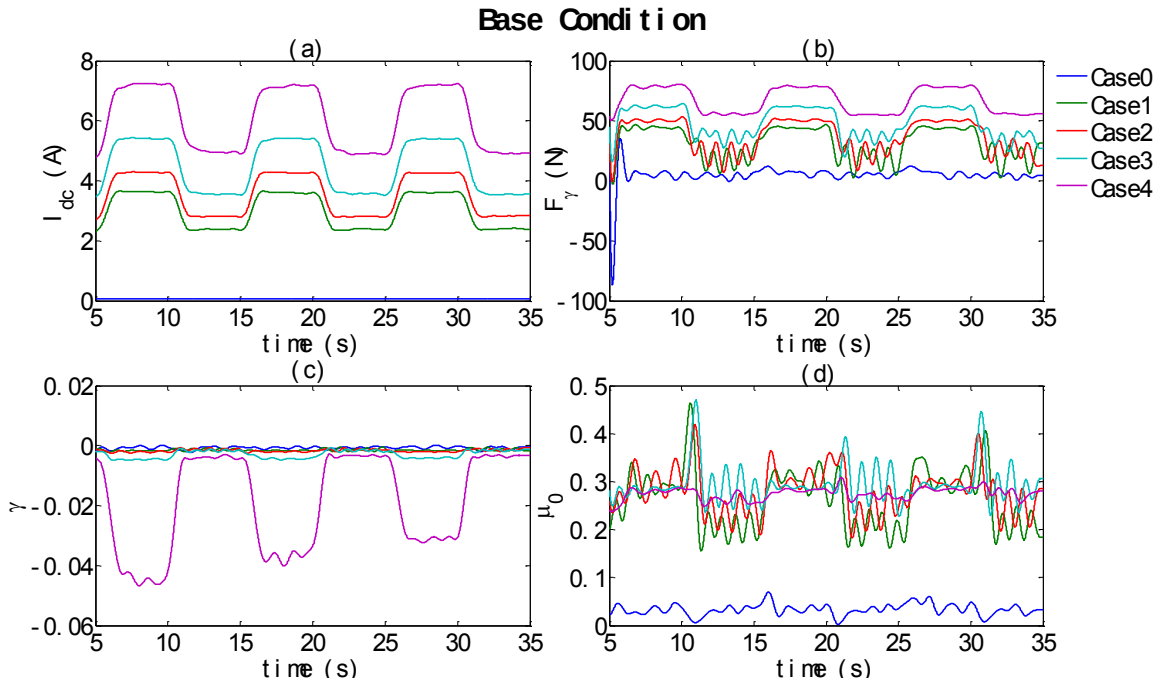

Figure 5-1 Estimation result for the base condition

The performance of the estimator under water and oil contaminations has also been studied. Firstly, water has been sprayed evenly between the wheel and roller surfaces, after the tests and thoroughly cleaning, oil is then sprayed evenly. 5 tests with different DC generator external resistances are proceed with water and oil contaminations, respectively. Under both water and oil contamination conditions, the external resistance of the 5 tested load cases decreases from infinite to 0.5Ω.

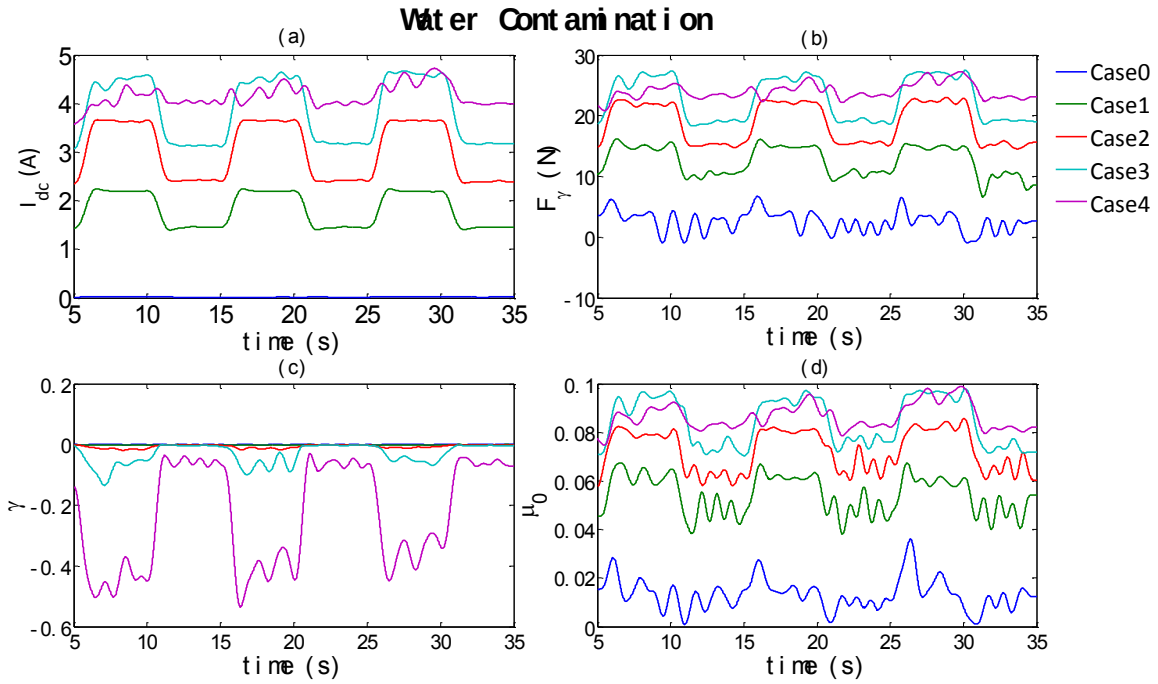

Figure 5-2 Estimation results for the water contamination condition

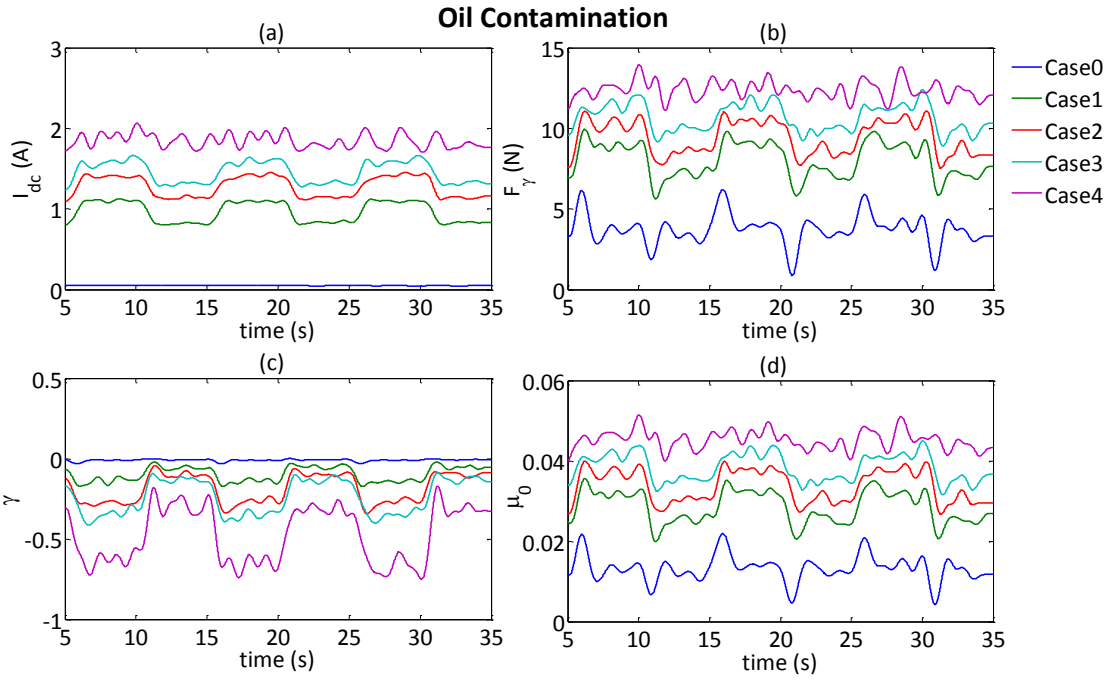

Figure 5-3 Estimation results for the oil contamination condition

Figure 5-2 and Figure 5-3 show the output values of the UKF under water and oil contamination respectively. In plot (a) of Figure 5-2 and Figure 5-3, I_{dc} increases from case 0 to case 3. In case 4, the wheel and roller reaches full slip thus the roller speed does not increase accordingly with the AC motor speed, which explains why the pattern of I_{dc} of case 4 is different from those of other cases.

In plot (d) of Figure 5-2 and Figure 5-3, it is clear that the estimated μ_0 values for each case have the same pattern with the creep force, which means that a higher traction load will result in a higher friction estimation. This trend is also proved in Figure 5-4, which plots the average values of the estimated μ_0 for all the tested cases. This problem is most possibly because that the friction coefficient is very sensitive to the sensor resolution and sample frequency. The inaccuracy of the creep force model can also lead to estimation errors as well. The noise matrices for the system and measurements are also very important to remain the estimator reliable.

Despite the estimation errors discussed above, the average μ_0 estimations under water and oil contaminations still remain around 0.08 and 0.04, respectively.

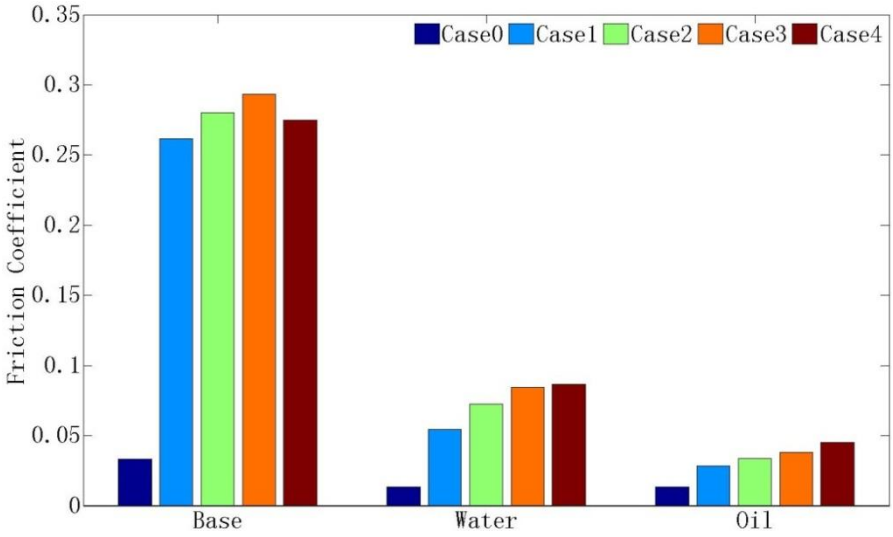

Figure 5-4 Average friction estimation results.

The creepage – creep force curves for the base, water and oil contamination conditions are shown in Figure 5-5. The creepage and creep force points have been curve fitted with the Polach creep force model. The identified friction coefficients for these three conditions are: μ_{base}=0.28, μ_{water}=0.08 and μ_{oil}=0.04. The identified μ0 by the curve fitting are close to the results in Figure 5-4. This good agreement between these two plots shows that the unscented Kalman filter can provide acceptable real time estimation of the wheel – roller friction condition.

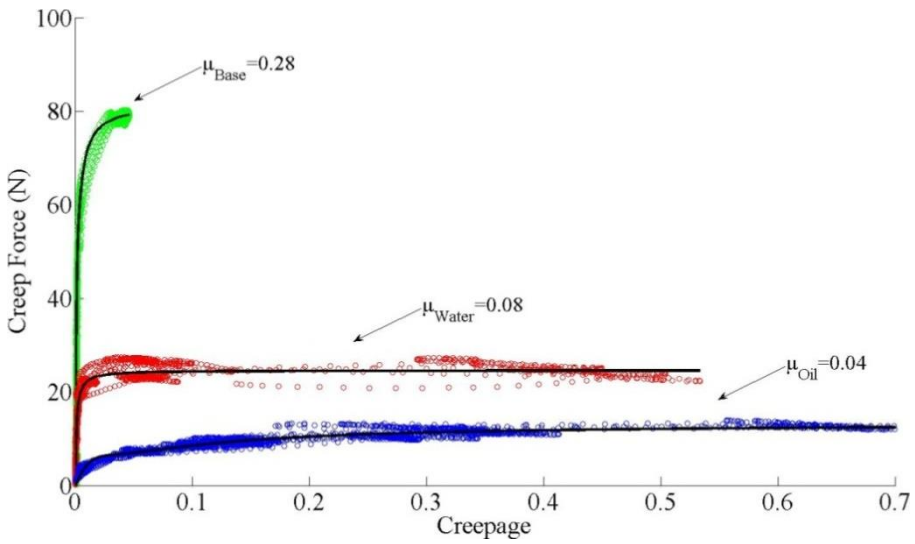

Figure 5-5 Creepage – creep force curve

5.3. Estimator 2

Estimator 2 obtains the roller speed and does not require the measurement of the traction load. The estimation results from estimator 2 are plotted and compared to those from estimator 1, as shown in Figure 5-6 to Figure 5-8. The estimation error of the I_{dc} is negligible for all the 3 conditions (base, water and oil lubrication). It is also very hard to notice the difference between estimator 1 and 2 when comparing the estimation of the γ, $F\gamma$ and μ_0.

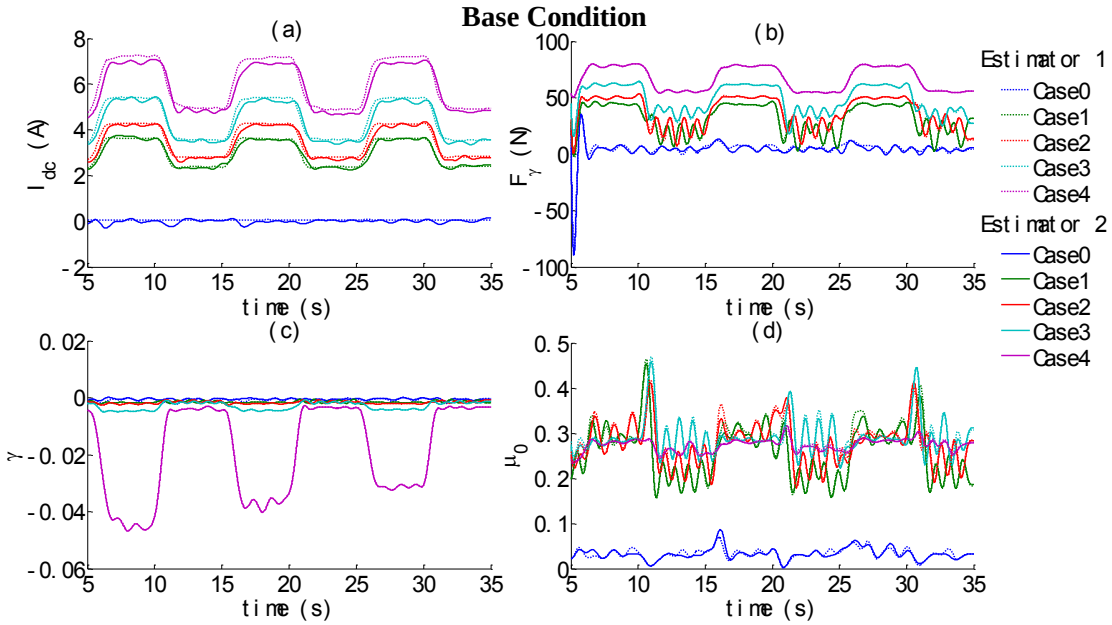

Figure 5-6 Results of estimator 1 and 2 for the base condition

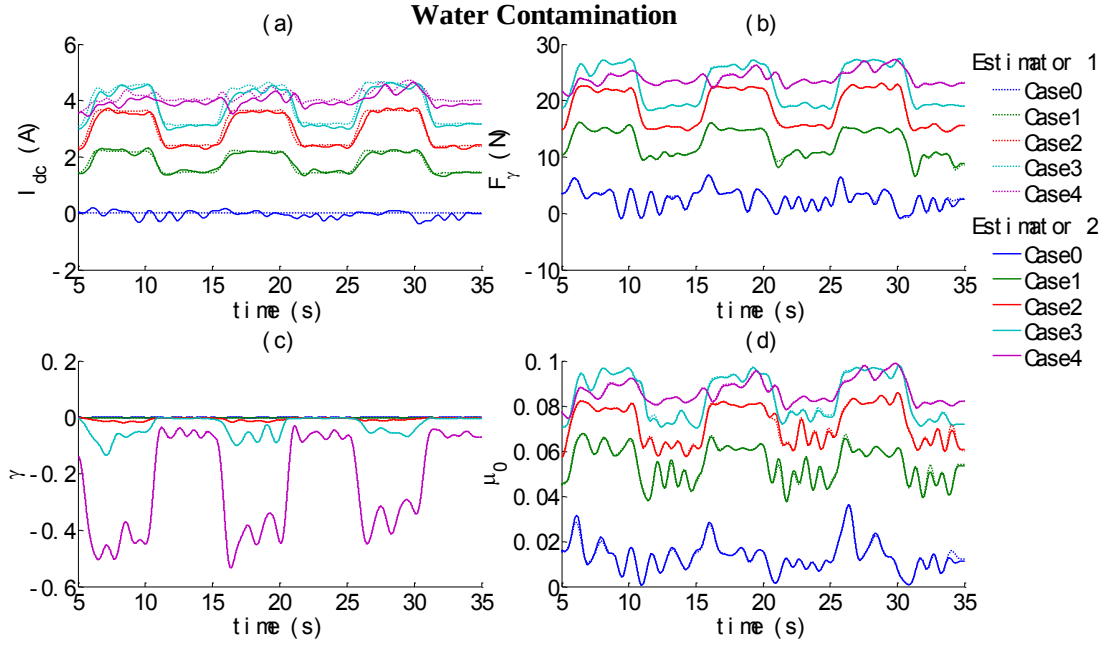

Figure 5-7 Results of estimator 1 and 2 for the water contamination condition

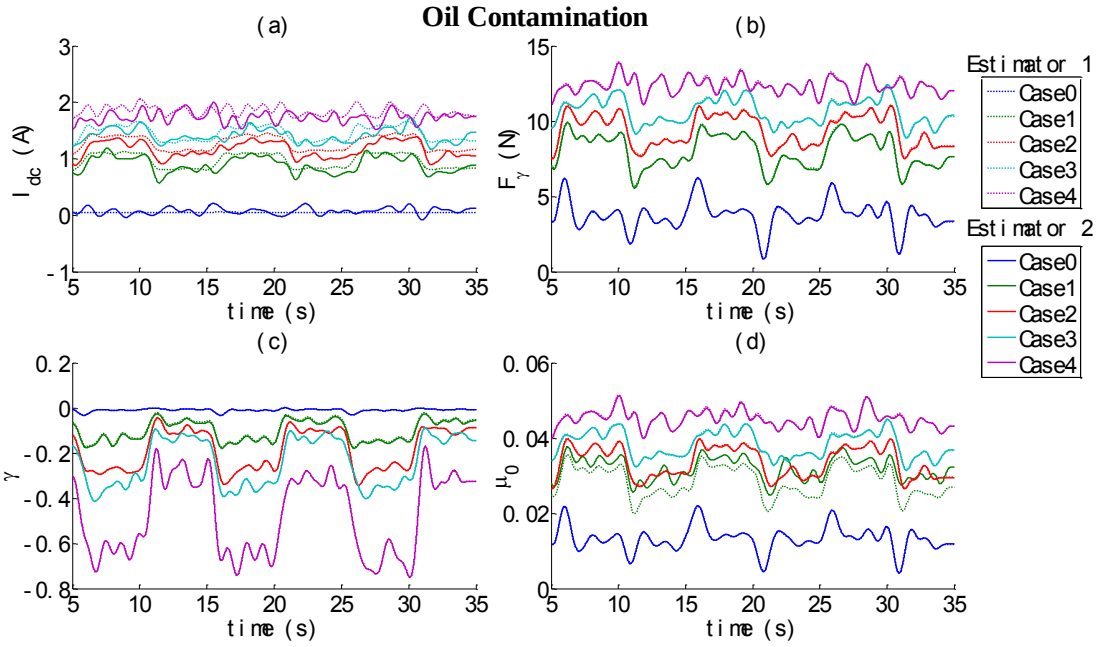

Figure 5-8 Results of estimator 1 and 2 for the oil contamination condition

The estimation errors of μ_0 are calculated by comparing the results from estimator 1 and 2. The average values acquired from estimator 1 and the root mean square values of the estimation errors are plotted in Table 5-2**Error! Reference source not found.**. The RMS values are all very small in all cases, which also indicate that the performance of the estimator 2 is as good as estimator 1.

Table 5-2 Estimation error of the friction coefficient using estimator 2

RMS	Dry	Wet	Oil
Case0	0.19	0.06	0.00
Case1	0.04	0.01	0.13
Case2	0.03	0.00	0.00
Case3	0.02	0.00	0.00
Case4	0.01	0.00	0.00

The estimated creepage – creep force curve is plotted in Figure 5-9, which has the identical shape to that acquired from estimator 1. The identified friction coefficients using the curving fitting method are also the same as those from estimator 1.

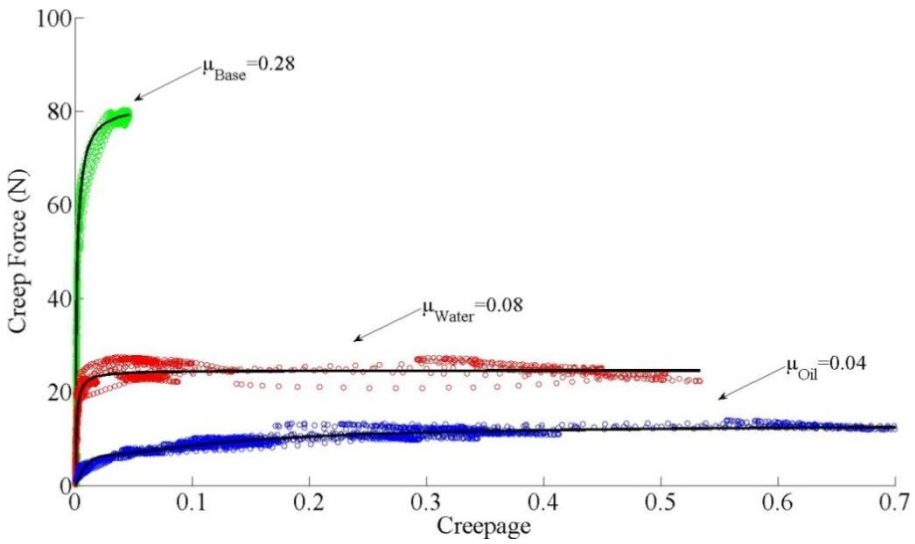

Figure 5-9 Creepage – creep force curve from estimator 2

Therefore, based on the comparison between the performance of estimator 1 and 2, the traction load will have a negligible effect on the estimation results. This conclusion also agrees with the simulation work discussed in section 4.5.

5.4. Estimator 3

Estimator 3 obtains the traction load and does not require the measurement of the roller speed. The same simulation has been carried out using estimator 3. The results are compared to the corresponding results from estimator 1 and are plotted in Figure 5-10 to Figure 5-12. The estimation results are only reliable in case 0 (No traction load). In other load cases, the estimation results of ω_{roller} decreases until the estimation finishes, which indicates that estimator 3 cannot provide reliable estimation of the system.

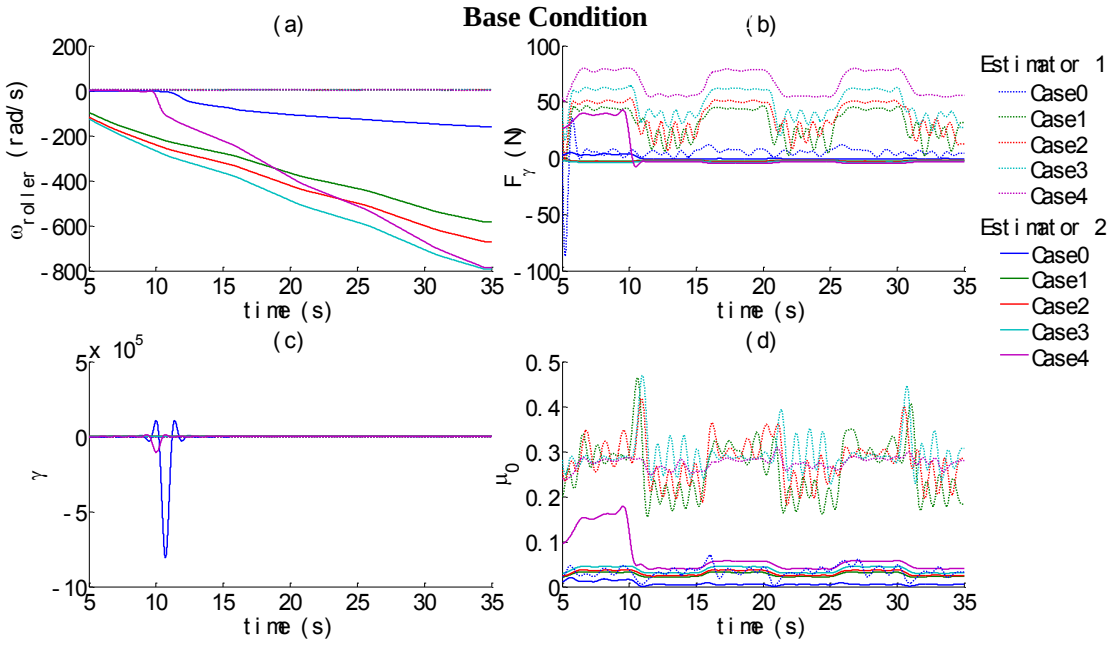

Figure 5-10 Results of estimator 1 and 2 for the base condition

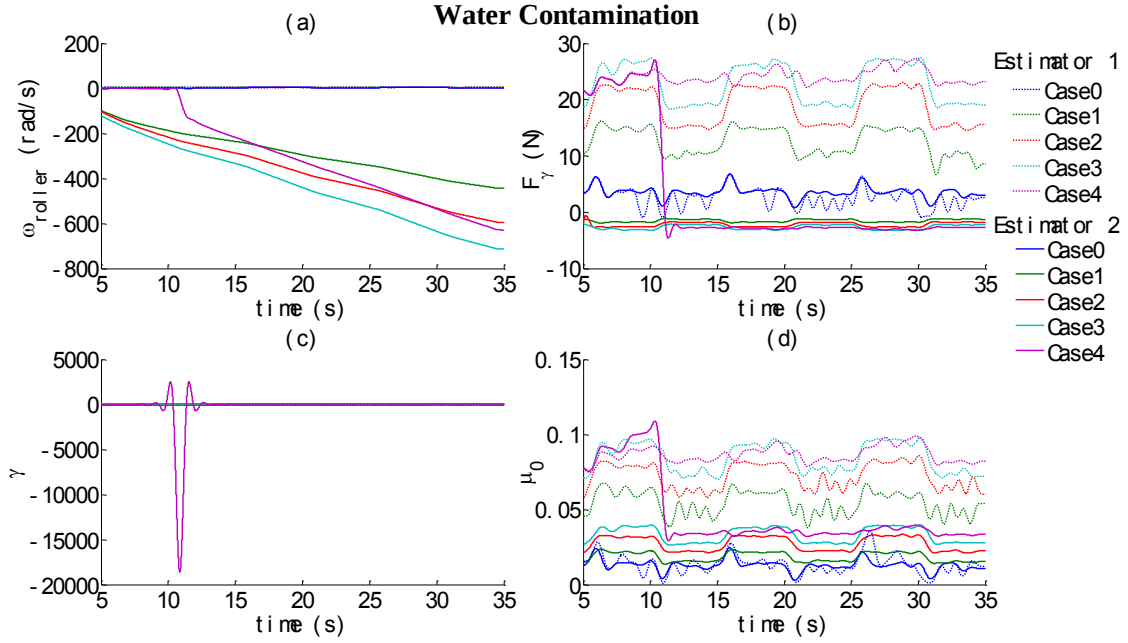

Figure 5-11 Results of estimator 1 and 2 for the water contamination condition

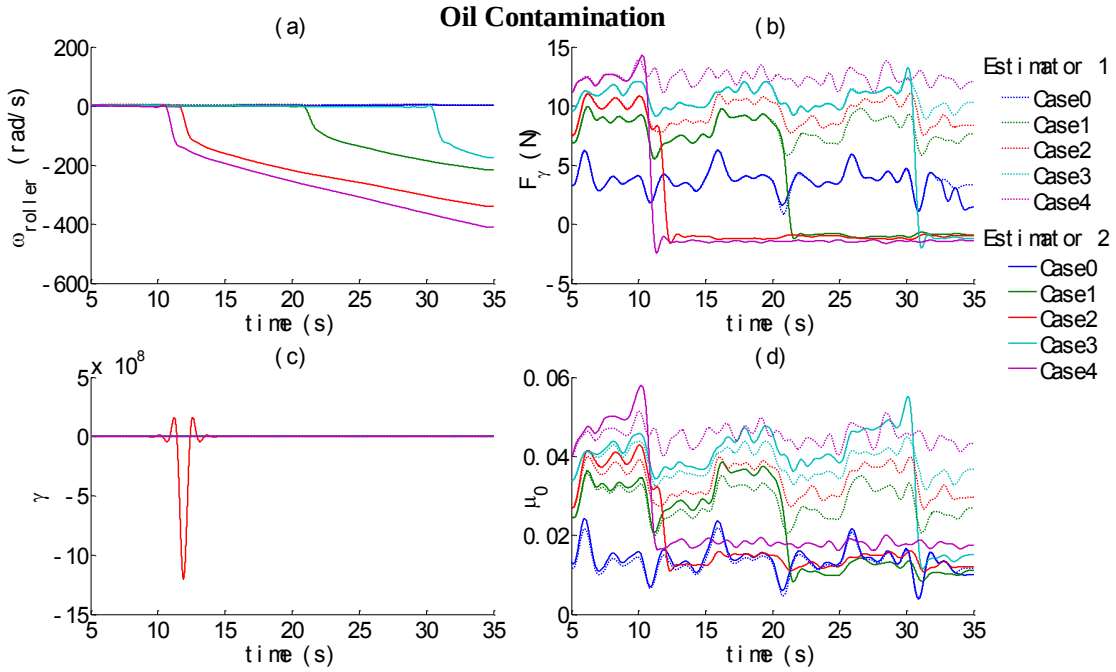

Figure 5-12 Results of estimator 1 and 2 for the oil contamination condition

The estimation errors of μ_0 are calculated by comparing the results from estimator 1 and 2. The average values acquired from estimator 1 and the root mean square values of the estimation errors are plotted in Table 5-3**Error! Reference source not found.**. The RMS values are all very large in most cases, which also indicate that estimator 3 cannot provide acceptable estimation of the system.

Table 5-3 Estimation error of the friction coefficient using estimator 2

RMS/Estimator1	Dry	Wet	Oil
Case 0	0.87	0.31	0.07
Case 1	0.92	0.66	0.39
Case 2	0.90	0.62	0.52
Case 3	0.88	0.61	0.22
Case 4	0.77	0.53	0.54

Therefore, both the real time estimations and the RMS results show that the knowledge of the roller speed is essential in order to achieve reliable estimation of the railway traction system, which agrees with the conclusions in section 4.5.

5.5. Conclusion

Three unscented Kalman filter (UKF) based estimators with different measurements have been tested by experiments reported on in this chapter. Three friction conditions are tested, which are: base condition without contamination; water contamination condition and oil contamination condition. A large range of creepage was covered by varying the traction load for all conditions.

The first estimator measures both the roller speed and traction load. The real time estimation result of the friction coefficient oscillates around 0.28, 0.08 and 0.04 for the base, water and oil conditions. Then the estimated creepage – creep force curves are plotted and the curve fitting method is used to identify the friction coefficients. The identified results are very close to the real time results in most cases. Therefore, estimator 1 is shown to be capable of providing reliable estimations of the railway vehicle traction system.

Estimator 2 is identical to estimator 1, only without the traction load measurement, but the estimation results are identical to those acquired from estimator 1. This indicates that the traction load measurement is not necessary for this task.

Estimator 3 further removes the roller speed measurement from estimator 2, and the estimation results are quite different to those acquired from estimator 1. This indicates that the roller speed measurement is very important to achieve reliable estimations.

These conclusions reached in this chapter agree with the discussions based on the simulation work in section 4.5.

However, there are still some problems with estimator 1 and 2, such as:

- The estimated friction coefficient is not reliable when the traction load is very small.
- The estimated friction coefficient is also influenced by the traction load but still remains in an acceptable range.

6. Conclusions and future work

Monitoring the wheel – rail friction condition is very important to reduce low friction incidents as well as to improve rail vehicle traction and braking performances. An indirect fault detection and identification (FDI) method has been developed in this research due to the difficulty in directly measuring the friction coefficient. Firstly, knowledge about the FDI methods and available techniques are reviewed. The state observer method is finally chosen due to its advantages in railway system monitoring. Available state observer methods were then studied and their advantages and disadvantages are analysed. Other required knowledge was studied and the previous research using the state observers has been reviewed.

To validate the developed method, a 1/5 scaled roller rig was designed with an axle-hung traction arrangement. Complex control and data acquisition systems were developed and used to achieve real time monitoring.

Preliminary work was first done using computer simulation tools. A very simplified traction system was first modelled and estimated using Kalman filter. As a Kalman filter can only work with linear systems, the friction coefficient was identified by a root mean square algorithm. To reduce unnecessary assumptions and improve estimation accuracy, an extended Kalman filter (EKF) was used instead of the basic Kalman filter. The achieved estimation results have been shown to be accurate. However, this method struggles to provide reliable estimation when the traction load is applied.

Then the unscented Kalman filter (UKF) was used to solve this problem. The necessity of measuring the roller speed and traction load are also studied using the UKF. It was discovered that the traction load is not required while knowledge of the roller speed is essential. With adequate measurements, the UKF estimation results are very accurate (less than 1% error).

Based on the estimated friction coefficient, creep force and creepage, a re-adhesion control algorithm has been proposed to reduce the excessive creepage and increase the adhesion utilization rate during accelerating and braking. This control strategy can keep the traction motor works at its optimum point where the largest creep force is achieved. Therefore the shortest accelerating and braking time is reduced to its lowest value. The avoidance of excessive creepage can also reduce wheel and rail wear and reduce corresponding maintenance cost.

Experiments were then carried out to validate the developed UKF estimator. Base condition with no contamination between the wheel and roller surfaces and conditions which the wheel and roller surfaces are contaminated with water and oil are tested. For each of these 3 conditions, 5 different traction load values are used to cover a large

range of creepage. Both the simulation and experiment work have reached the same conclusion on the impact of different measurements.

The experiments show that the UKF estimator can provide reliable estimations of the railway vehicle traction system with adequate measurements but the following problems still remain:

- The estimated friction coefficient is not reliable when the traction load is very small.
- The estimated friction coefficient is also influenced by the traction load but still remain in an acceptable range.

To improve the estimator performance, the noise covariance matrices may need to be tuned to their optimum value. Several adaptive tuning algorithms have been proposed and these methods will be studied and employed in the future work.

The roller rig will also be upgraded to carry out more complex experiments. The upgrades include:

Actuators that can eject different contaminations to the wheel – roller interfaces will be implemented so that the friction condition can be changed during the experiment at a certain time point. In this way, the response time of the estimator can be evaluated.

Relays that can alter the external resistance of the DC generator could also be implemented so that the traction load can be changed during the experiment at a certain time point. In this way, the estimator performance under varying traction load can also be studied.

References

[1] D. f. T. Rail Accident Investigation Branch, " Autumn Adhesion Investigation Part 3: Review of adhesion-related incidents Autumn 2005. Jan 2007."

[2] A. K. S. Jardine, D. Lin, and D. Banjevic, "A review on machinery diagnostics and prognostics implementing condition-based maintenance," *Mechanical systems and signal processing,* vol. 20, pp. 1483-1510, 2006.

[3] S. Bruni, R. Goodall, T. Mei, and H. Tsunashima, "Control and monitoring for railway vehicle dynamics," *Vehicle System Dynamics,* vol. 45, pp. 743-779, 2007.

[4] V. Venkatasubramanian, R. Rengaswamy, and S. N. Kavuri, "A review of process fault detection and diagnosis:: Part II: Qualitative models and search strategies," *Computers & Chemical Engineering,* vol. 27, pp. 313-326, 2003.

[5] V. Venkatasubramanian, R. Rengaswamy, S. N. Kavuri, and K. Yin, "A review of process fault detection and diagnosis:: Part III: Process history based methods," *Computers & Chemical Engineering,* vol. 27, pp. 327-346, 2003.

[6] V. Venkatasubramanian, R. Rengaswamy, K. Yin, and S. N. Kavuri, "A review of process fault detection and diagnosis:: Part I: Quantitative model-based methods," *Computers & Chemical Engineering,* vol. 27, pp. 293-311, 2003.

[7] J. Gertler, "Analytical redundancy methods in fault detection and isolation," 1991, pp. 9-21.

[8] R. E. Kalman, "A new approach to linear filtering and prediction problems," *Journal of basic Engineering,* vol. 82, pp. 35-45, 1960.

[9] D. Simon, Optimal state estimation: Kalman, H [infinity] and nonlinear approaches: John Wiley and Sons, 2006.

[10] G. Welch and G. Bishop, "An introduction to the Kalman filter," *Design,* vol. 7, pp. 1-16, 2001.

[11] S. J. Julier and J. K. Uhlmann, "Unscented filtering and nonlinear estimation," *Proceedings of the IEEE,* vol. 92, pp. 401-422, 2004.

[12] P. S. Maybeck, *Stochastic models, estimation and control* vol. 1: Academic Pr, 1979.

[13] M. S. Grewal and A. P. Andrews, *Kalman filtering: theory and practice using MATLAB* vol. 2: Wiley Online Library, 2001.

[14] S. J. Julier, J. K. Uhlmann, and H. F. Durrant-Whyte, "A new approach for filtering nonlinear systems," in *Proceedings of the American Control Conference*, Seattle, Washington USA, 1995, pp. 1628-1632.

[15] L. Jie and Z. Yanru, "Comparison of three Kalman filters for speed estimation of induction machines," in *Industry Applications Conference, Fourtieth IAS Annual Meeting*, Hong Kong, 2005, pp. 1792-1797 Vol. 3.

[16] R. van der Merwe and E. A. Wan, "The square-root unscented Kalman filter for state and parameter-estimation," in *Proceedings of IEEE International Conference on Acoustics, Speech, and Signal Processing (ICASSP '01)*, Salt Lake City, Utah, USA, 2001, pp. 3461-3464 vol.6.

[17] E. A. Wan and R. van der Merwe, "The unscented Kalman filter for nonlinear estimation," in *Adaptive Systems for Signal Processing, Communications and Control Symposium*, Lake Louise, Alberta, Canada, 2000, pp. 153-158.

[18] A. Doucet and A. M. Johansen, "A tutorial on particle filtering and smoothing: Fifteen years later," ed: Oxford, UK: Oxford University Press, 2009.

[19] M. Arnold and H. Netter, "Apporoximation of contact geometry in the dynamical simulation of wheel-rail," *Mathematical and Computer Modelling of Dynamical Systems,* vol. 4, pp. 162-184, 1998/01/01 1998.

[20] A. De Pater, "The approximate determination of the hunting movement of a railway vehicle by aid of the method of Krylov and Bogoljubov," *Applied Scientific Research,* vol. 10, pp. 205-228, 1961.

[21] A. D. De Pater, "The Geometrical Contact between Track and Wheelset," *Vehicle System Dynamics,* vol. 17, pp. 127-140, 1988/01/01 1988.

[22] P. Arrus, A. de Pater, and P. Meyers, "The stationary motion of a one-axle vehicle along a circular curve with real rail and wheel profiles," *Vehicle System Dynamics,* vol. 37, pp. 29-58, 2002.

[23] A. Shabana and J. Sany, "An Augmented Formulation for Mechanical Systems with Non-Generalized Coordinates: Application to Rigid Body Contact Problems," *Nonlinear Dynamics,* vol. 24, pp. 183-204, 2001.
[24] J. Pombo and J. Ambrosio, "A computational efficient general wheel-rail contact detection method," *Journal of mechanical science and technology,* vol. 19, pp. 411-421, 2005.
[25] J. Pombo, J. Ambrósio, and M. Silva, "A new wheel–rail contact model for railway dynamics," *Vehicle System Dynamics,* vol. 45, pp. 165-189, 2007.
[26] G. Chen and W. Zhai, "A new wheel/rail spatially dynamic coupling model and its verification," *Vehicle System Dynamics,* vol. 41, pp. 301-322, 2004.
[27] A. A. Shabana, K. E. Zaazaa, J. L. Escalona, and J. R. Sany, "Development of elastic force model for wheel/rail contact problems," *Journal of sound and vibration,* vol. 269, pp. 295-325, 2004.
[28] T. Mazilu, "Some aspects of the elastic wheel/rail bi-contact," in *Proc. of 9 th IFToMM International Symposium on Theories of Machines and Mechanisms*, Bucharest, 2005, pp. 541-546.
[29] A. H. Wickens, Fundamentals of rail vehicle dynamics: guidance and stability: Swets & Zeitlinger Publishers, 2003.
[30] S. Iwnicki, Handbook of railway vehicle dynamics: CRC Press, 2006.
[31] J. Piotrowski and H. Chollet, "Wheel–rail contact models for vehicle system dynamics including multi-point contact," *Vehicle System Dynamics,* vol. 43, pp. 455-483, 2005/06/01 2005.
[32] O. Polach, "A fast wheel-rail forces calculation computer code," *Vehicle System Dynamics,* vol. 33, pp. 728-739, 2000.
[33] O. Polach, "Creep forces in simulations of traction vehicles running on adhesion limit," *Wear,* vol. 258, pp. 992-1000, 2005.
[34] G. Charles and R. Goodall, "Low Adhesion Estimation," in The Institution of Engineering and Technology International Conference on Railway Condition Monitoring., Birmingham, UK, 2006, pp. 96-101.
[35] J. Kalker, "Survey of Wheel—Rail Rolling Contact Theory," *Vehicle System Dynamics,* vol. 8, pp. 317-358, 1979.
[36] J. Kalker, "A fast algorithm for the simplified theory of rolling contact," *Vehicle System Dynamics,* vol. 11, pp. 1-13, 1982.
[37] J. Kalker, "Wheel-rail rolling contact theory," *Wear,* vol. 144, pp. 243-261, 1991.
[38] P. Shackleton and S. Iwnicki, "Comparison of wheel–rail contact codes for railway vehicle simulation: an introduction to the Manchester Contact Benchmark and initial results," *Vehicle System Dynamics,* vol. 46, pp. 129-149, 2008.
[39] A. Jaschinski, H. Chollet, S. Iwnicki, A. Wickens, and J. Würzen, "The application of roller rigs to railway vehicle dynamics," *Vehicle System Dynamics,* vol. 31, pp. 345-392, 1999.
[40] P. Allen and S. D. Iwnicki, "The critical speed of a railway vehicle on a roller rig," *Proceedings of the Institution of Mechanical Engineers, Part F: Journal of Rail and Rapid Transit,* vol. 215, pp. 55-64, 2001.
[41] M. Lata, "The modern wheelset drive system and possibilities of modelling the torsion dynamics," *Transport,* vol. 23, pp. 172-181, 2008/01/01 2008.
[42] R. J. Hill, "Electric railway traction Part 2 Traction drives with three-phase induction motors " *Power Engineering Journal,* vol. 8, pp. 143-152, 1994.
[43] R. J. Hill, "Traction drives and converters," in Railway Electrification Infrastructure and Systems, 2007 3rd IET Professional Development Course on, 2007, pp. 185-196.
[44] A. Steimel, "Electric railway traction in Europe," *Industry Applications Magazine, IEEE,* vol. 2, pp. 6-17, 1996.
[45] Y. Hagiwara, M. Tanaka, and M. Ueno, "Evaluation of advantages of high-speed EMU in the case of the Series 700 Shinkansen high-speed train with IGBT applied traction system," in *Proceedings of the World Congress on Railway Research*, 2001.
[46] K. Hasse, "Drehzahlgelverfahren für schnelle umkehrantriebe mit stromrichtergespeisten asynchron-kurzschlusslaufer-motoren," *Regelungstechnik,* vol. 20, pp. 60-66, 1972.
[47] F. Blaschke, "The principle of field orientation as applied to the new TRANSVECTOR closed loop control system for rotating field machines," *Siemens review,* vol. 34, pp. 217-220, 1972.
[48] R. Park, "Two-reaction theory of synchronous machines generalized method of analysis-part I," *American Institute of Electrical Engineers, Transactions of the,* vol. 48, pp. 716-727, 1929.

[49] I. Takahashi and T. Noguchi, "A new quick-response and high-efficiency control strategy of an induction motor," *Industry Applications, IEEE Transactions on*, pp. 820-827, 1986.
[50] M. Depenbrock, "Direct self-control (DSC) of inverter-fed induction machine," *Power Electronics, IEEE Transactions on*, vol. 3, pp. 420-429, 1988.
[51] M. Vasudevan, R. Arumugam, and S. Paramasivam, "Real time implementation of viable torque and flux controllers and torque ripple minimization algorithm for induction motor drive," *Energy conversion and management*, vol. 47, pp. 1359-1371, 2006.
[52] R. Isermann, "Diagnosis methods for electronic controlled vehicles," *Vehicle System Dynamics*, vol. 36, pp. 77-117, 2001.
[53] Y. Hayashi, H. Tsunashima, and Y. Marumo, "Fault detection of railway vehicle suspension systems using multiple-model approach," *Journal of Mechanical Systems for Transportation and Logistics*, vol. 1, pp. 88-99, 2008.
[54] T. Mei and X. Ding, "New condition monitoring techniques for vehicle suspensions," 2008, pp. 1-6.
[55] R. Goodall, "Active railway suspensions: Implementation status and technological trends," *Vehicle System Dynamics*, vol. 28, pp. 87-117, 1997.
[56] C. P. Ward, R. M. Goodall, and R. Dixon, "Creep force estimation at the wheel-rail interface," presented at the 22nd International Symposium on Dynamics of Vehicles on Roads and Tracks (IAVSD2011 Symposium Proceedings), Manchester, UK, 2011.
[57] T. Mei and I. Hussain, "Detection of wheel-rail conditions for improved traction control," in *The 4th International Conference on Railway Traction Systems (RTS2010)*, Birmingham, UK 2010, , pp. 1-6.
[58] P. Gáspár, Z. Szabó, and J. Bokor, "Observer based estimation of the wheel-rail friction coefficient," in Computer Aided Control System Design, 2006 IEEE International Conference on Control Applications, 2006 IEEE International Symposium on Intelligent Control, 2006 IEEE, 2006, pp. 1043-1048.
[59] P. Gáspár, Z. Szabó, and J. Bokor, "Observer based estimation of the wheel-rail friction coefficient," in *IEEE International Conference on Control Applications*, Munich, Germany, 2006, pp. 1043-1048.
[60] M. Covino, M. L. Grassi, and E. Pagano, "Traction electric drives: an indirect identification method of friction forces," in *IEEE International Electric Machines and Drives Conference Record.*, Milwaukee, USA, 1997, pp. TA2/5.1-TA2/5.3.
[61] R. Rizzo and D. Iannuzzi, "Indirect friction force identification for application in traction electric drives," *Mathematics and computers in simulation*, vol. 60, pp. 379-387, 2002.
[62] G. Charles, R. Dixon, and R. Goodall, "Condition Monitoring Approaches to Estimating Wheel-Rail Profile," in *Proceedings of UKACC Control Conference, Manchester*, 2008.
[63] G. Charles, R. Goodall, and R. Dixon, "A least mean squared approach to wheel-rail profile estimation," 2008.
[64] K. Goda and R. Goodall, "A fault-detection-and-isolation system for railway vehicles," *Nippon Kikai Gakkai Kotsu, Butsuryu Bumon Taikai Koen Ronbunshu*, vol. 12, pp. 155-158, 2003.
[65] J. Real, P. Salvador, L. Montalbán, and M. Bueno, "Determination of rail vertical profile through inertial methods," *Proceedings of the Institution of Mechanical Engineers, Part F: Journal of Rail and Rapid Transit*, vol. 225, p. 14, 2011.
[66] K. Young-Real, S. Seung-Ki, and P. Min-Ho, "Speed sensorless vector control of induction motor using extended Kalman filter," *Industry Applications, IEEE Transactions on*, vol. 30, pp. 1225-1233, 1994.
[67] D. J. Atkinson, P. P. Acarnley, and J. W. Finch, "Observers for induction motor state and parameter estimation," *Industry Applications, IEEE Transactions on*, vol. 27, pp. 1119-1127, 1991.
[68] K. Shi, T. Chan, Y. Wong, and S. Ho, "Speed estimation of an induction motor drive using an optimized extended Kalman filter," *Industrial Electronics, IEEE Transactions on*, vol. 49, pp. 124-133, 2002.
[69] K. Fujikawa, Z. Yang, H. Kobayashi, and T. Koga, "Robust and fast speed control for torsional system based on state-space method," 1991, pp. 687-692 vol. 1.

[70] J. H. Chow, S. H. Javid, J. J. Sanchez-Gasca, C. E. J. Bowler, and J. S. Edmonds, "Torsional Model Identification for Turbine-Generators," *Energy Conversion, IEEE Transactions on*, vol. EC-1, pp. 83-91, 1986.
[71] I. Yasuoka, T. Henmi, Y. Nakazawa, and I. Aoyama, "Improvement of re-adhesion for commuter trains with vector control traction inverter," in *Power Conversion Conference-Nagaoka 1997.*,, 1997, pp. 51-56.
[72] W. S. Kim, Y. S. Kim, J. K. Kang, and S. K. Sul, "Electro-mechanical re-adhesion control simulator for inverter-driven railway electric vehicle," in *Industry Applications Conference, 1999. Thirty-Fourth IAS Annual Meeting. Conference Record of the 1999 IEEE*, 1999, pp. 1026-1032.
[73] Y. Matsumoto, N. Eguchi, and A. Kawamura, "Novel re-adhesion control for train traction system of the," in *Industrial Electronics Society, 2001. IECON'01. The 27th Annual Conference of the IEEE*, 2001, pp. 1207-1212.
[74] A. Kawamura, K. Takeuchi, T. Furuya, M. Cao, Y. Takaoka, and K. Yoshimoto, "Measurement of tractive force and the new maximum tractive force control by the newly developed tractive force measurement equipment," *Electrical Engineering in Japan*, vol. 149, pp. 49-59, 2004.
[75] S. Kadowaki, K. Ohishi, T. Hata, N. Iida, M. Takagi, T. Sano, *et al.*, "Antislip readhesion control based on speed-sensorless vector control and disturbance observer for electric commuter train—Series 205-5000 of the East Japan Railway Company," *Industrial Electronics, IEEE Transactions on*, vol. 54, pp. 2001-2008, 2007.
[76] Y. Shimizu, K. Ohishi, T. Sano, and S. Yasukawa, "Anti - slip/slid re - adhesion control based on disturbance observer considering bogie vibration," *Electrical Engineering in Japan*, vol. 172, pp. 37-46, 2010.
[77] M. Spiryagin, K. S. Lee, and H. H. Yoo, "Control system for maximum use of adhesive forces of a railway vehicle in a tractive mode," *Mechanical systems and signal processing*, vol. 22, pp. 709-720, 2008.
[78] M. Spiryagin, Y. Q. Sun, C. Cole, S. Simson, and I. Persson, "Development of traction control for hauling locomotives," *Journal of System Design and Dynamics*, vol. 5, pp. 1214-1225, 2011.
[79] T. Mei, J. Yu, and D. Wilson, "A mechatronic approach for effective wheel slip control in railway traction," *Proceedings of the Institution of Mechanical Engineers, Part F: Journal of Rail and Rapid Transit*, vol. 223, pp. 295-304, 2009.
[80] A. Wickens, "Paper 1: The Dynamics of Railway Vehicles on Straight Track: Fundamental Considerations of Lateral Stability," in *Proceedings of the Institution of Mechanical Engineers, Conference Proceedings*, 1965, pp. 29-44.
[81] T. Matsudaira, N. Matsui, S. Arai, and K. Yokose, "Problems on hunting of railway vehicle on test stand," *Publication of: ASSOCIATION OF AMERICAN RAILROADS*, 1971.
[82] R. Illingworth, "Railway wheelset lateral excitation by track irregularities," *Vehicle System Dynamics*, vol. 6, pp. 144-147, 1977.
[83] M. Jochim, "Konstruktion eines Versuchsdrehgestells," Term study, Lehrstuhl B fur Mechanik, Tu-Munchen and DLR, Oberpfaffenhofen, 1984.
[84] M. Jochim, "Analyse der Dynamik eines Schienenfahrzeuges," Diploma thesis, Lehrstuhl B fur Mechanik, TU-Munchen and DLR, Oberpfaffenhofen, 1987.
[85] A. Jaschinski, "On the application of similarity laws to a scaled railway bogie model," 1990.
[86] *Roue de Grenoble*. Available: http://www.inrets.fr/linstitut/unites-de-recherche-unites-de-service/grettia/equipements-et-logiciels/roue-de-grenoble.html
[87] S. D. Iwnicki and A. H. Wickens, "Validation of a MATLAB railway vehicle simulation using a scale roller rig," *Vehicle System Dynamics*, vol. 30, pp. 257-270, 1998.
[88] V. K. Jadon and S. Verma, *Analysis and Design of Machine Elements*: I.K. International Publishing House Pvt. Limited, 2010.
[89] A. Siemens, SIMOVERT MASTERDRIVES VECTOR CONTROL OPERATIONAL INSTRUCTIONS, 1998.
[90] C. I. Hubert, *Electric machines*: Prentice-Hall, 2002.
[91] B. K. Bose, *Modern power electronics and AC drives*. New Jersey: Prentice Hall PTR, 1986.
[92] P. Vas, *Sensorless vector and direct torque control* vol. 729: Oxford university press Oxford, UK, 1998.

Appendix A

Table A-0-1 List of roller rig components

ITEM NO.	ITEM NAME	QUANTITY	DRAWING/CATALOGUE NO.
1	WHEEL AXLE	2	DRAWING #1
2	WHEEL	4	DRAWING #2
3	BOGIE FRAME	2	DRAWING #3
4	SPACER 1	4	DRAWING #4
5	SPACER 2	2	DRAWING #5
6	MOTOR BASE	2	DRAWING #6
7	ANTI-PITCH FRAME	2	DRAWING #7
8	ANTI-PITCH ARM	2	DRAWING #8
9	ENCODER HOLDER 1	2	DRAWING #9
10	ENCODER HOLDER 2	2	DRWAING #10
11	ENCODER SHAFT	4	DRAWING #11
12	ROLLER AXLE	2	DRAWING #12
13	ROLLER	4	DRAWING #13
14	GROUND FRAME	1	DRAWING #14
15	BOGIE ARM 1	1	DRAWING #15
16	BOGIE ARM 2	1	DRAWING #16
17	SPACER 3	4	DRAWING #17
18	AXLE EXTENSION	2	DRAWING #18
19	PULLEY SHAFT 1	2	DRAWING #19
20	PULLEY SHAFT 2	2	DRAWING #20
21	ANGLE SECTION 1	4	DRAWING #21
22	ANGLE SECTION 2	4	DRAWING #22
23	RUBBER BUSH	8	RS CATALOGUE, 237-1764
24	PLUMMER BLOCK 1	4	RS CATALOGUE, 339-8445
25	PLUMMER BLOCK 2	4	RS CATALOGUE, 339-8467
26	PLUMMER BLOCK 3	4	RS CATALOGUE
27	GEAR 1	2	HPC GEAR, PG2-120
28	GEAR 2	2	HPC GEAR, G2-40
29	TIMINGPULLEY 1	4	HPC GEAR 20T 5-15, PT
30	TIMING PULLEY 2	4	HPC GEAR 84T 5-15, PT
31	TIMING BELT	4	HPC GEAR T5/750
32	INVERTER DRIVE	2	SIEMENS 6SE7016
33	AC MOTOR	2	SIEMENS 1LA7083

34	DATA ACQUISITION CARD	1	NATIONAL INSTRUMENTS, 779348-01
35	ROTATRY ENCODER	4	RS CATALOGUE, 441-6134

Appendix B

Drawings for the roller rig

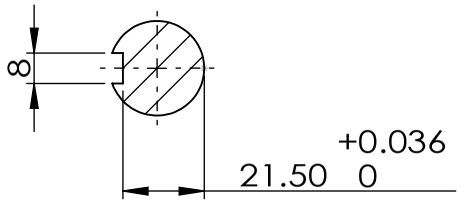

SECTION A-A

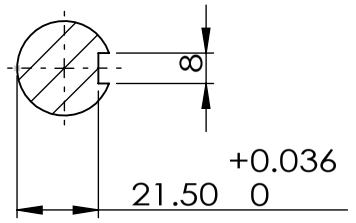

SECTION B-B

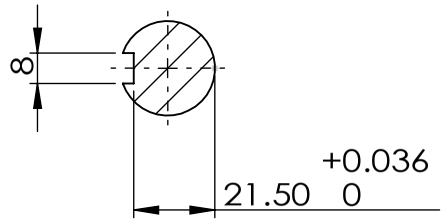

SECTION C-C

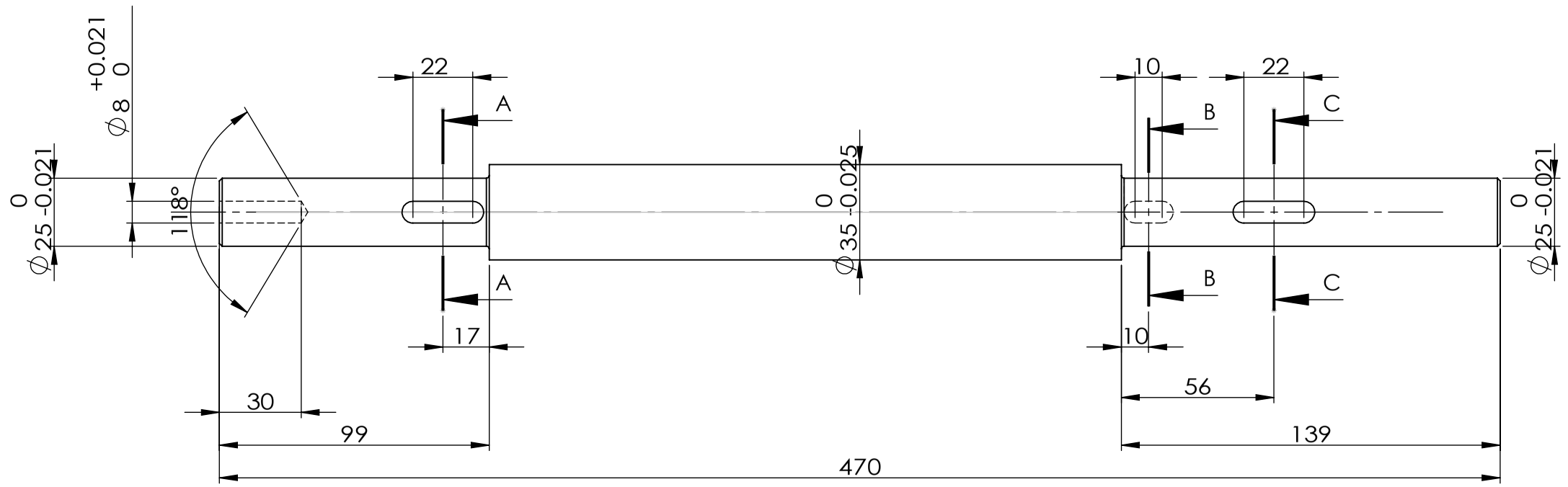

UNSPECIFIED CHAMFER C=1
UNSPECIFIED FILLET R=1

UNLESS OTHERWISE SPECIFIED: DIMENSIONS ARE IN MILLIMETERS SURFACE FINISH: Ra=25 TOLERANCES: MEDIUM LINEAR: ANGULAR:		FINISH:			DEBUR AND BREAK SHARP EDGES	DO NOT SCALE DRAWING	REVISION
	NAME	SIGNATURE	DATE			TITLE:	
DRAWN	YUNSHI ZHAO					WHEELSET AXLE	
CHK'D							
APPV'D							
MFG							
Q.A				MATERIAL: STEEL		DWG NO. 1	A3
				WEIGHT:		SCALE:1:2	SHEET 1 OF 1

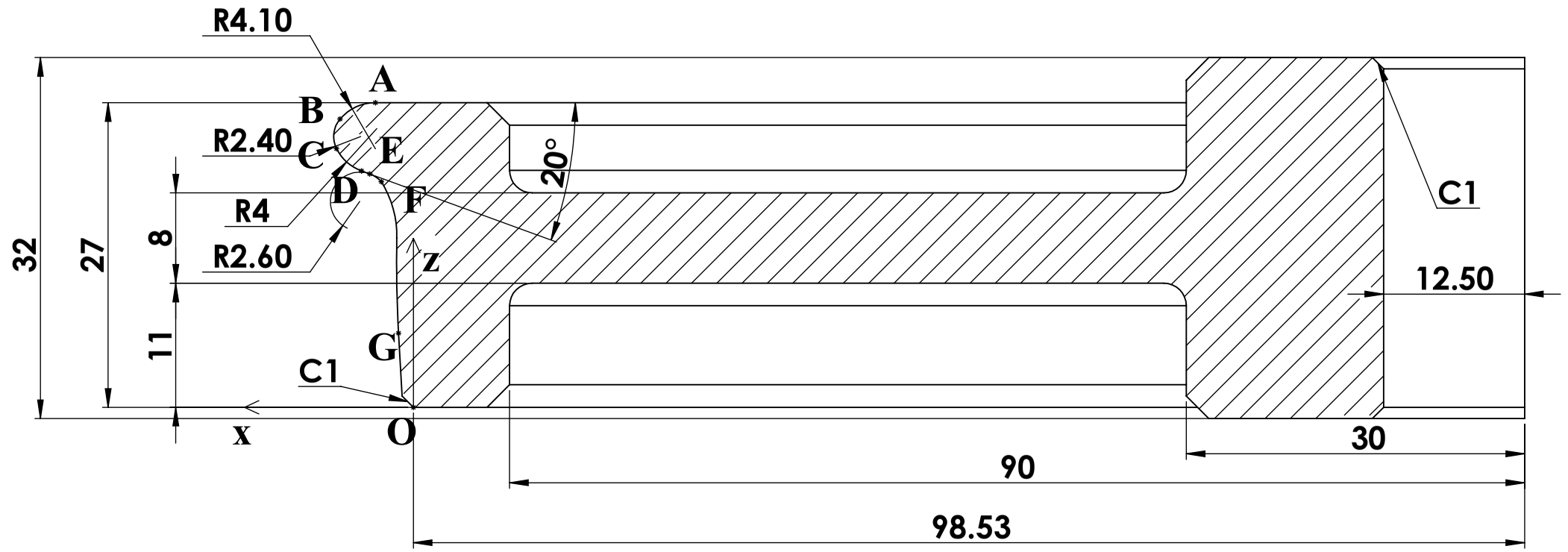

SECTION A-A
SCALE 2 : 1

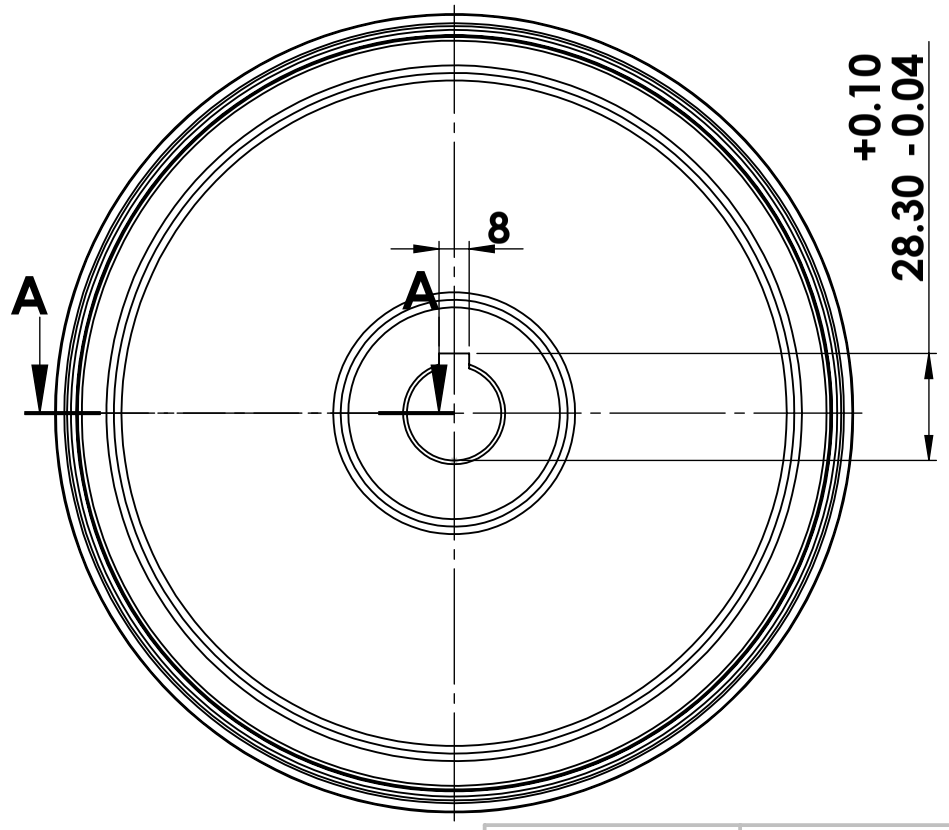

TABLE 2	
CO-ORDINATES	
BETWEEN	
F-G	
X	Z
2.158	20
1.569	19
1.287	18
1.104	17
0.978	16
0.889	15
0.827	14
0.785	13
0.758	12
0.743	11
0.734	10
0.722	9
0.7	8
0.656	7
0.631	6.6

TABLE 1		
CO-ORDINATES A-K		
POINTS	X	Z
O	0	0
A	2.689	27
B	5.815	26.953
C	6.134	22.933
D	3.92	20.953
E	3.185	20.685
F	2.158	20
G	0.629	6.568

UNSPECIFIED CHAMFER C=2

UNLESS OTHERWISE SPECIFIED: DIMENSIONS ARE IN MILLIMETERS SURFACE FINISH: TOLERANCES: LINEAR: ANGULAR:		FINISH:		DEBUR AND BREAK SHARP EDGES		DO NOT SCALE DRAWING	REVISION
	NAME	SIGNATURE	DATE			TITLE:	
DRAWN	YUNSHI ZHAO		13/02/2012			WHEEL	
CHK'D							
APPV'D							
MFG							
				MATERIAL: STEEL		DWG NO. 2	A3
				WEIGHT:		SCALE:1:2	SHEET 1 OF 1

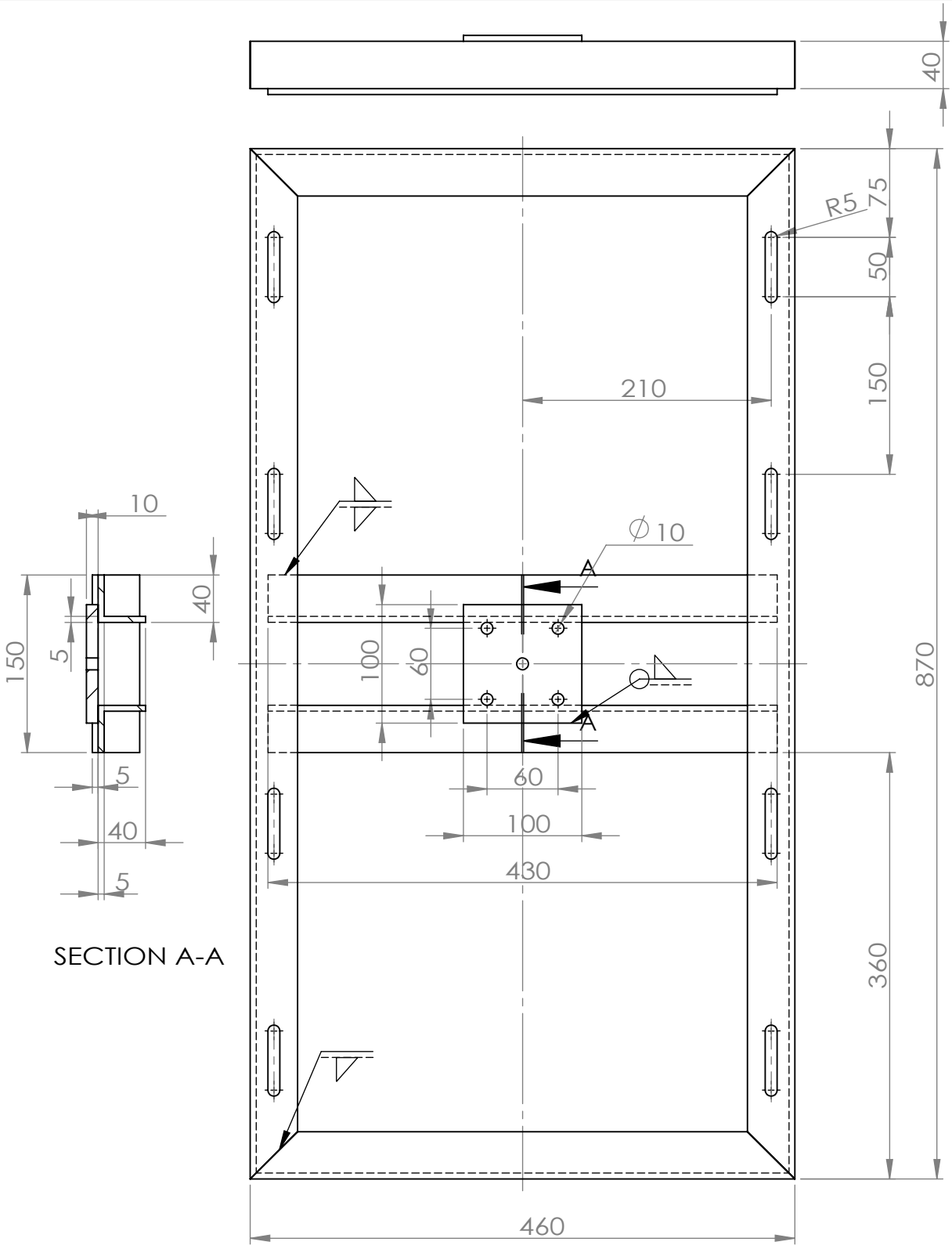

SECTION A-A

WELD OF ANGLE STEEL 40X40X5

UNLESS OTHERWISE SPECIFIED: DIMENSIONS ARE IN MILLIMETERS SURFACE FINISH: TOLERANCES: LINEAR: ANGULAR:		FINISH:		DEBUR AND BREAK SHARP EDGES		DO NOT SCALE DRAWING	REVISION
	NAME	SIGNATURE	DATE			TITLE:	
DRAWN	YUNSHI ZHAO					BOGIE FRAME	
CHK'D							
APPV'D							
MFG							
Q.A				MATERIAL: STEEL		DWG NO. 3	A4
				WEIGHT:		SCALE:1:20	SHEET 1 OF 1

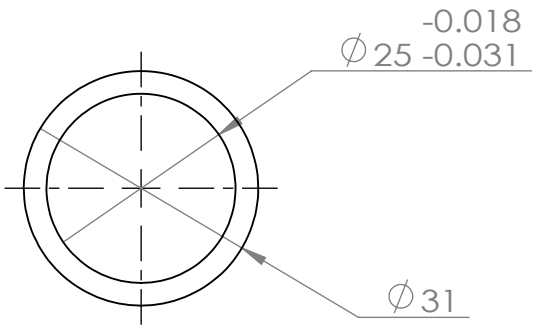

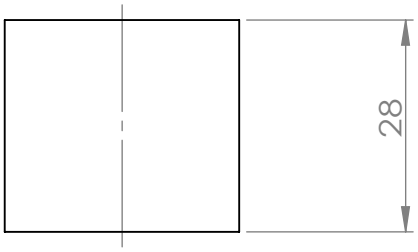

UNLESS OTHERWISE SPECIFIED: DIMENSIONS ARE IN MILLIMETERS SURFACE FINISH: Ra=25 TOLERANCES: MEDIUM LINEAR: ANGULAR:	FINISH:		DEBUR AND BREAK SHARP EDGES		DO NOT SCALE DRAWING	REVISION
	NAME	SIGNATURE	DATE		TITLE:	
DRAWN	YUNSHI ZHAO				SPACER1	
CHK'D						
APPV'D						
MFG						
Q.A				MATERIAL: STEEL	DWG NO. 4	A4
				WEIGHT:	SCALE:1:1	SHEET 1 OF 1

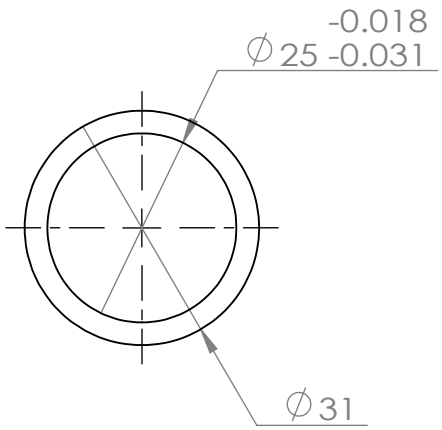

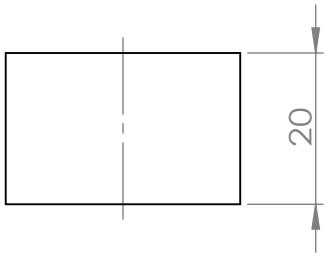

UNLESS OTHERWISE SPECIFIED: DIMENSIONS ARE IN MILLIMETERS SURFACE FINISH: TOLERANCES: LINEAR: ANGULAR:	FINISH:		DEBUR AND BREAK SHARP EDGES	DO NOT SCALE DRAWING	REVISION	
	NAME	SIGNATURE	DATE	TITLE:		
DRAWN	YUNSHI ZHAO			SPACER2		
CHK'D						
APPV'D						
MFG						
Q.A				MATERIAL:	DWG NO.	A4
				STEEL	5	
				WEIGHT:	SCALE:1:1	SHEET 1 OF 1

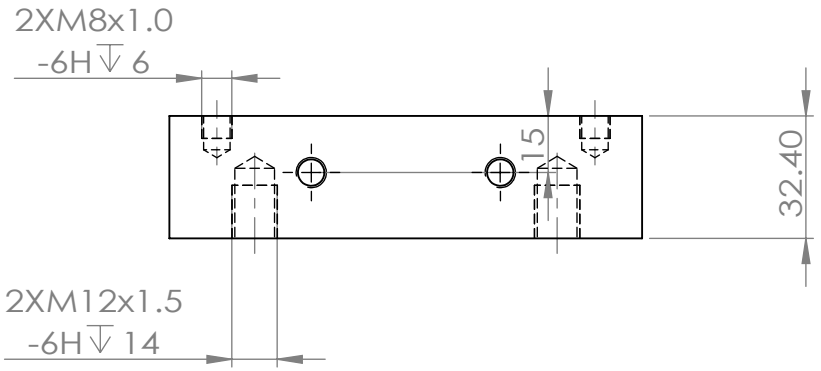

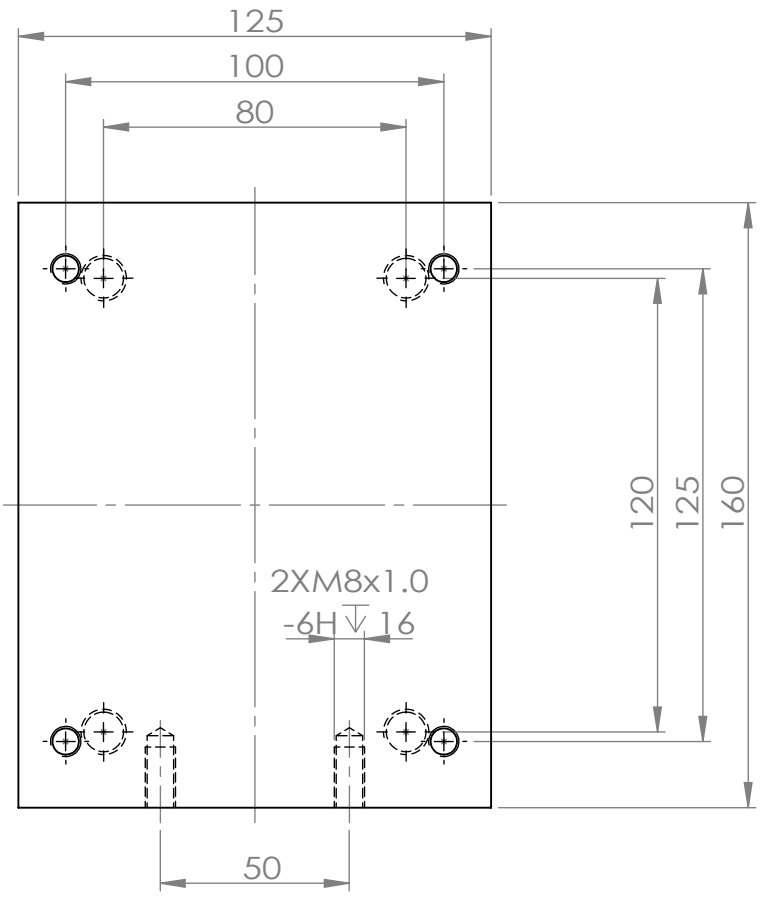

UNLESS OTHERWISE SPECIFIED: DIMENSIONS ARE IN MILLIMETERS SURFACE FINISH: Ra=25 TOLERANCES: MEDIUM LINEAR: ANGULAR:	FINISH:		DEBUR AND BREAK SHARP EDGES	DO NOT SCALE DRAWING	REVISION	
	NAME	SIGNATURE	DATE	TITLE:		
DRAWN	YUNSHI ZHAO			MOTOR BASE		
CHK'D						
APPV'D						
MFG						
Q.A				MATERIAL: STEEL	DWG NO. 6	A4
				WEIGHT:	SCALE:1:2	SHEET 1 OF 1

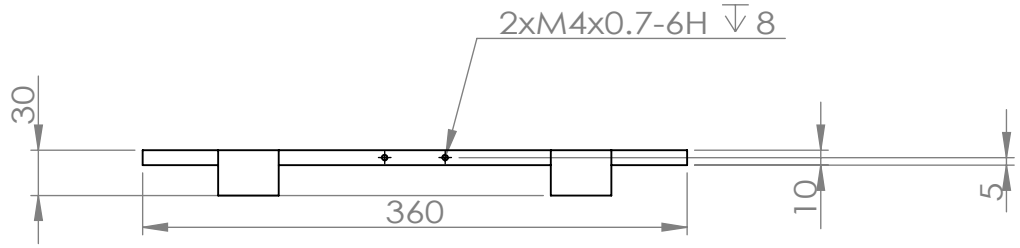

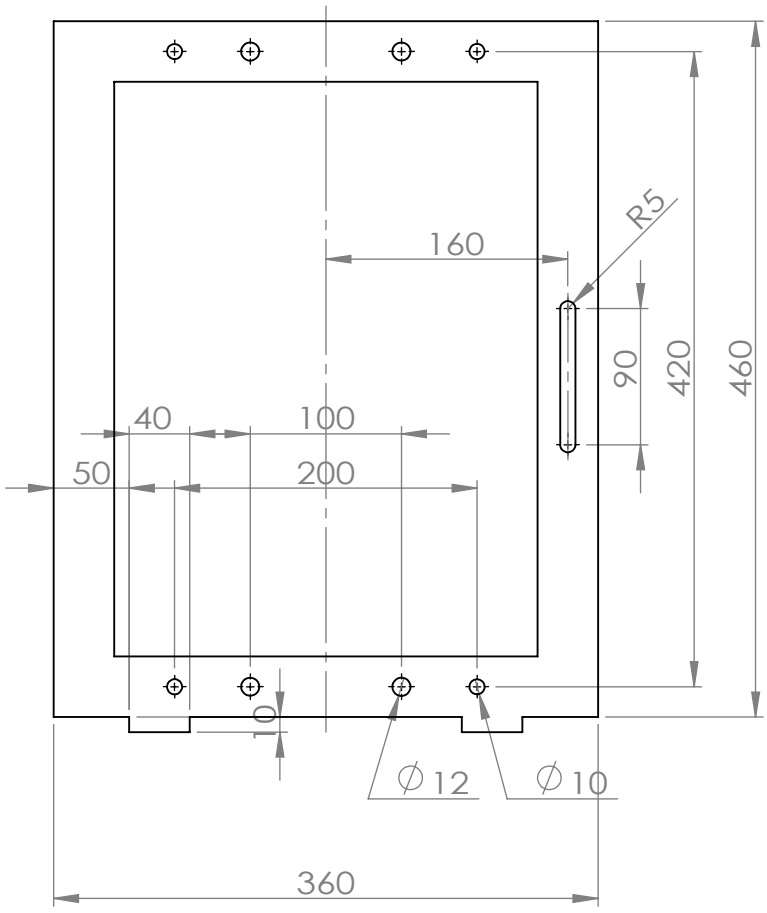

UNLESS OTHERWISE SPECIFIED: DIMENSIONS ARE IN MILLIMETERS SURFACE FINISH: Ra=25 TOLERANCES: MEDIUM LINEAR: ANGULAR:		FINISH:		DEBUR AND BREAK SHARP EDGES	DO NOT SCALE DRAWING	REVISION
	NAME	SIGNATURE	DATE		TITLE:	
DRAWN	YUNSHI ZHAO				ANTI-PITCH FRAME	
CHK'D						
APPV'D						
MFG						
Q.A				MATERIAL: STEEL	DWG NO. 7	A4
				WEIGHT:	SCALE:1:5	SHEET 1 OF 1

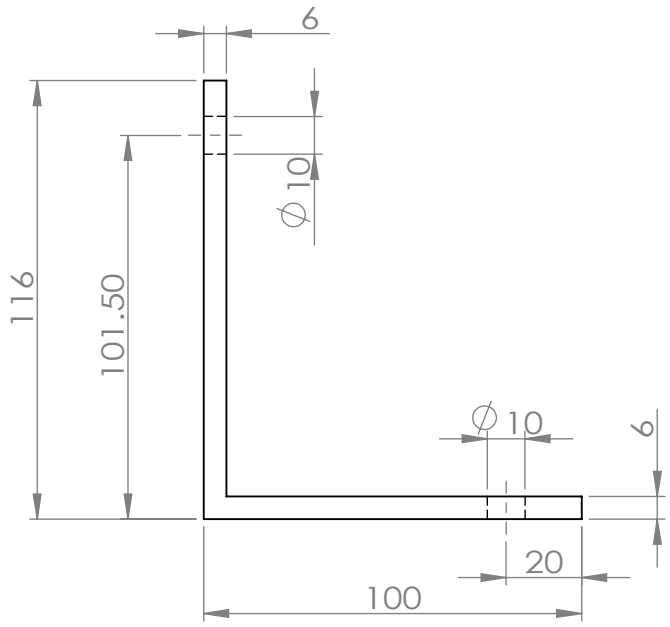

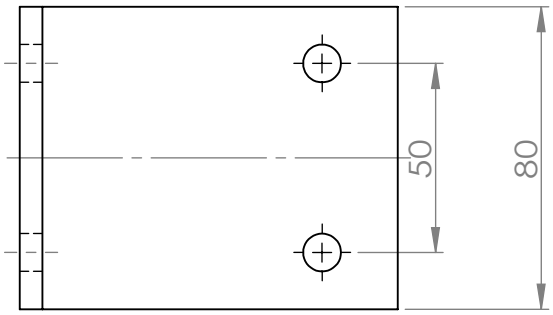

UNLESS OTHERWISE SPECIFIED: DIMENSIONS ARE IN MILLIMETERS SURFACE FINISH: Ra=25 TOLERANCES: MEDIUM LINEAR: ANGULAR:	FINISH:		DEBUR AND BREAK SHARP EDGES		DO NOT SCALE DRAWING	REVISION
	NAME	SIGNATURE	DATE		TITLE:	
DRAWN	YUNSHI ZHAO				ANTI-PITCH ARM	
CHK'D						
APPV'D						
MFG						
Q.A				MATERIAL: STEEL	DWG NO. 8	A4
				WEIGHT:	SCALE:1:2	SHEET 1 OF 1

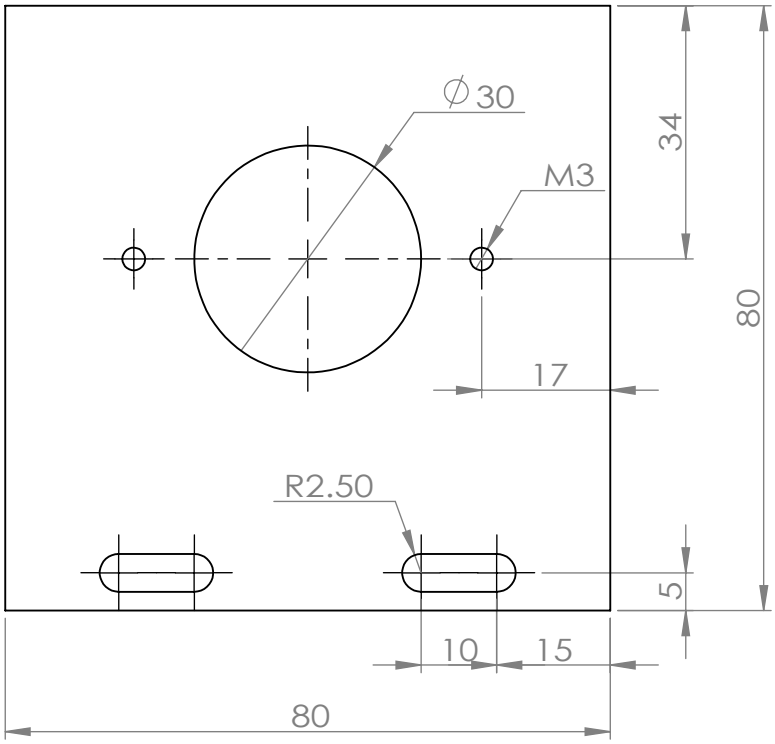

THICKNEES 6MM
ALL HOLES ARE THROUGH HOLES

UNLESS OTHERWISE SPECIFIED: DIMENSIONS ARE IN MILLIMETERS SURFACE FINISH: TOLERANCES: LINEAR: ANGULAR:	FINISH:		DEBUR AND BREAK SHARP EDGES	DO NOT SCALE DRAWING	REVISION	
	NAME	SIGNATURE	DATE	TITLE:		
DRAWN	YUNSHI ZHAO			ENCODER HOLDER 1		
CHK'D						
APPV'D						
MFG						
Q.A				MATERIAL: STEEL	DWG NO. 9	A4
				WEIGHT:	SCALE:1:1	SHEET 1 OF 1

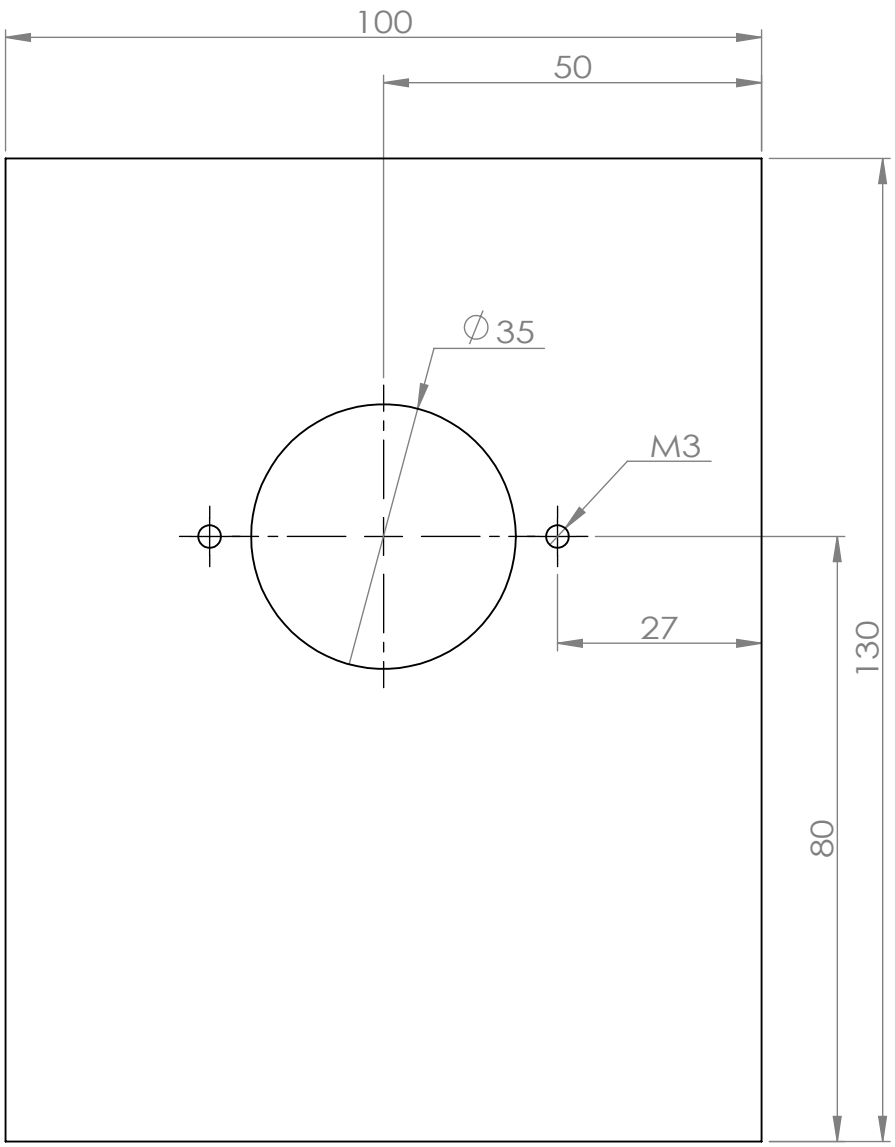

Thickness 6mm
All the holes are through holes

UNLESS OTHERWISE SPECIFIED: DIMENSIONS ARE IN MILLIMETERS SURFACE FINISH: TOLERANCES: LINEAR: ANGULAR:	FINISH:		DEBUR AND BREAK SHARP EDGES	DO NOT SCALE DRAWING	REVISION	
	NAME	SIGNATURE	DATE	TITLE:		
DRAWN	YUNSHI ZHAO			ENCODER HOLDER 2		
CHK'D						
APPV'D						
MFG						
Q.A				MATERIAL: STEEL	DWG NO. 10	A4
				WEIGHT:	SCALE:1:1	SHEET 1 OF 1

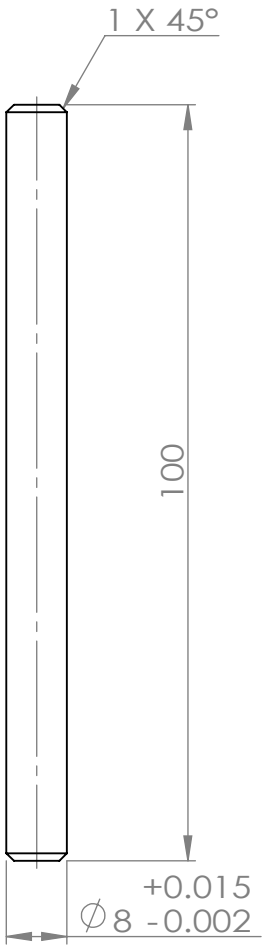

UNLESS OTHERWISE SPECIFIED: DIMENSIONS ARE IN MILLIMETERS SURFACE FINISH: Ra=25 TOLERANCES: MEDIUM LINEAR: ANGULAR:	FINISH:		DEBUR AND BREAK SHARP EDGES		DO NOT SCALE DRAWING	REVISION
	NAME	SIGNATURE	DATE		TITLE:	
DRAWN	YUNSHI ZHAO				ENCODER SHAFT	
CHK'D						
APPV'D						
MFG						
Q.A				MATERIAL: STEEL	DWG NO. 11	A4
				WEIGHT:	SCALE:1:1	SHEET 1 OF 1

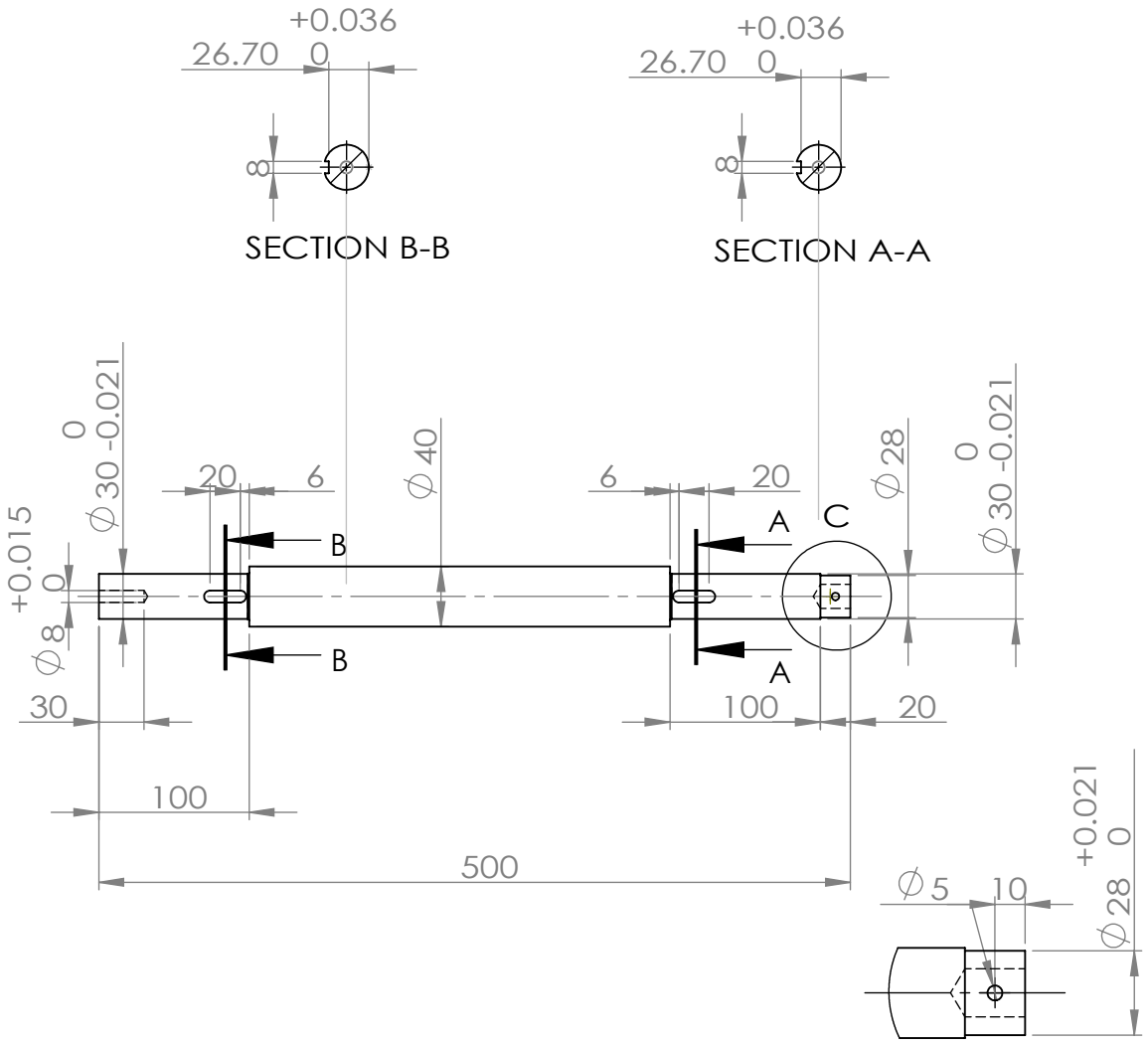

DETAIL C
SCALE 2 : 5

Unspecified Fillet C=1mm
Unspecified Chamfer R=1mm

UNLESS OTHERWISE SPECIFIED: DIMENSIONS ARE IN MILLIMETERS SURFACE FINISH: TOLERANCES: LINEAR: ANGULAR:	FINISH:		DEBUR AND BREAK SHARP EDGES	DO NOT SCALE DRAWING	REVISION	
	NAME	SIGNATURE	DATE	TITLE:		
DRAWN	YUNSHI ZHAO			ROLLER AXLE		
CHK'D						
APPV'D						
MFG						
Q.A				MATERIAL: STEEL	DWG NO. 12	A4
				WEIGHT:	SCALE:1:5	SHEET 1 OF 1

TABLE 1		
CO-ORDINATES A-H		
POINTS	X	Z
O	0	0
A	-7	-6.75
B	-6.985	-2.786
C	-5.027	-0.440
D	-1.905	-0.030
E	1.905	-0.030
F	5.027	-0.440
G	6.985	-2.786
H	7	-6.75

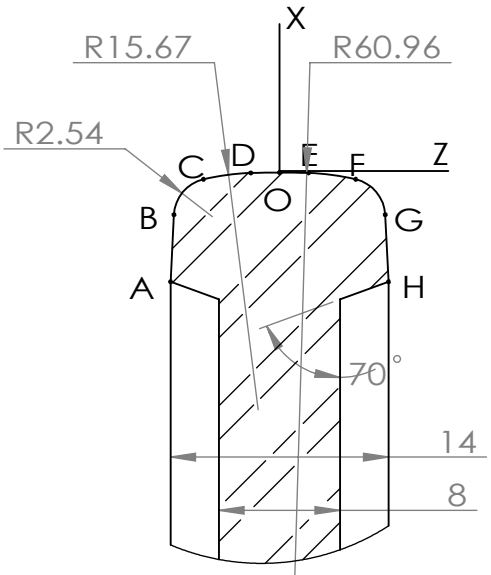

DETAIL B
SCALE 2 : 1

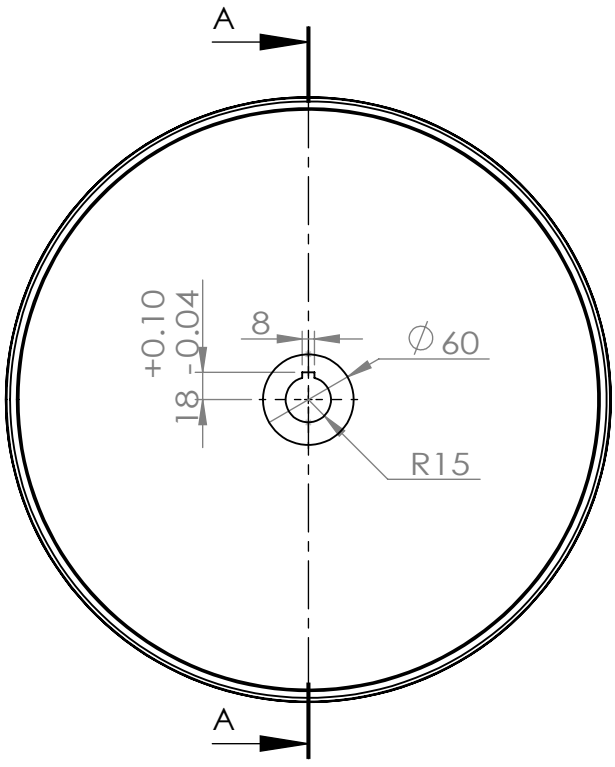

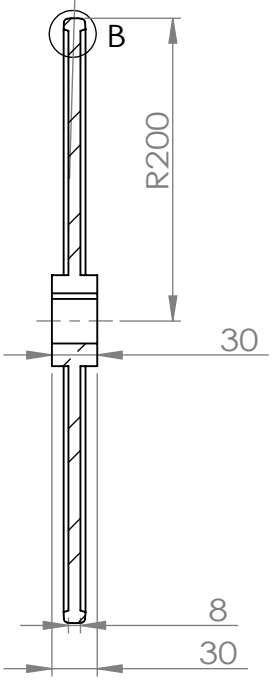

SECTION A-A

UNLESS OTHERWISE SPECIFIED: DIMENSIONS ARE IN MILLIMETERS SURFACE FINISH: TOLERANCES: LINEAR: ANGULAR:	FINISH:		DEBUR AND BREAK SHARP EDGES	DO NOT SCALE DRAWING	REVISION	
	NAME	SIGNATURE	DATE	TITLE:		
DRAWN	YUNSHI ZHAO			ROLLER		
CHK'D						
APPV'D						
MFG						
				MATERIAL: STEEL	DWG NO. 13	A4
				WEIGHT:	SCALE:1:5	SHEET 1 OF 1

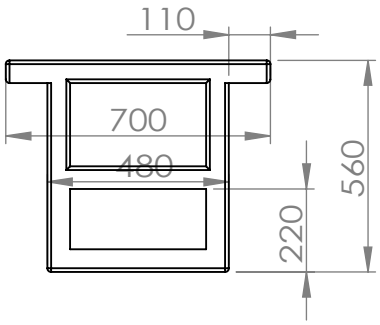

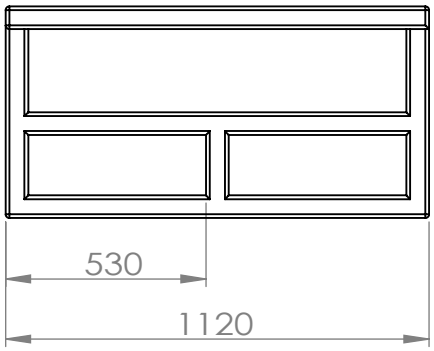

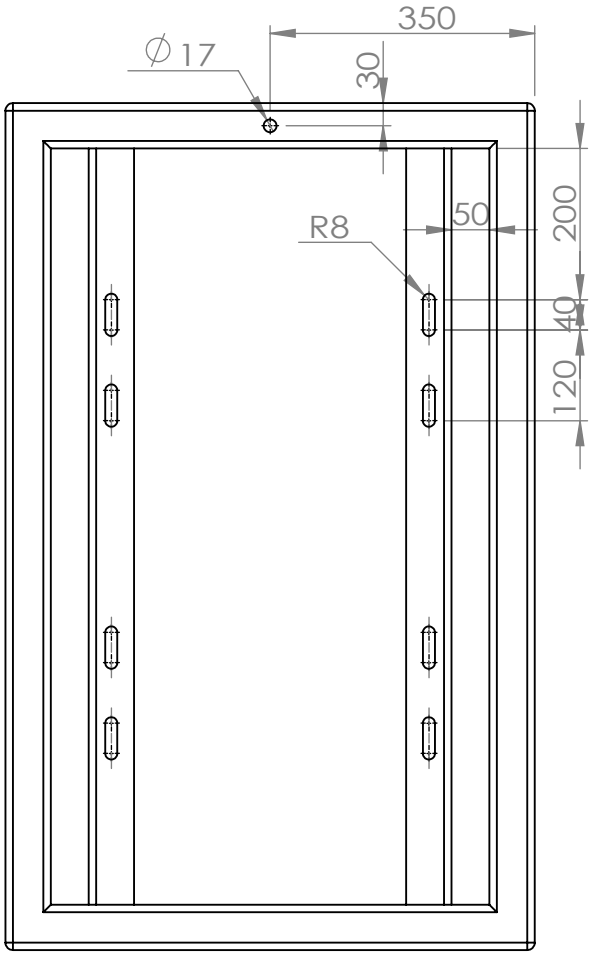

SCALE 1:10

WELDED FROM BOX SECTION OF 60X60X3.6mm

UNLESS OTHERWISE SPECIFIED: DIMENSIONS ARE IN MILLIMETERS SURFACE FINISH: TOLERANCES: LINEAR: ANGULAR:	FINISH:		DEBUR AND BREAK SHARP EDGES	DO NOT SCALE DRAWING	REVISION	
	NAME	SIGNATURE	DATE	TITLE:		
DRAWN	YUNSHI ZHAO			GROUND FRAME		
CHK'D						
APPV'D						
MFG						
				MATERIAL: STEEL	DWG NO. 14	A4
				WEIGHT:	SCALE:1:20	SHEET 1 OF 1

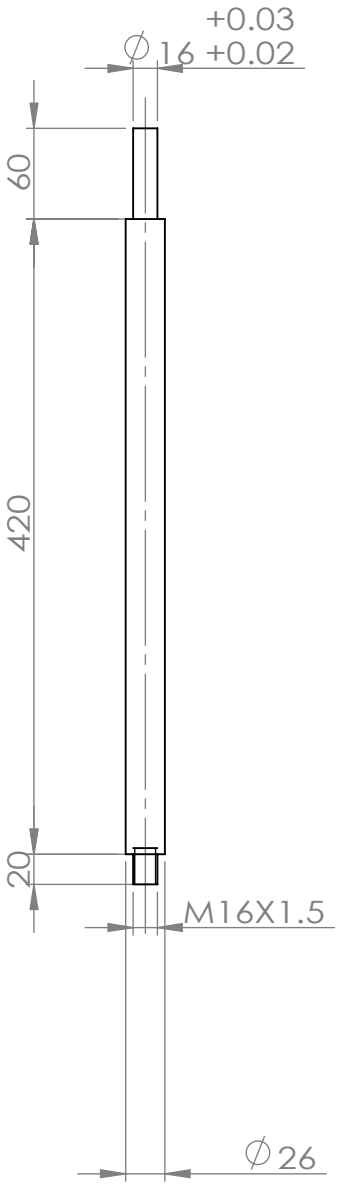

UNLESS OTHERWISE SPECIFIED: DIMENSIONS ARE IN MILLIMETERS SURFACE FINISH: TOLERANCES: LINEAR: ANGULAR:	FINISH:		DEBUR AND BREAK SHARP EDGES	DO NOT SCALE DRAWING	REVISION	
	NAME	SIGNATURE	DATE	TITLE:		
DRAWN	YUNSHI ZHAO			BOGIE ARM 1		
CHK'D						
APPV'D						
MFG						
				MATERIAL: STEEL	DWG NO. 15	A4
				WEIGHT:	SCALE:1:5	SHEET 1 OF 1

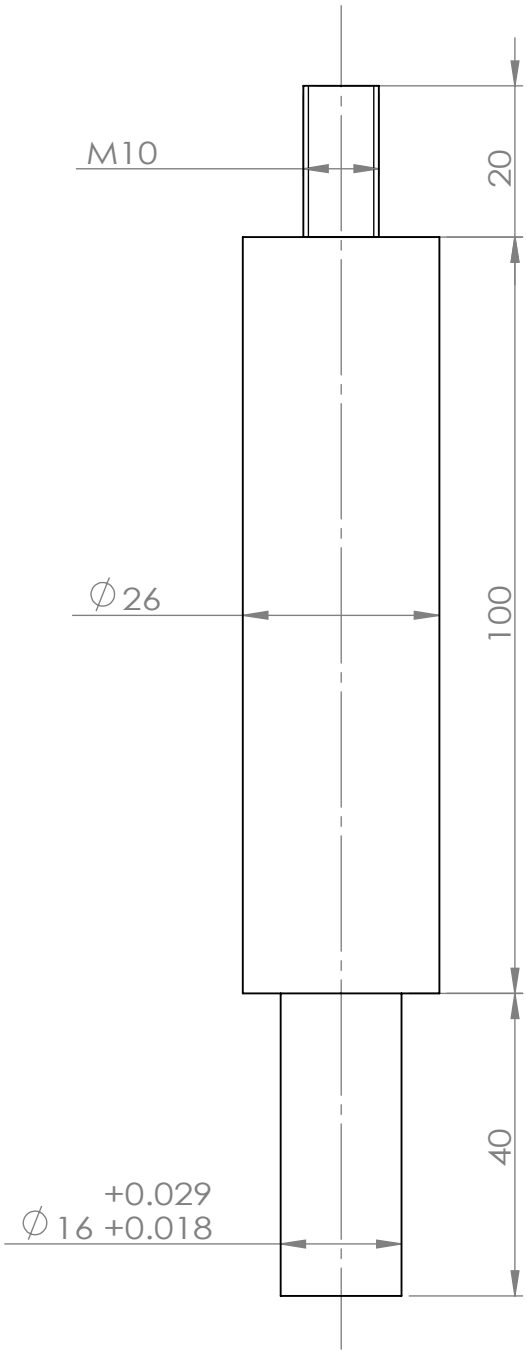

UNLESS OTHERWISE SPECIFIED: DIMENSIONS ARE IN MILLIMETERS SURFACE FINISH: TOLERANCES: LINEAR: ANGULAR:	FINISH:		DEBUR AND BREAK SHARP EDGES	DO NOT SCALE DRAWING	REVISION	
	NAME	SIGNATURE	DATE	TITLE:		
DRAWN	YUNSHI ZHAO			BOGIE ARM 2		
CHK'D						
APPV'D						
MFG						
				MATERIAL: STEEL	DWG NO. 16	A4
				WEIGHT:	SCALE:1:1	SHEET 1 OF 1

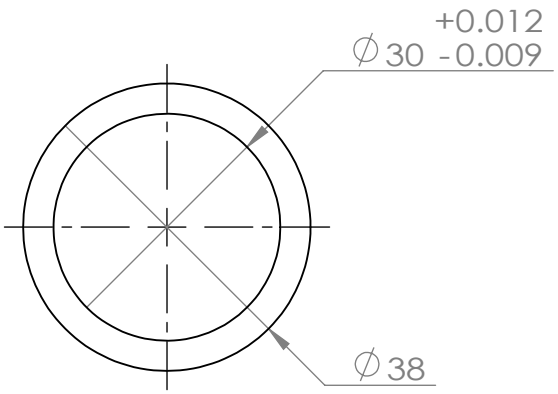

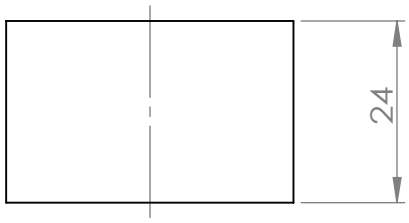

UNLESS OTHERWISE SPECIFIED: DIMENSIONS ARE IN MILLIMETERS SURFACE FINISH: TOLERANCES: LINEAR: ANGULAR:	FINISH:		DEBUR AND BREAK SHARP EDGES	DO NOT SCALE DRAWING	REVISION	
	NAME	SIGNATURE	DATE	TITLE:		
DRAWN	YUNSHI ZHAO			SPACER 3		
CHK'D						
APPV'D						
MFG						
Q.A				MATERIAL: STEEL	DWG NO. 17	A4
				WEIGHT:	SCALE:1:1	SHEET 1 OF 1

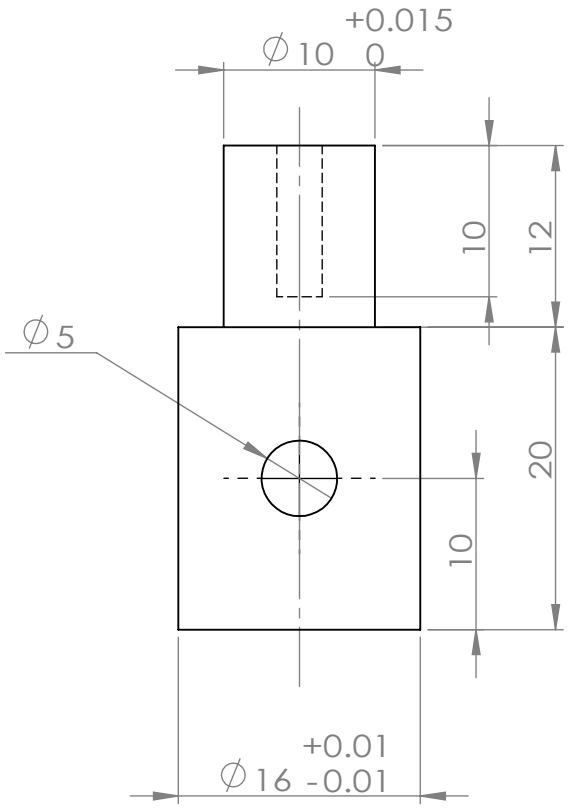

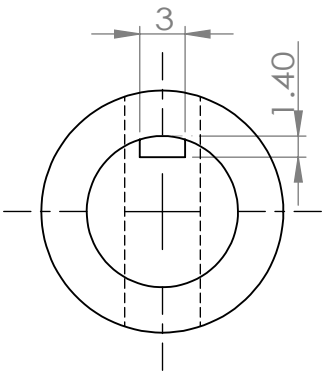

UNLESS OTHERWISE SPECIFIED: DIMENSIONS ARE IN MILLIMETERS SURFACE FINISH: TOLERANCES: LINEAR: ANGULAR:	FINISH:		DEBUR AND BREAK SHARP EDGES	DO NOT SCALE DRAWING	REVISION	
	NAME	SIGNATURE	DATE	TITLE:		
DRAWN	YUNSHI ZHAO			AXLE EXTENSION		
CHK'D						
APPV'D						
MFG						
				DWG NO. 18		A4
				MATERIAL: STEEL		
				WEIGHT:	SCALE:2:1	SHEET 1 OF 1

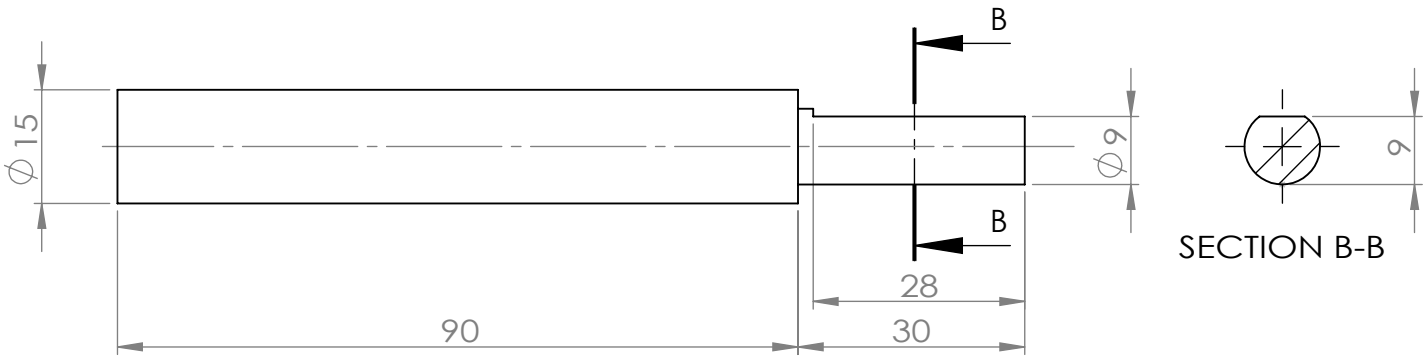

UNLESS OTHERWISE SPECIFIED: DIMENSIONS ARE IN MILLIMETERS SURFACE FINISH: TOLERANCES: LINEAR: ANGULAR:	FINISH:		DEBUR AND BREAK SHARP EDGES	DO NOT SCALE DRAWING	REVISION	
	NAME	SIGNATURE	DATE	TITLE:		
DRAWN	YUNSHI ZHAO			PULLEY SHAFT 1		
CHK'D						
APPV'D						
MFG						
Q.A				MATERIAL: STEEL	DWG NO. 19	A4
				WEIGHT:	SCALE:1:1	SHEET 1 OF 1

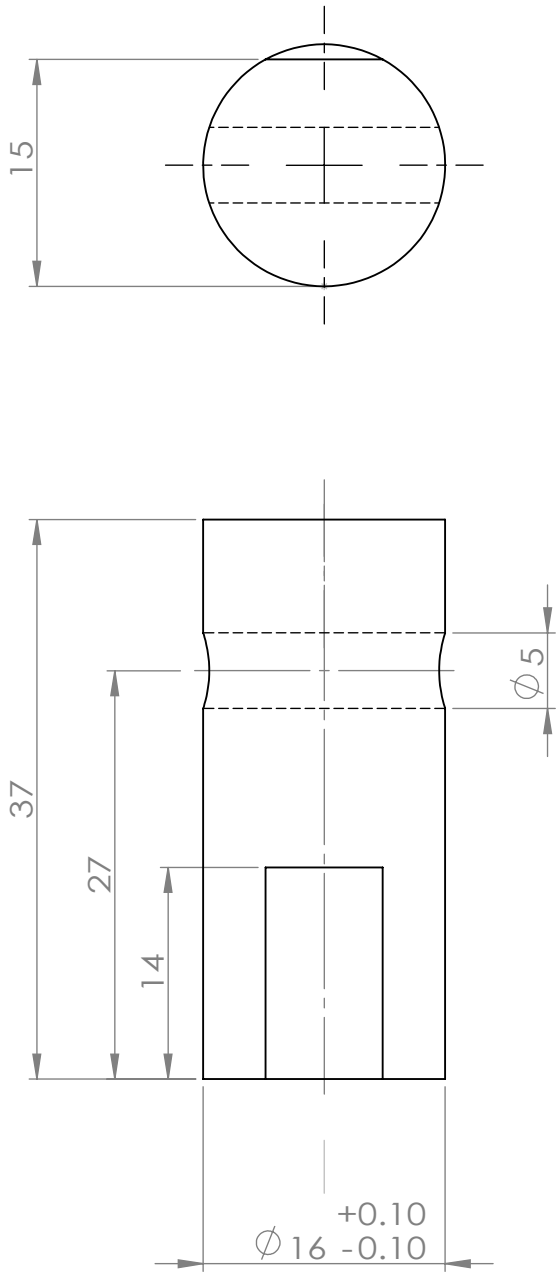

UNLESS OTHERWISE SPECIFIED: DIMENSIONS ARE IN MILLIMETERS SURFACE FINISH: TOLERANCES: LINEAR: ANGULAR:	FINISH:		DEBUR AND BREAK SHARP EDGES	DO NOT SCALE DRAWING	REVISION	
	NAME	SIGNATURE	DATE	TITLE:		
DRAWN	YUNSHI ZHAO			PULLEY SHAFT 2		
CHK'D						
APPV'D						
MFG						
Q.A				MATERIAL: STEEL	DWG NO. 20	A4
				WEIGHT:	SCALE:2:1	SHEET 1 OF 1

Appendix C

Block diagrams of the motor control system

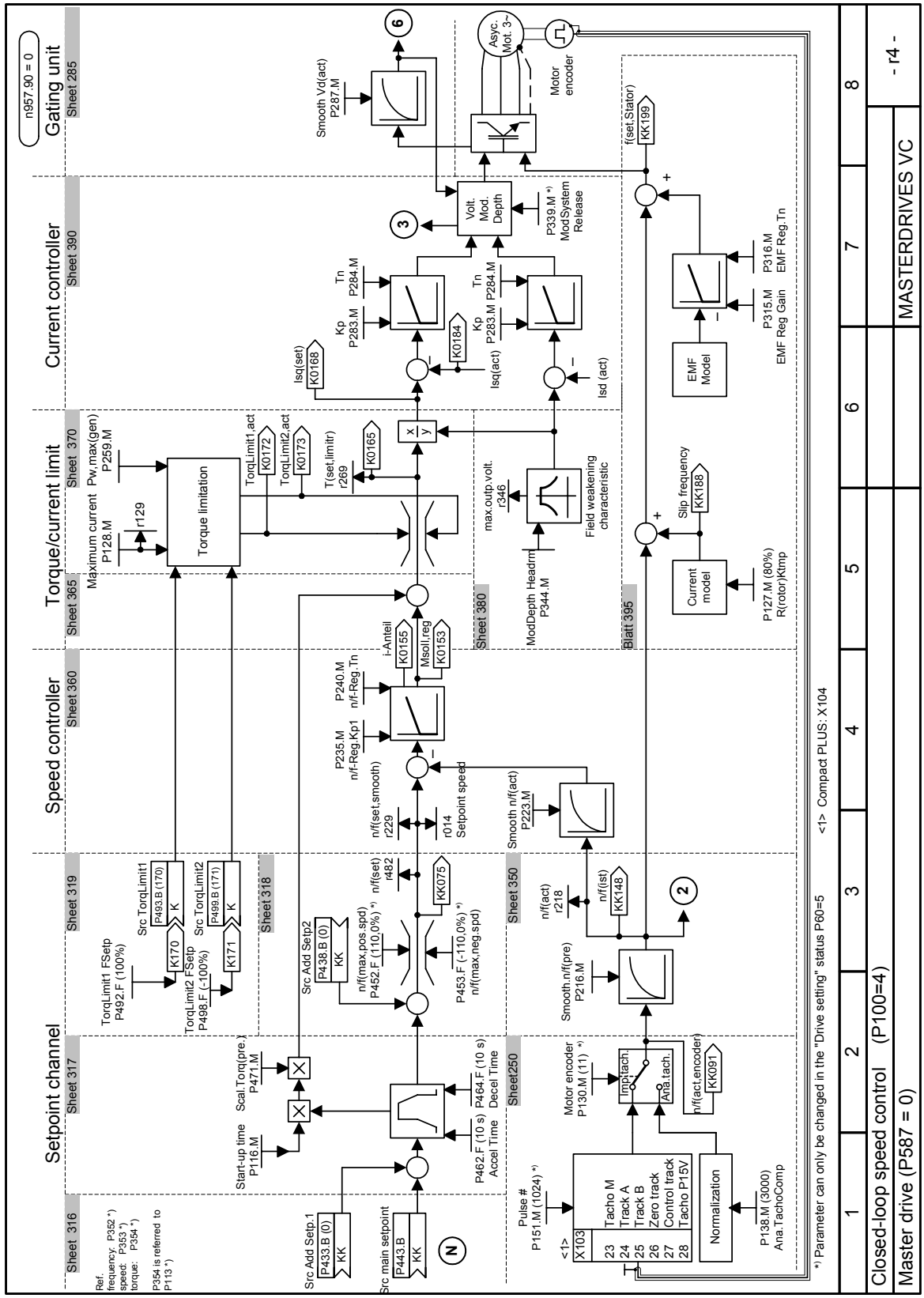
n957.90 = 0
Gating unit
Sheet 285
Current controller
Sheet 390
Torque/current limit
Sheet 370
Sheet 365
Speed controller
Sheet 360
Sheet 319
Sheet 318
Setpoint channel
Sheet 317
Sheet 316
Sheet 380
Sheet 350
Sheet250
Blatt 395
Smooth Vd(act) P287.M
Asyc. Mot. 3~
Motor encoder
Volt. Mod. Depth
P339.M *) ModSystem Release
f(set.Stator) KK199
Tn P284.M
Kp P283.M
K0184
Isq(act)
Isq(set) K0168
Isd (act)
EMF Model
P316.M EMF Reg.Tn
P315.M EMF Reg Gain
Maximum current P128.M
r129
Pw.max(gen) P259.M
Torque limitation
TorqLimit1.act K0172
TorqLimit2.act K0173
T(set,limitr) r269
K0165
max.outp.volt. r346
ModDepth Headrm P344.M
Field weakening characteristic
Slip frequency KK188
Current model
P127.M (80%) R(rotor)Ktmp
i-Anteil K0155
Msoll.reg K0153
P240.M n/f-Reg.Tn
P235.M n/f-Reg.Kp1
n/f(set,smooth) r229
r014 Setpoint speed
Smooth n/f(act) P223.M
n/f(act) r218
n/f(ist) KK148
n/f(set) r482
KK075
n/f(max,pos.spd) P452.F (110,0%) *)
P453.F (-110,0%) *) n/f(max.neg.spd)
TorqLimit1 FSetp P492.F (100%)
TorqLimit2 FSetp P498.F (-100%)
Src TorqLimit1 P493.B (170)
Src TorqLimit2 P499.B (171)
K170
K171
K
Src Add Setp2 P438.B (0) KK
Scal.Torq(pre.) P471.M
Start-up time P116.M
P462.F (10 s) Accel Time
P464.F (10 s) Decel Time
Src Add Setp.1 P433.B (0) KK
Src main setpoint P443.B KK
Ref. frequency: P352 *) speed: P353 *) torque: P354 *)
P354 is referred to P113 *)
Smooth.n/f(pre) P216.M
Motor encoder P130.M (11) *)
Impl.tach.
Ana.tach.
n/f(act,encoder) KK091
Pulse # P151.M (1024) *)
<1> X103
23 Tacho M
24 Track A
25 Track B
26 Zero track
27 Control track
28 Tacho P15V
Normalization
P138.M (3000) Ana.TachoComp
*) Parameter can only be changed in the "Drive setting" status P60=5
<1> Compact PLUS: X104
1 2 3 4 5 6 7 8
Closed-loop speed control (P100=4)
Master drive (P587 = 0)
MASTERDRIVES VC
- r4 -

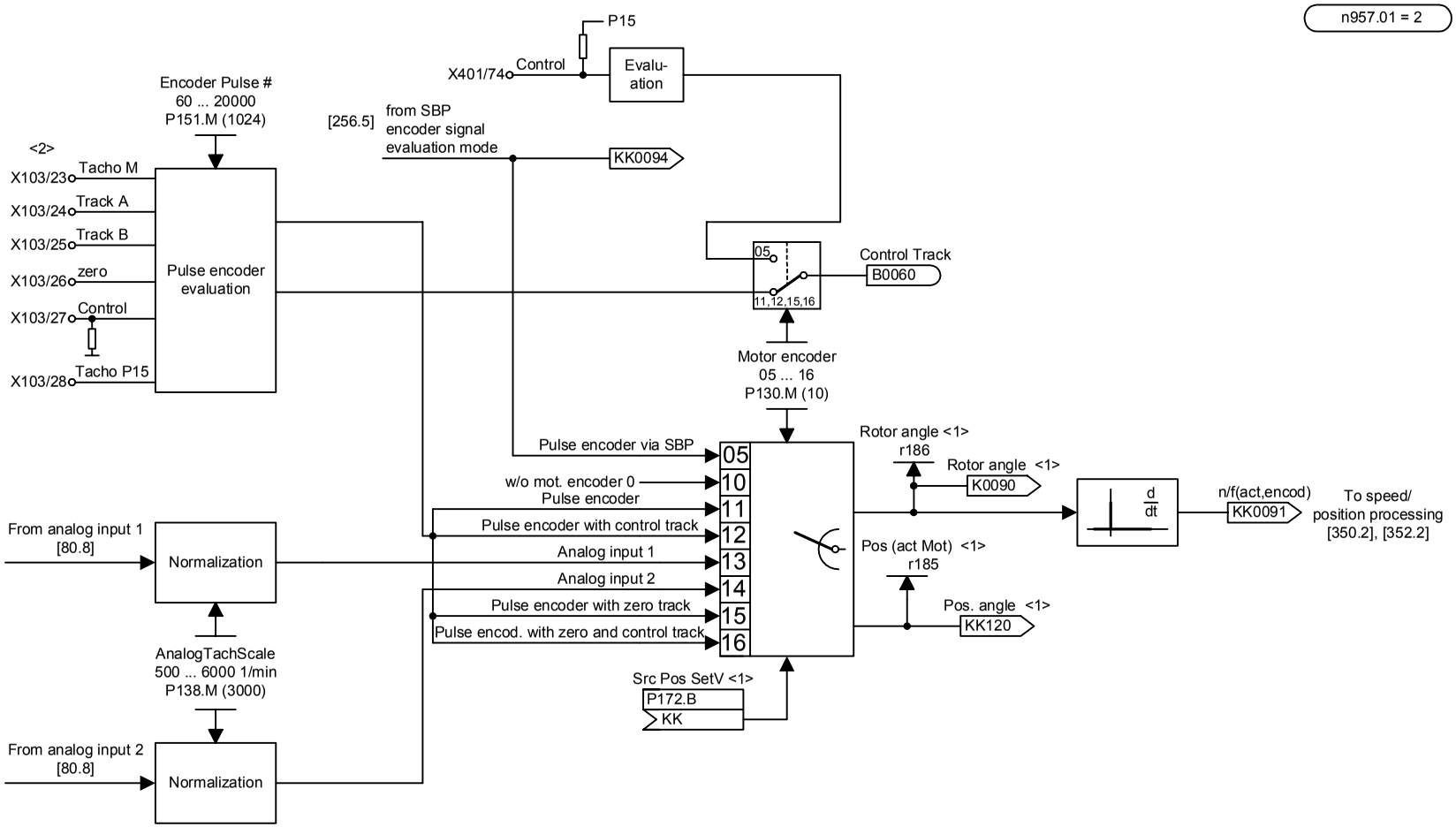

1	2	3	4	5	6	7	8
Encoder evaluation					fp_vc_250_e.vsd	Function diagram	- 250 -
Speed/position processing					21.07.04	MASTERDRIVES VC	

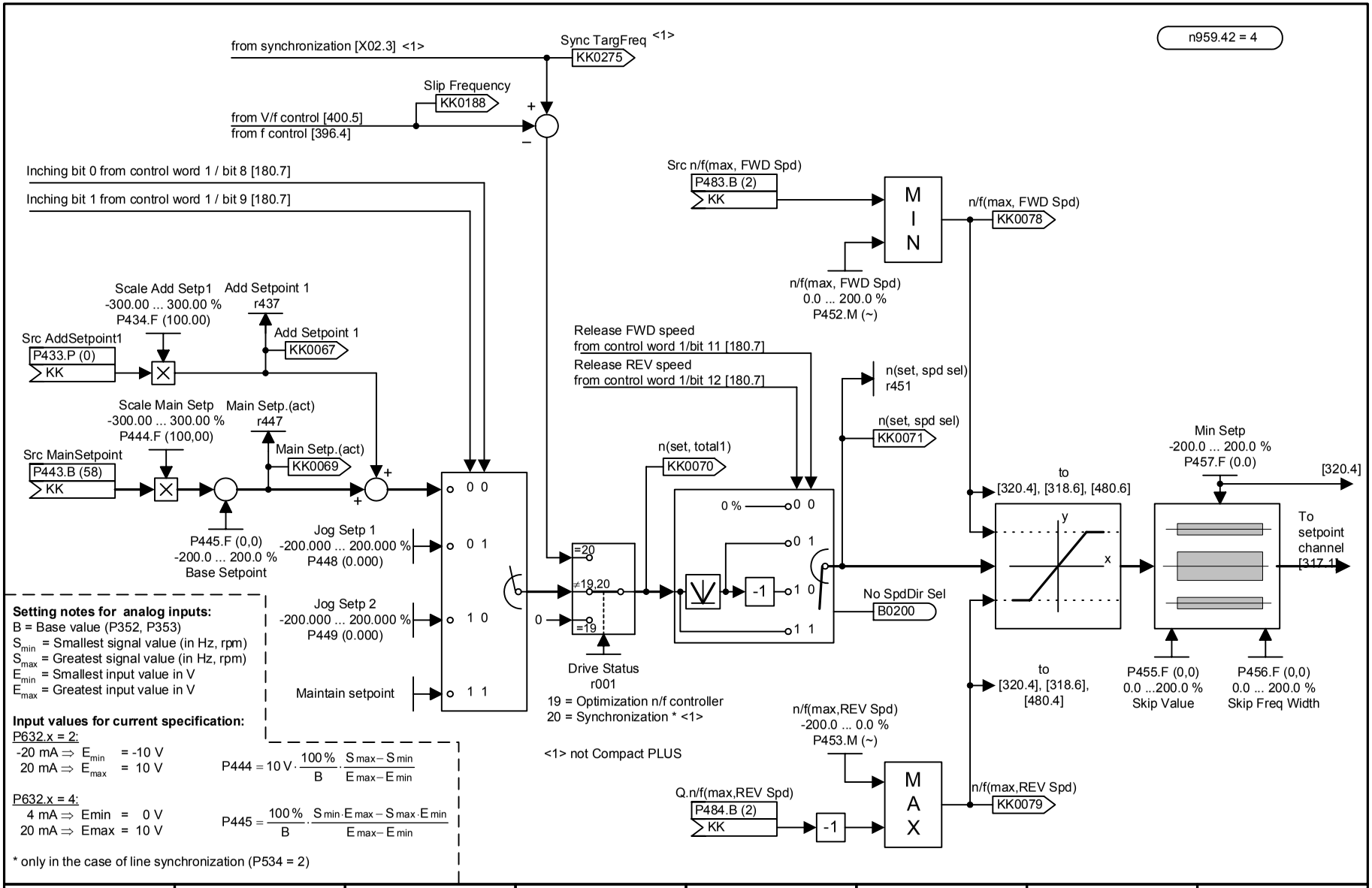

1	2	3	4	5	6	7	8
Setpoint channel (part 1)					fp_vc_316_e.vsd	Function diagram	- 316 -
Master Drive					24.07.01	MASTERDRIVES VC	

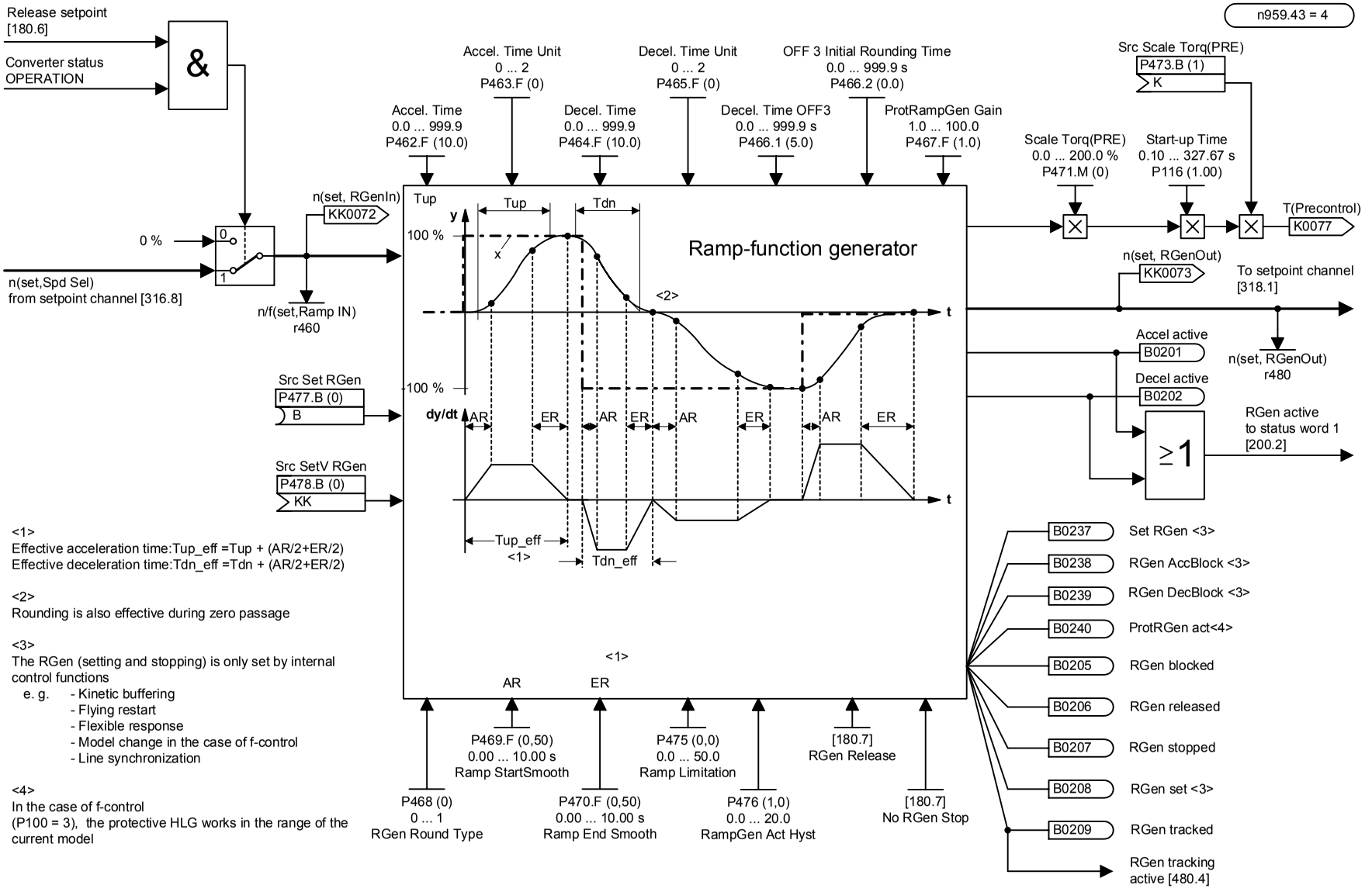

1	2	3	4	5	6	7	8
Setpoint channel (Part 2)					fp_vc_317_e.vsd	Function diagram	- 317 -
Master drive + RFG					12.05.03	MASTERDRIVES VC	

n959.44 = 3

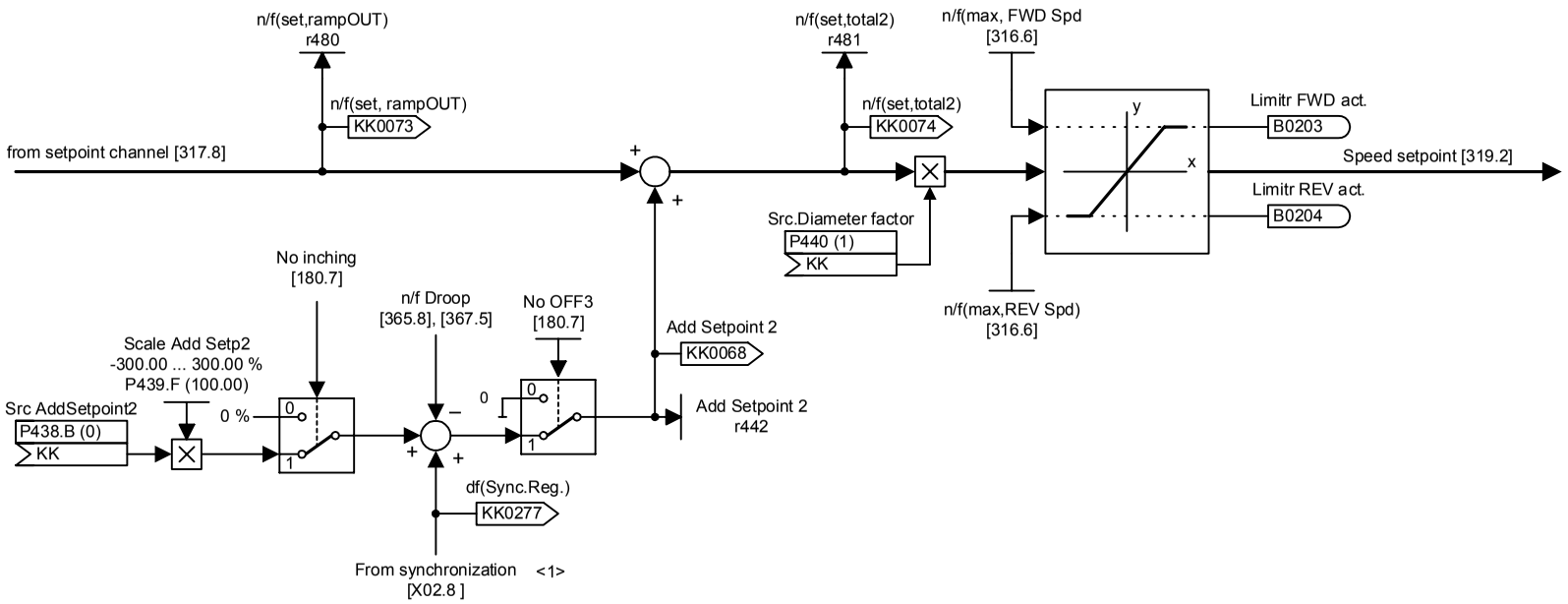

<1> not Compact PLUS

1	2	3	4	5	6	7	8
Setpoint channel (part 3)					fp_vc_318_e.vsd	Function diagram	- 318 -
Master drive					21.07.04	MASTERDRIVES VC	

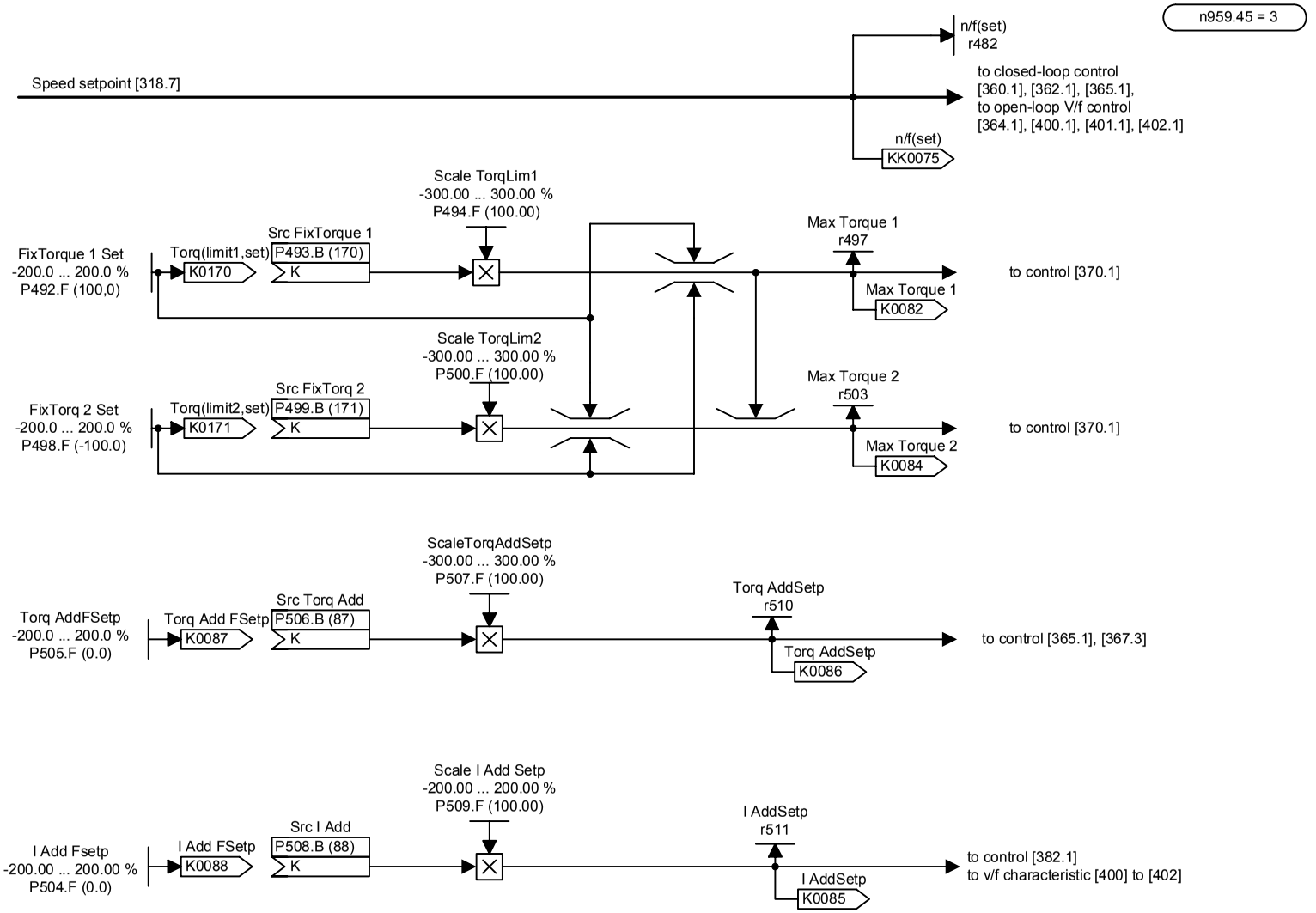

1	2	3	4	5	6	7	8
Setpoint channel (part 4)					fp_vc_319_e.vsd	Function diagram	- 319 -
Master drive					31.01.98	MASTERDRIVES VC	

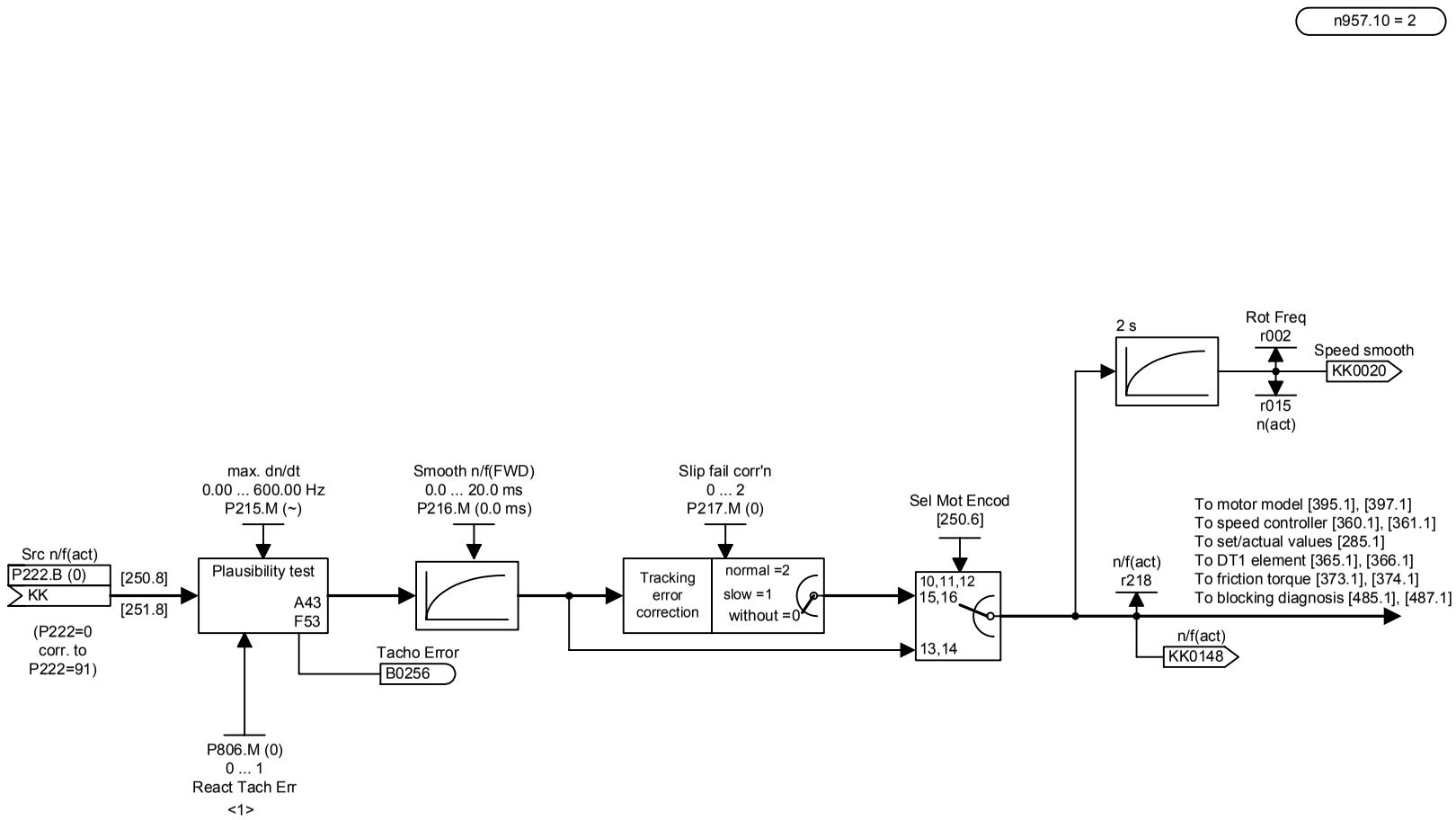

<1> Only in the case of n-control (P100 = 4)
Not in the case of synch. motor (P95=12)

1	2	3	4	5	6	7	8
Speed/position processing					fp_vc_350_e.vsd	Function diagram	- 350 -
Speed/torque control, master/slave drive					31.01.98	MASTERDRIVES VC	

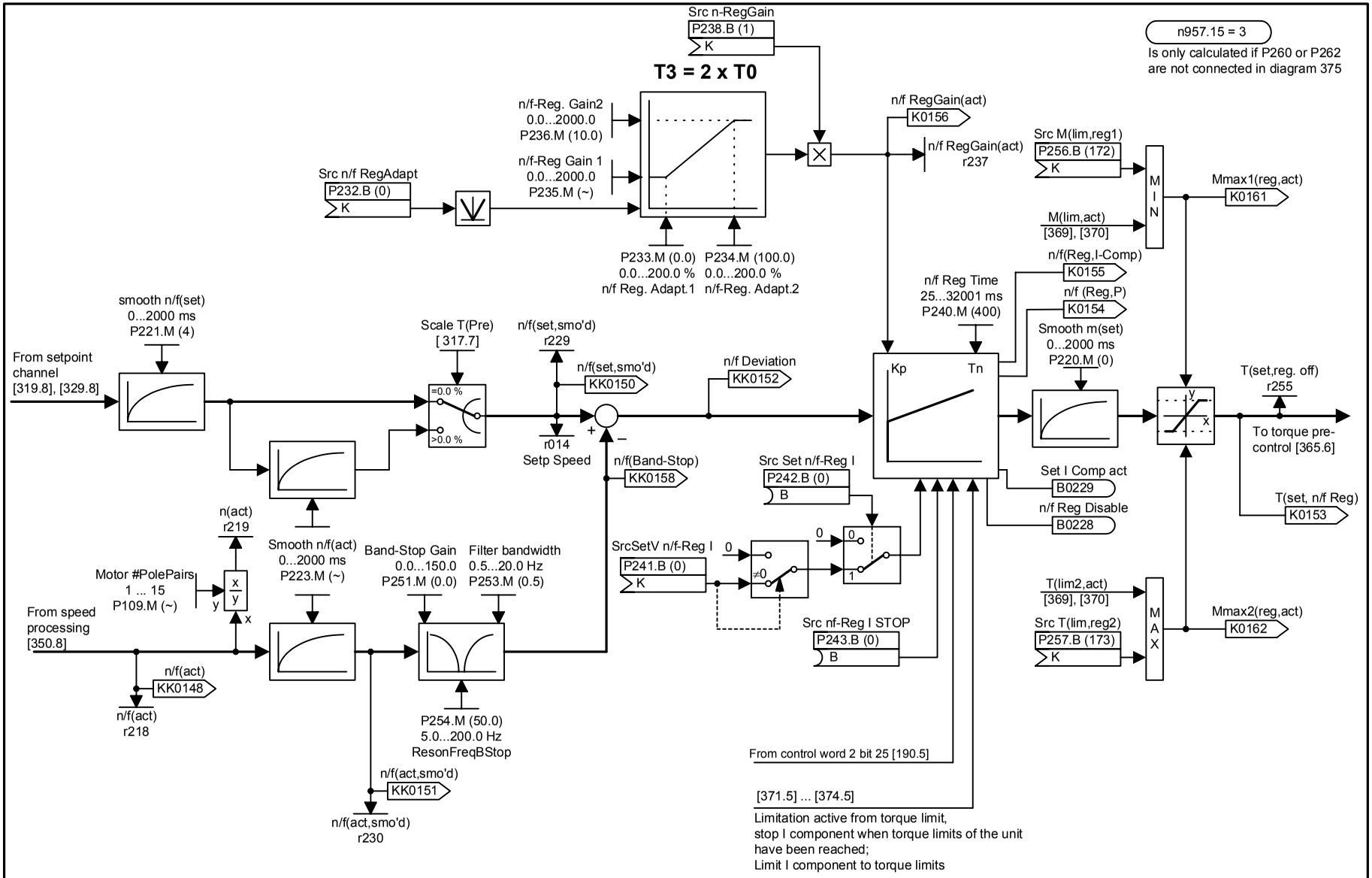

1	2	3	4	5	6	7	8
Speed controller					fp_vc_360_e.vsd	Function diagram	- 360 -
Speed control, master drive					21.07.04	MASTERDRIVES VC	

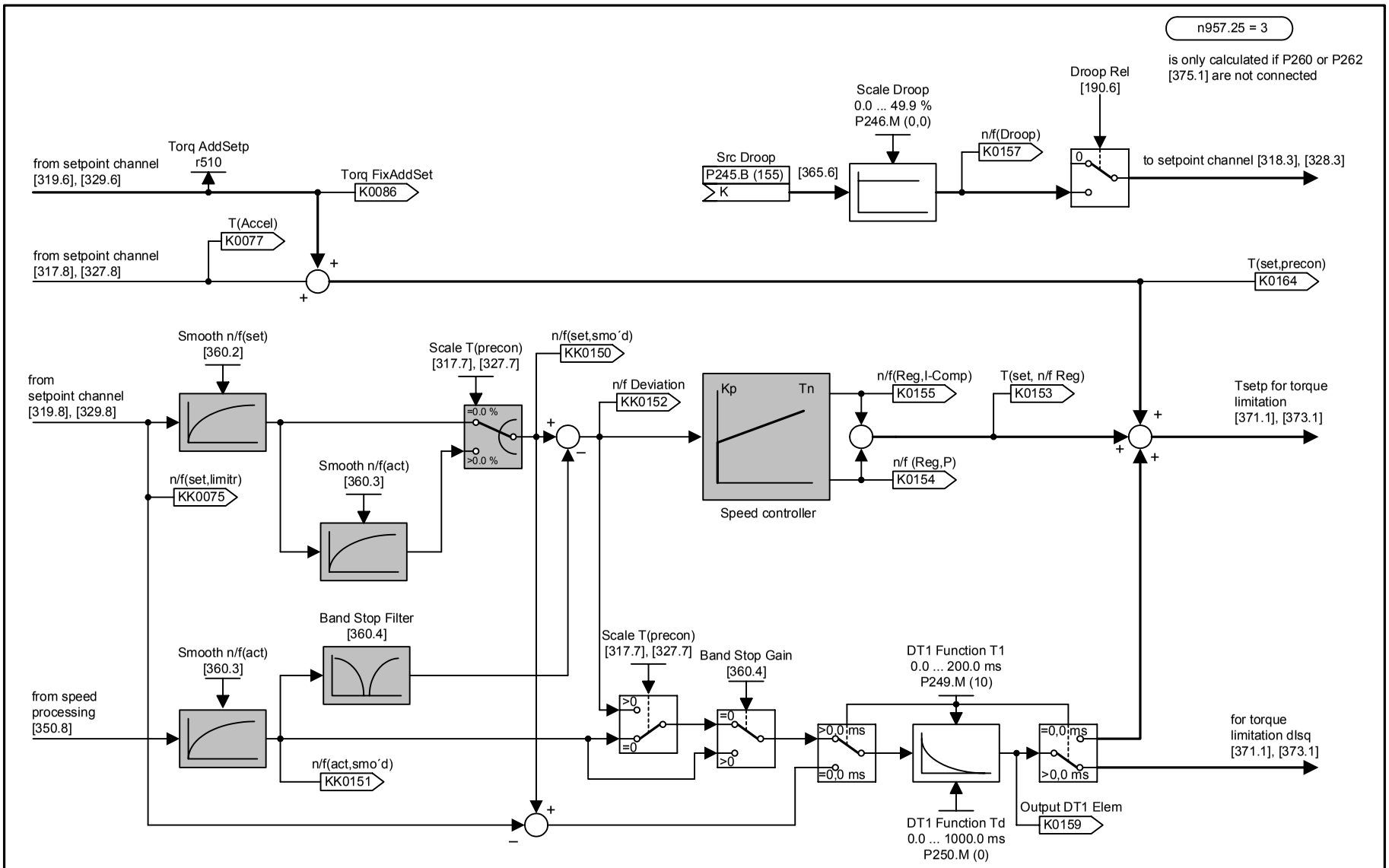

1	2	3	4	5	6	7	8
DT1 element, droop and torque pre-control					fp_vc_365_e.vsd	Function diagram	- 365 -
Speed control, master drive					09.04.98	MASTERDRIVES VC	

n957.30 = 3

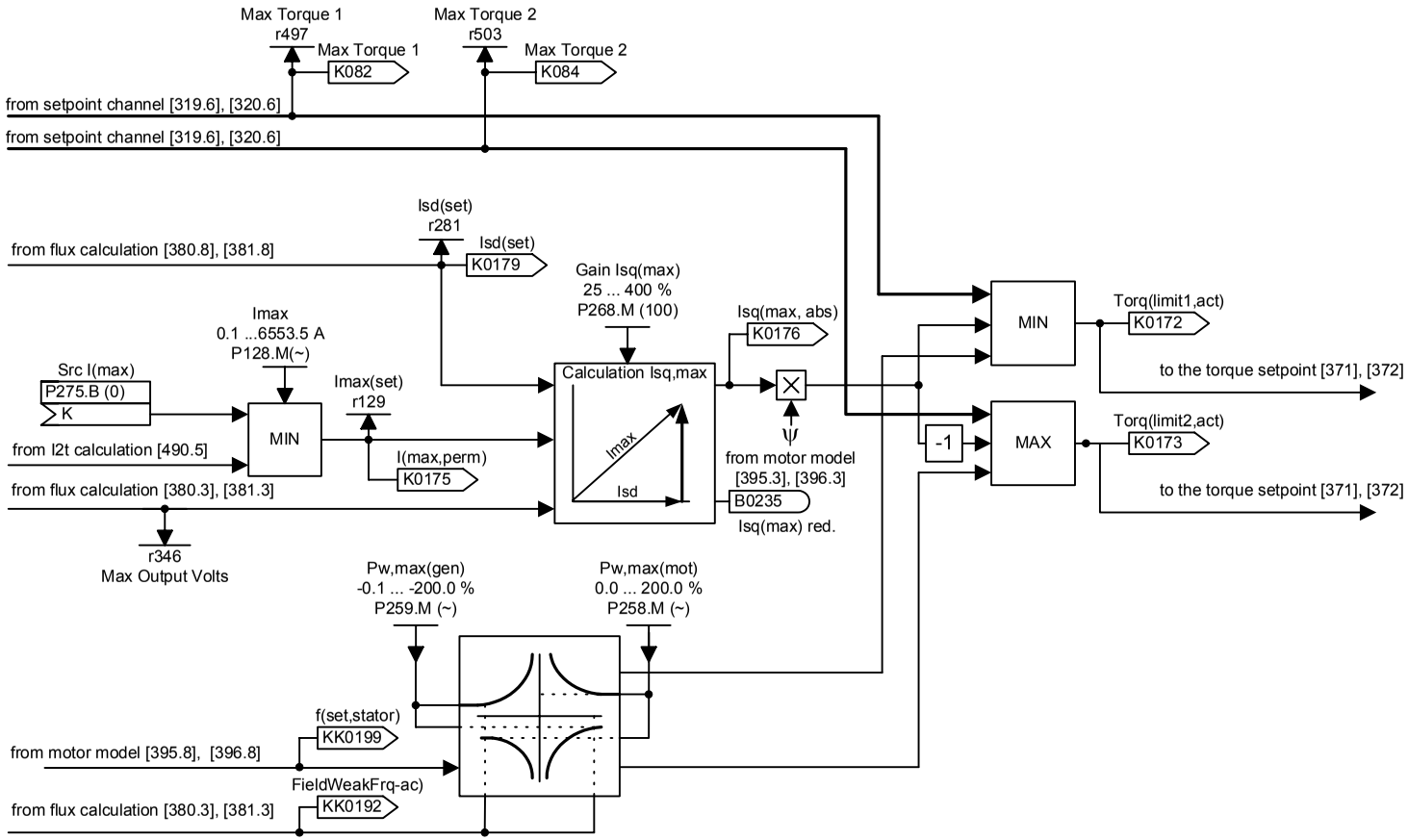

1	2	3	4	5	6	7	8
Torque/current limitation					fp_vc_370_e.vsd	Function diagram	- 370 -
n/f/T control, master/slave drive					31.01.98	MASTERDRIVES VC	

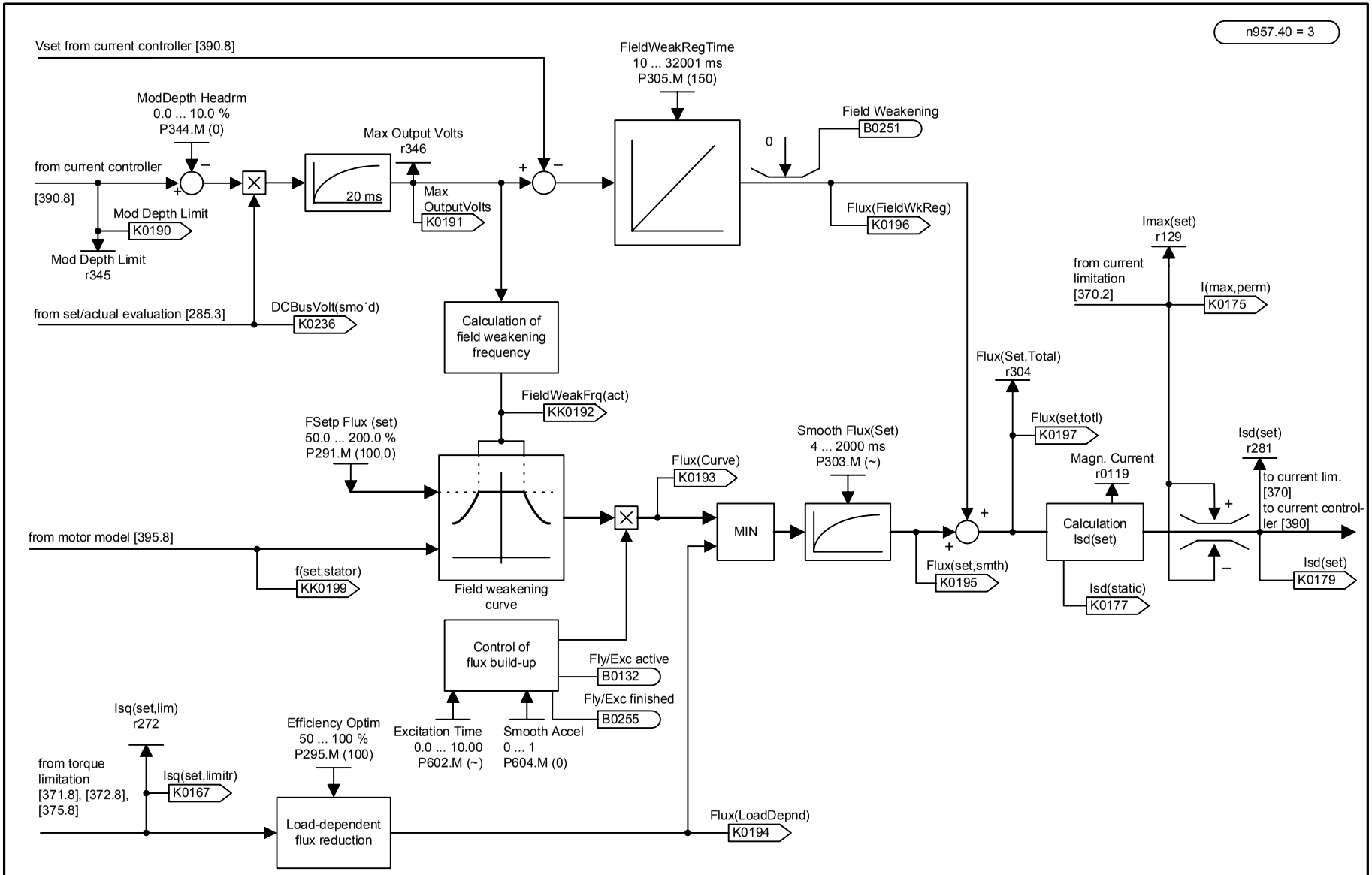

1	2	3	4	5	6	7	8
Flux calculation					fp_vc_380_e.vsd	Function diagram	- 380 -
n/T-control, master/slave drive					09.04.98	MASTERDRIVES VC	

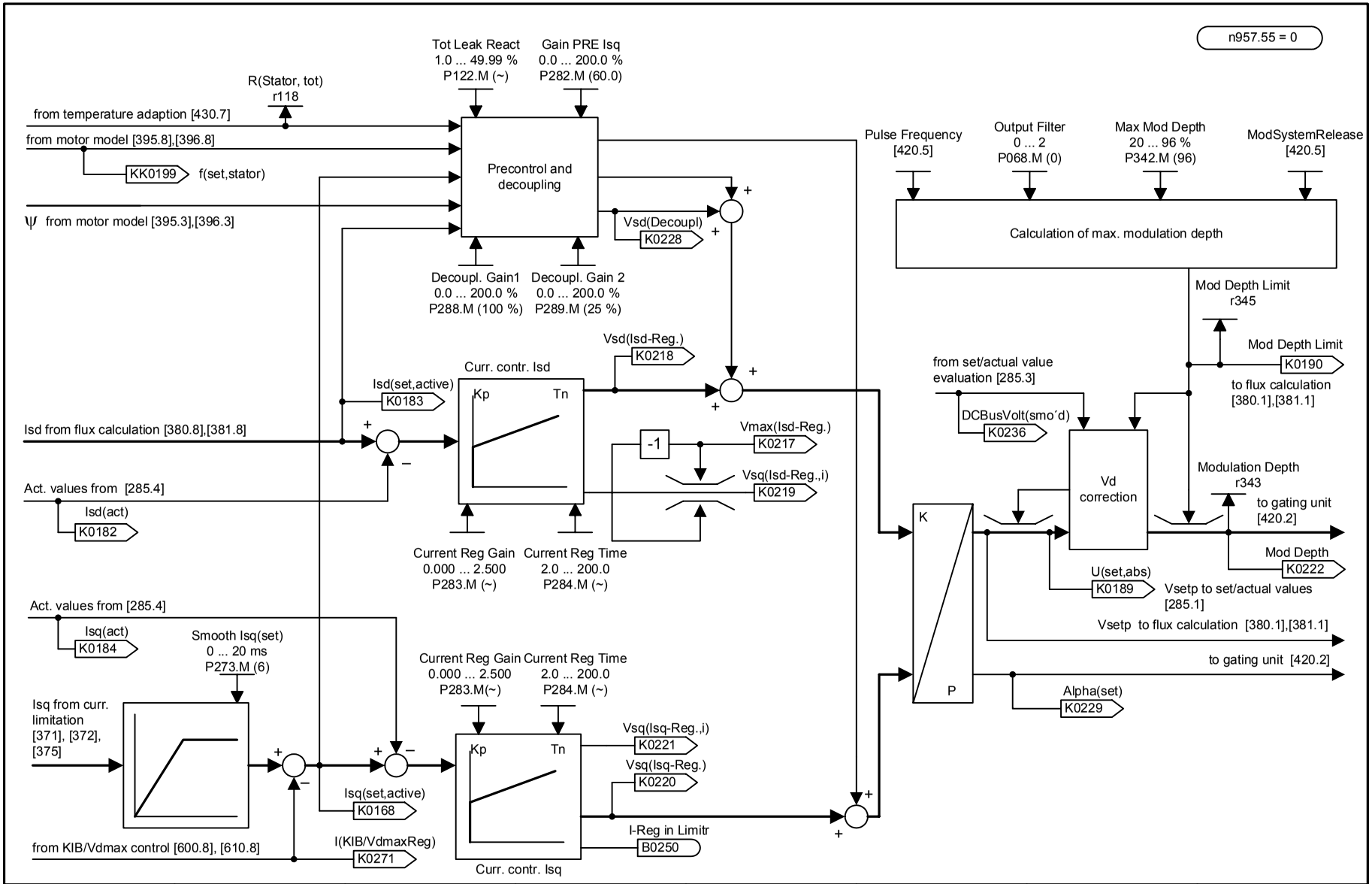

1	2	3	4	5	6	7	8
Current controller					fp_vc_390_e.vsd	Function diagram	- 390 -
n/f/T-control for master/slave drive					31.01.98	MASTERDRIVES VC	

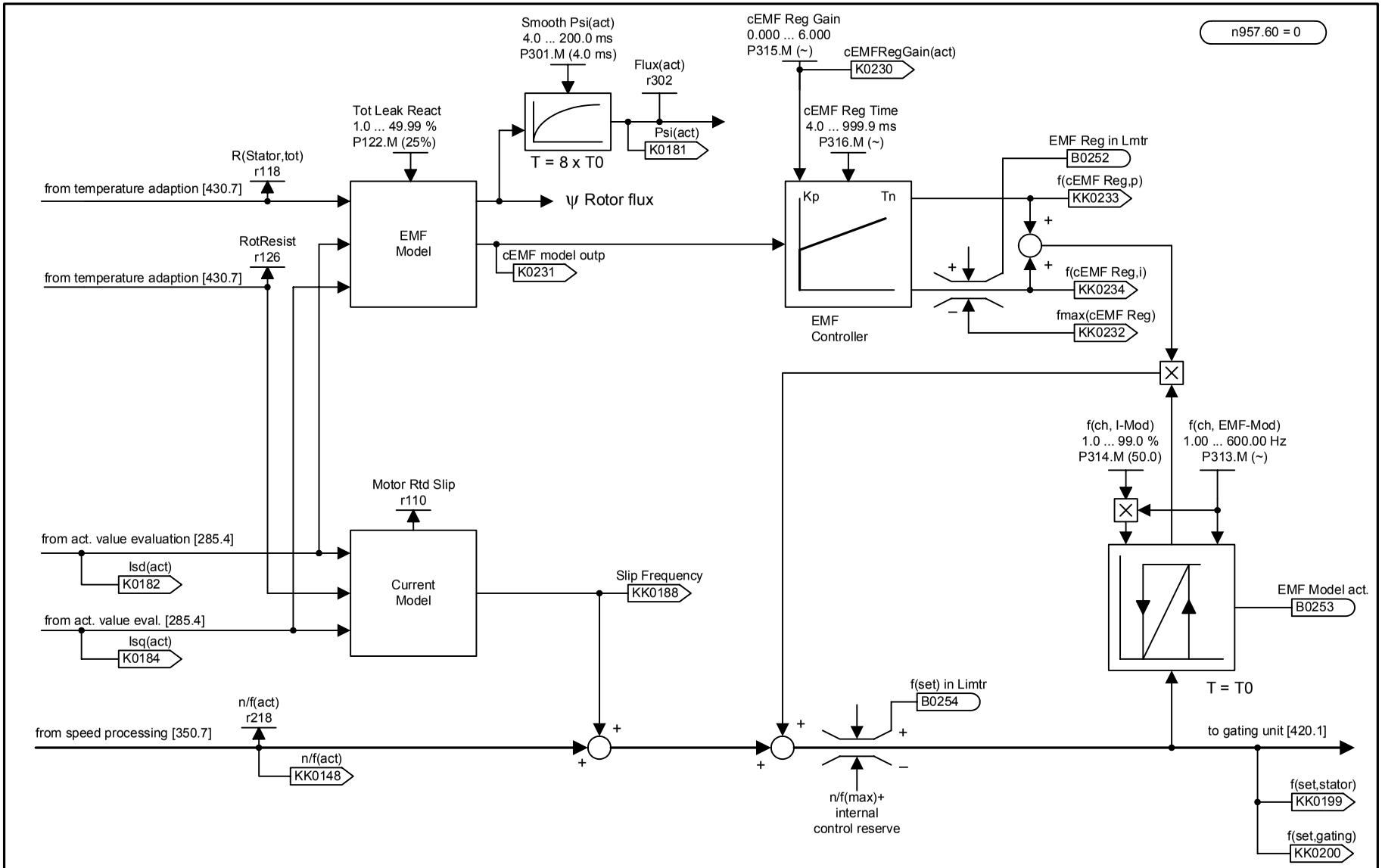

1	2	3	4	5	6	7	8
Motor model, frequency					fp_vc_395_e.vsd	Function diagram	- 395 -
Speed/torque control, master/slave drive					31.01.98	MASTERDRIVES VC	

Appendix D

Table D-1 Blocked-rotor test of Motor A

Motor A	Reading 1	Reading 2	Reading 3	Average
P_{ab} (W)	139.07	132.73	135.85	135.88
P_{ac} (W)	54.05	51.50	52.76	52.77
V_{ab} (V)	80.25	78.66	79.59	79.50
V_{ac} (V)	81.20	79.33	80.56	80.36
I_{ab} (A)	1.7369	1.7038	1.7232	1.7213
I_{ac} (A)	1.7675	1.7290	1.7543	1.7503

Table D-2 Blocked-rotor test of Motor B

Motor B	Reading 1	Reading 2	Reading 3	Average
P_{ab} (W)	165.65	165.91	166.08	165.88
P_{ac} (W)	64.13	64.24	64.29	64.22
V_{ab} (V)	88.73	88.81	88.89	88.81
V_{ac} (V)	89.90	90.03	90.05	89.90
I_{ab} (A)	1.8870	1.8880	1.8882	1.8877
I_{ac} (A)	1.9107	1.9100	1.9169	1.9125

Table D3 No-load test of Motor A

Motor A	Reading 1	Reading 2	Reading 3	Average
P_{ab} (W)	306.2	306.3	306.3	306.3
P_{ac} (W)	571.3	571.2	571.4	571.3
V_{ab} (V)	424.5	424.4	424.4	424.4
V_{ac} (V)	425.5	425.5	425.4	425.5
I_{ab} (A)	2.086	2.086	2.086	2.086
I_{ac} (A)	2.174	2.174	2.174	2.174

Table D4 No-load test of Motor B

Motor B	Reading 1	Reading 2	Reading 3	Average
P_{ab} (W)	290.0	290.0	289.2	289.7
P_{ac} (W)	532.6	534.9	535.3	534.3
V_{ab} (V)	421.4	421.3	421.0	421.2
V_{ac} (V)	422.3	422.4	422.2	422.3
I_{ab} (A)	1.914	1.918	1.914	1.915
I_{ac} (A)	2.047	2.047	2.045	2.046